NMR Studies of RNA Conformational Dynamics Induced by Metal Cations and Paromomycin

by

Anette Casiano-Negroni

A dissertation submitted in partial fulfillment
of the requirements for the degree of
Doctor in Philosophy
(Chemistry)
in The University of Michigan
2010

Doctoral Committee:

Professor Hashim M. Al-Hashimi, Co-Chair
Professor Carol Fierke, Co-Chair
Professor Charles L. Brooks III
Professor Ayyalusamy Ramamoorthy

To my parents José A. Casiano and María M. Negroni with all my love

Acknowledgements

First of all, I would like to thank my advisor Professor Hashim M. Al-Hashimi for all his advice, encouragement and patience through out my years here in Michigan. I also would like to thank my committee members, Professor Carol Fierke, Professor Charles L. Brooks III and Professor Ayyalusamy Ramamoorthy for all their help, time and insightful scientific discussions. Thanks to the present and past members of the Al-Hashimi Lab for their friendship, scientific discussions, support and our coffee trips!! Especially, I would like to thank Evgenia Nikolova, Dr. Jeet Chugh, Dr. Alexandar Hansen, Dr. Xioyan Sun, Dr. Melissa Getz, Dr. Qi Zhang, and Dr. Max Bailor for all the insightful discussions and collaborations.

I would like to thank all family members for all their love, prayers and always being there for me. Special thanks to my parents, José A. Casiano and María M. Negroni, for their unconditional love, encouragement and puertorrican homemade food ☺. I am blessed to have you both in my life!!! Thanks to my siblings for always keeping me smiling. My fiancé, Mitaire Ojaruega, thanks for all your love, English lessons ☺, patience and friendship. Finally, I would like to thank all my friends here in Michigan and Puerto Rico for all their love, encouragement and friendships.

Table of Contents

List of Figures

Figures

List of Tables

Tables

List of Appendices

Appendix

List of Abbreviations

A – adenine

aatRNA – aminoacyl transfer RNA

C – cytosine

COSY – correlated spectroscopy

CPMG – Carr Purcell Meibon Gill experiment

CSA – chemical shift anisotropy

G – guanine

HIV-1 human immunodeficiency virus type-1

HSQC – heteronuclear single quantum coherence

INEPT insensitive nuclei enhanced by polarization transfer

mRNA – messenger RNA

NMR – nuclear magnetic resonance

NOE – nuclear overhauser effect spectroscopy

PDB – protein data bank

RDC – residual dipolar coupling

RNA – ribonucleic acid

TROSY – transfer relaxation optimized spectroscopy

U – uridine

Abstract

Many regulatory RNAs adaptively change their conformation on binding to cognate protein and ligand targets or therapeutic molecules but the mechanism by which these conformational changes occur still remains poorly understood. In this thesis we characterize the dynamic properties of two RNA drug targets; HIV-1 TAR RNA and ribosomal A-site rRNA using a battery of NMR experiments that provide information on motions occurring over picosecond to millisecond timescales. We have used residual dipolar couplings (RDCs) in concert with structure-based electrostatic calculations to characterize the dependence of local and inter-helical recognition motions in TAR containing a trinucleotide pyrimidine bulge on the concentration of Na^+ and Mg^{2+}. Results revealed that Na^+ or Mg^{2+} induce a similar dynamic transition of TAR from an electrostatic relaxed bent and flexible state to a globally rigid coaxial state, which has a stronger negative charge density and association with counterions. The dynamic transition carries the TAR structure through several of the ligand bound conformations, indicating that metals and electrostatic interactions likely play an important role in adaptive recognition.

We used domain-elongation spin relaxation and relaxation dispersion NMR experiments to characterize base flipping and other local motions in the A-site rRNA in the absence and presence of the aminoglycoside antibiotic paromomycin. Our results

strongly suggest that A-site can dynamically access conformations in which the two adenines are flipped out at microsecond timescales and that binding to paromomycin is not necessary to induce this transition. These results were then compared to those obtained on a corresponding construct bearing an antibiotic resistance A1408G mutation. This single mutation leads to dramatic changes in the dynamics observed over picosecond to millisecond timescales. We propose that a G-A base-pair reduces the propensity to have both adenine residues looped out, thereby explaining in part the much lower antibiotic affinity for this RNA construct. Taken together, our results provide fundamental new insights into how internal motions occurring on different timescales can drive the conformational changes that accompany molecular recognition.

Chapter 1

Introduction

1.1 Background

1.1.1 RNA conformational dynamics and potential as a drug target

Ribonucleic acids (RNA) are involved in a host of cellular functions including regulation of gene expression at the transcriptional and translational level, protein transport, and protein synthesis (*1, 2*). Many of these functions require changes in the RNA conformation that are either self-induced (*3*) during RNA synthesis or that arise in response to recognition of specific proteins, other RNAs, small metabolite molecules and/or divalent ions (*4, 5*). These adaptive changes in RNA conformation provide a basis for sensory activity and/or temporal regulation in various biochemical pathways. For instance, protein induced changes in RNA conformation allows subsequent protein binding events to take place and consequently induce the sequential assembly of ribonucleoprotein (RNP) complexes like the ribosome (*2*).

Because many RNAs act as cellular switches, understating their function requires the characterization of both structural of dynamical properties. A key question is how do RNA structures manage to undergo changes in a specific fashion and in response to specific cellular signals? To understand the mechanism of structural changes, it becomes

necessary to characterize the flexibility of the RNA and the thermally accessible internal motions. These include fast picoseconds librations of non-canonical residues that are not involved in stacking or hydrogen bonding interactions such as looped out bulges that feature base motions and sugar repuckering dynamics; diffusion limited collective helical motions occurring at nanosecond timescales that result in large changes in the RNA global structure; and slower transitions occurring at micro-to-millisecond timescales that involve disruption of hydrogen bonding and stacking interactions, and even slower motions occurring at millisecond to second timescales involving large changes in secondary structure.

The growing importance of RNA in gene expression and regulation has been accompanied by a growing list of RNA drug targets, many of which act as flexible switches (*1, 6-8*). Indeed, RNA is already an established drug target since many antibiotics that target the ribosome do so by binding specifically to ribosomal RNA (*9*). Importantly, large changes in structure and disruption of RNA switching activity, often accompanies drug binding. Understanding the mechanism by which small molecules interact with RNA and the effects on structure and dynamics is therefore fundamentally important for biomedical applications and for targeting RNA in drug discovery efforts.

In this thesis we will study the structure and dynamics characteristics of two major RNA drug targets; HIV-1 TAR is a viral drug target while the ribosomal A-site rRNA is a bacterial drug target.

1.1.2 HIV-1 TAR: A paradigm for studying RNA conformational dynamics

The human immunodeficiency virus (HIV) is the causative lentivirus of the acquired immune deficiency syndrome (AIDS), and it is the deadliest pandemic up to date. According to a report published by the World Health Organization (WHO) and the Joint United Nations Programme on HIV/AIDS (UNAIDS), since the beginning of this epidemic in 1981, approximately 60 million people have been infected with HIV and 25 million people have died of HIV related causes (*10*). In 2008 there were around 2.7 million new cases of HIV with 430,000 being children under the age of 15 (*11*). HIV type 1 (HIV-1) is one of the main strains of HIV infection in humans and it constitutes the main causative agent of global HIV infections (*12*). Although there is progress on anti-retroviral treatments for AIDS/HIV, there is currently no vaccine or cure for this disease. The current available drug cocktails are very expensive and are continually being affected by the growth of drug-resistant mutations in the virus (*13*). As a result, the necessity to investigate and develop novel anti-HIV therapeutics has arise bringing much attention to the highly conserved structured RNA elements in the 5' non-coding region of the HIV-1 genome (*6, 8, 13*). These RNA elements play essential roles in different steps of the HIV replication cycle making them potent anti-HIV drug targets that can significantly suppress viral functions (*6, 8*).

One of these RNA elements is the trans-activation response element (TAR). TAR is a stem-bulge-loop RNA located at the 5'-end of the non-coding region of all HIV-1 mRNAs (*14, 15*). It plays an essential role at different steps of the viral replication cycle, including transcription and translation (*6, 14, 16*). During transcription, after TAR is transcribed, the RNA polymerase II (RNAP II) pauses ~60 nucleotides downstream from

the promoter. Subsequently, TAR binds the viral protein Tat and the Positive Transcription Elongation Factor b complex (P-TEFb). The P-TEFb is composed of the proteins Cyclin T1 and the Cyclin-Dependent Kinase 9 (CDK9) (*14*). Tat is believed to bind TAR in the UCU trinucleotide bulge, while Cyclin T1 is believed to bind the apical loop of TAR (*17*). Following the formation of the TAR-Tat-P-TEFb complex, the Cyclin T-associate CDK9 kinase phosphorylates the carboxyl terminal domain of the RNAP II inducing efficient promoter clearance succeeded by viral transcription elongation (*14, 17*). On the translational level, TAR participates on HIV-1 RNA translation regulation through binding of proteins PKR, TRBP and La (*14, 18*).

These essential functions of TAR in the HIV-1 cycle and proliferation of this virus makes this RNA a candidate target for anti-HIV drugs (*19, 20*). For example, a compound that could bind TAR RNA preventing Tat binding will disrupt Tat-mediated transcription elongation of HIV-1 genes ultimately inhibiting viral replication (*19-22*). The quest to develop these inhibitors is to understand the molecular basis of HIV-1 TAR and Tat interactions. Different biochemical studies such as chemical probing, mutagenesis and peptide ligand binding showed that nucleotides 19-43 comprise the minimal region of TAR necessary for Tat-P-TEFb binding and that the Tat binding site surrounds the UCU bulge area by interacting with an arginine rich region in the protein (*23-27*). Structures using this minimal binding region have been reported for HIV-1 TAR free (*28*) and bound to Tat peptide mimics (*29, 30*). These structures show that binding of Tat derived peptides results in a TAR conformational helix rearrangement from a bent (~45º) to a coaxial alignment as shown in Figure 2.1 (*28*) (*29, 31*). Moreover, structures have been solved for TAR bound to Ca^{2+} ions (*32*) and five distinct small molecules

designed to inhibit its interaction with Tat (*20, 33-35*). These structures reveal that TAR is able to bind chemically diverse targets by adopting significantly different global helical orientation (inter-helical angles spanning the range from ~5º up to ~45º) and local conformations around the binding pocket comprise of the bulge and neighboring residues (Figure 2.1).

Electrostatic interactions can be one contributing factor driving these conformational changes accompanying HIV-1 TAR-ligand complex formation. For instance, the spatial arrangements of basic groups in Tat relative to the negative TAR surface is an important determinant of Tat binding and its induced TAR conformational changes (*26*). The conformation of Tat bound TAR can be stabilized by distinct small molecules that can satisfy two key electrostatic interactions (*29, 30, 35*). Moreover, aminoglycosides bind TAR with affinities that correlate with their total number of positive amines (*36*). In this thesis we used a combination of solution nuclear magnetic resonance (NMR) and structure-based electrostatic calculations to characterize the role of electrostatic interactions in HIV-1 TAR RNA conformational adaptation upon ligand binding.

1.1.3 Ribosomal A-site RNA: An important site for translation fidelity and antibiotic therapy

The bacterial ribosome is a 2.5 MDalton ribonucleoprotein complex that translates the mRNA information into protein by polymerizing amino acids in the order specified by the mRNA sequence. It is composed of two subunits (50S and 30S) containing over 50 proteins and 3 large RNAs (*37*). The large 50S subunit harbors the

peptidyl transferase activity that is responsible for making the protein peptide bonds during elongation and hydrolyzing the peptidyl-tRNA during the termination step of protein synthesis (*38*). The small 30S subunit contains the decoding site where the selection of the correct aminoacyl-tRNA (aa-tRNA) takes place (*38*). There are three tRNA binding sites in the ribosome: the A, P and E sites. The ternary complex containing aa-tRNA, GTP and Elongation Factor Tu (EF-Tu) is delivered to the A-site at the initiation of the elongation cycle of protein synthesis (Figure 1.1). This is a reversible initial binding step that dissociates rapidly when the mRNA codon and tRNA anticodon is not correct (non-cognate). When the codon is recognized, the complex is stabilized and EF-Tu undergoes a conformational change towards the active site of GTP hydrolysis. Following GTP hydrolysis, the EF-Tu loses affinity for the aa-tRNA, releasing it from the complex. Subsequently, the tRNA accommodates in the A-site of the peptidyl transferase center and reacts with the peptidyl-tRNA located in the P-site. This generates a peptidyl-tRNA and deacylated tRNA bound A-site and P-site respectively. Consequently, translocation occurs yielding the movement of peptidyl-tRNA and deacylated tRNA to the P-site and E-site respectively (*38*). The deacylated tRNA located in the E-site leaves the ribosome and a new mRNA codon is exposed in the A-site starting the elongation cycle one more time.

Accurate selection of the cognate aa-tRNA during protein synthesis depends on the correct pairing of the mRNA codon with its aa-tRNA anticodon. This essential step takes place at the A-site decoding region. A-site is a ribosomal RNA located within helix 44 of the 16S rRNA of the 30S ribosomal subunit. It contains an adenine internal loop that inspects the codon-anticodon mini-helix formed during the aa-tRNA initial selection

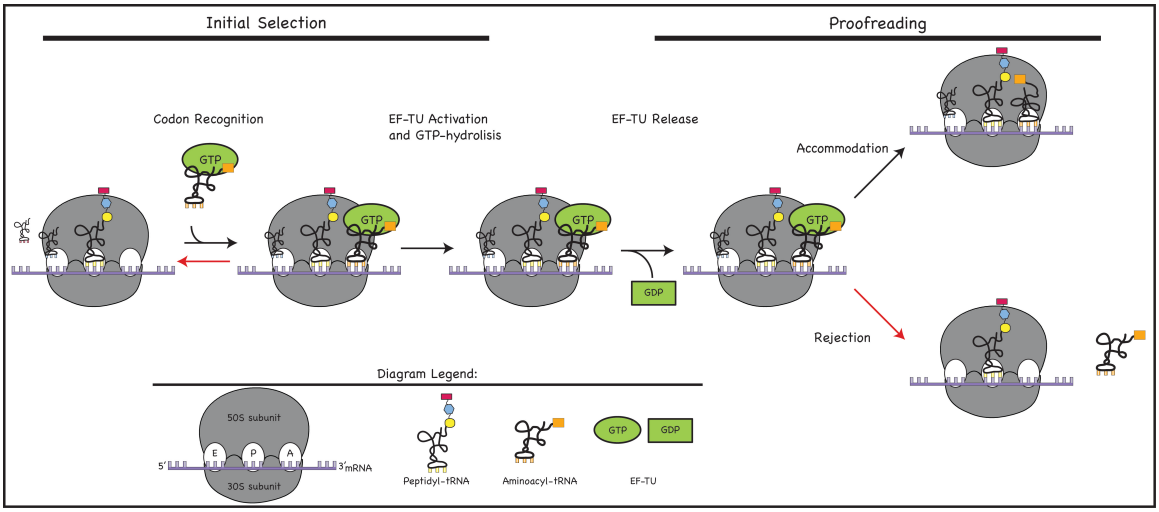

Figure 1.1: The aa-tRNA selection during protein synthesis

pathway (*39, 40*). Proper formation of the codon-anticodon mini-helix results in a conformational change in the A-site rRNA, which is known as the "on" state. This state involves the looping out of the A1492 and A1493 bases that interact with and stabilize the first two base pairs in the mini-helix (*40, 41*). For instance, A1493 monitors the geometry of the mini-helix first base pair by forming hydrogen bonds with the 2' hydroxyl groups of both the anticodon and codon bases (*40, 42*). Adenine 1492 together with G530 (from helix 18), spans the minor groove of the second base pair. The orientation of this base pair if further stabilized by hydrogen bonds to C518 (helix 18) and serine 50 (protein 12) (*39, 40*). These interactions are non-sequence specific but specific for Watson-Crick base pairs (*40*). Lastly, the third position of the mini-helix is monitored less stringently and thus is more prone to errors (*40, 42*). The "off" state of A-site is when there is no aminoacyl-tRNA anticodon to interact with the mRNA codon. During this state the two adenines (A1493, A1492) located in the internal loop are bulged in or one of them is dynamically flipping in and out from the helix.

In prokaryotes, the ribosome has been the target of many important antibacterial drugs. These antibiotics interfere with different essential steps in protein synthesis (*43*). The macrolides, lincosamides and streptogramin B antibiotics interact with the peptidyl transferase center in the 50S subunit (*44*). Aminoglycoside antibiotics can induce codon misreading and inhibit translocation. These antibiotics can be divided in two main classes: the ones containing streptamine and 2-deoxystreptamines aminoglycosides. The later class of aminoglycosides can be further divided into two different subclasses: 4,5- and 4,6-disubstitude antibiotics (*45*). Aminoglycosides have different binding sites on the small subunit; specially most of these antibiotics have been shown to interact directly with the ribosomal RNA (rRNA). Structural and chemical protection studies have shown that aminoglycosides specifically bind A-site rRNA (*6, 44, 46*). Upon binding, aminoglycosides induce destacking of the A1493 and A1492 bases of the internal loop, stabilizing the mini-helix continuously even if an incorrect anticodon-codon is paired (*39*). This way, aminoglycosides can disrupt the fidelity of the anticodon-codon pairing, decrease the rate of protein production and consequently cause cell death.

Nevertheless, clinical and biochemical studies have shown the increasing occurrence of antibiotic resistance due to mutations at different positions of the decoding site (*44, 47, 48*). The introduction of the A1408 to G mutation in particular confers the most significant resistance for aminoglycosides (*48-50*). Remarkably this substitution could be the basis of the antibiotic discrimination between the prokaryotic and eukaryotic A-site rRNAs. However, this mutation only caused an intermediate level of resistance for paromomycin and geneticin aminoglycosides in *E.coli* 16S rRNA (*49, 51*). Recent studies suggest that the specificity of aminoglycoside action lies not in their different binding

affinity to the prokaryotic and eukaryotic A-site rRNAs but rather in their distinct abilities to induce base destacking in the two RNAs (*52*). Despite the current knowledge of aminoglycoside binding to prokaryotic A-site rRNAs, the molecular basis for the mechanism of action remains poorly understood and it has been of great interest especially since bacteria is creating resistance against antibiotics.

In this thesis we quantitatively characterize the conformational dynamics of the unbound and drug bound forms of the prokaryotic A-site rRNA from *E.coli* and compare the findings with results obtained on a corresponding construct bearing the A1408 to G1408 mutation. These results will give us more insight on the basis of decoding and aminoglycoside resistance.

1.2 **Characterizing nucleic acids using NMR**

1.2.1 Brief historical survey of NMR and its application to the study of nucleic acids

NMR spectroscopy is a powerful technique for characterizing biopolymers such as proteins and nucleic acids at atomic resolution. Besides being one of two techniques that can be used to determine three dimensional structures of macromolecules (*53*); NMR has the capabilities of characterizing biomolecular dynamics such as folding, enzyme catalysis, ligand binding, reaction kinetics and intra/intermolecular dynamics among others (*54-59*).

This phenomenon started in 1937 when Rabi and coworkers made the first NMR observation using molecular beams. Almost a decade later, the groups led by Purcell (*60*) and Bloch (*61*) carried out the first NMR experiments of bulk materials, paraffin wax and water. In the years that followed, instrumental development and different basic theories

underlying NMR parameters were established. A major step forward in NMR occurred in 1966 when Ernst and Anderson developed the Fourier Transform (FT) spectroscopy (*62*). This new technique offered shorter time to record a spectrum and improved sensitivity of the experiments by several fold. The next break-through discovery that led to the advancement of new frontiers in nuclear magnetic resonance was the introduction of two dimensional (2D) NMR by Jeener in 1971 (*63*) and a third frequency dimension (3D) in late 1980s (*64, 65*). Subsequently, a vast variety of experimental schemes have been designed expanding the applicability of NMR in the characterization of complex macromolecules and biopolymers.

The study of nucleic acid structure and dynamics using NMR started in 1964 with the first polynucleotide proton spectra acquired by the groups led by Penman (*66*) and Gibbs (*67*). The first applications of FT NMR on RNA were applied to tRNA samples (*68-70*). These early studies highlighted the difficulty of the RNA proton spectrum. The structural homogeneity of the RNA A-form helix composed only of four very similar nucleotides lead to a limited chemical shift dispersion and congested resonance spectra, especially in the ribose sugars. Chemical shift dispersion is only usually observed for non-canonical structural regions like bulges, loops and hairpins. Nevertheless, the advent of multidimensional FT NMR and the introduction of isotopically $^{13}C/^{15}N$ label RNA samples have paved the way for a broad distribution of applications of biomolecular NMR to study nucleic acids. To date, there has been a growth on the number of three-dimensional structures of nucleic acids solved by NMR spectroscopy. In addition, experiments to quantitatively characterize biologically important local and global dynamics of RNA in solution within a variety of timescales have been developed (*2, 71,*

72). For instance, traditional ^{13}C and ^{15}N spin relaxation measurements can be used to detect diffusive picosecond to nanosecond motions (*54*), relaxation dispersion experiments can be use to measure microsecond to millisecond dynamics and characterize the "invisible" excited states (*73-75*). Residual dipolar couplings can be used to detect motions occurring at sub-millisecond timescales (*76-78*). Moreover, lineshape analysis and ZZ-exchange can be used to probe slower motions at the second timescale and provide kinetic information upon ligand binding (*55, 79, 80*). Finally, chemical shift mapping can be used to monitor metal, small molecules, other RNA and protein binding to nucleic acids.

1.2.2 RNA resonance assignments

Identification of the RNA chemical shifts in the spectrum is a fundamental yet challenging requirement before any further NMR studies. The standard strategy for the resonance assignment of nucleic acids consists of sequential intra- and internucleotide base to ribose sugar connectivity using basic NOESY experiments (*53*). In an unlabeled RNA, a basic NOESY experiment can correlate all the protons within 5Å distance via through-space dipolar-dipolar interactions. Here, the aromatic protons H8 in purines (or H6 in pyrimidines) will show NOE cross-peaks to their own H1' and the H1' of the preceding nucleotide in the 5' direction. This gives rise to the "NOE-walk" which will ultimately connect the H2, H6, H8, and H1' from the 3' to 5' direction in the RNA A-form helix. The resonance assignment of exchangeable imino (H1/H3) and amino protons of bases within the helical regions of the RNA can also be established through intra-base or sequential NOEs (*81*). For isotopically labeled RNA samples, using 2D or 3D (^{13}C or ^{15}N

filtered) NOESY-HSQC and (^{13}C or ^{15}N filtered) HSQC-NOESY experiments can be beneficial to resolve unclear exchangeable or non-exchangeable NOEs assignments (*81, 82*) (Figure 1.2A,C).

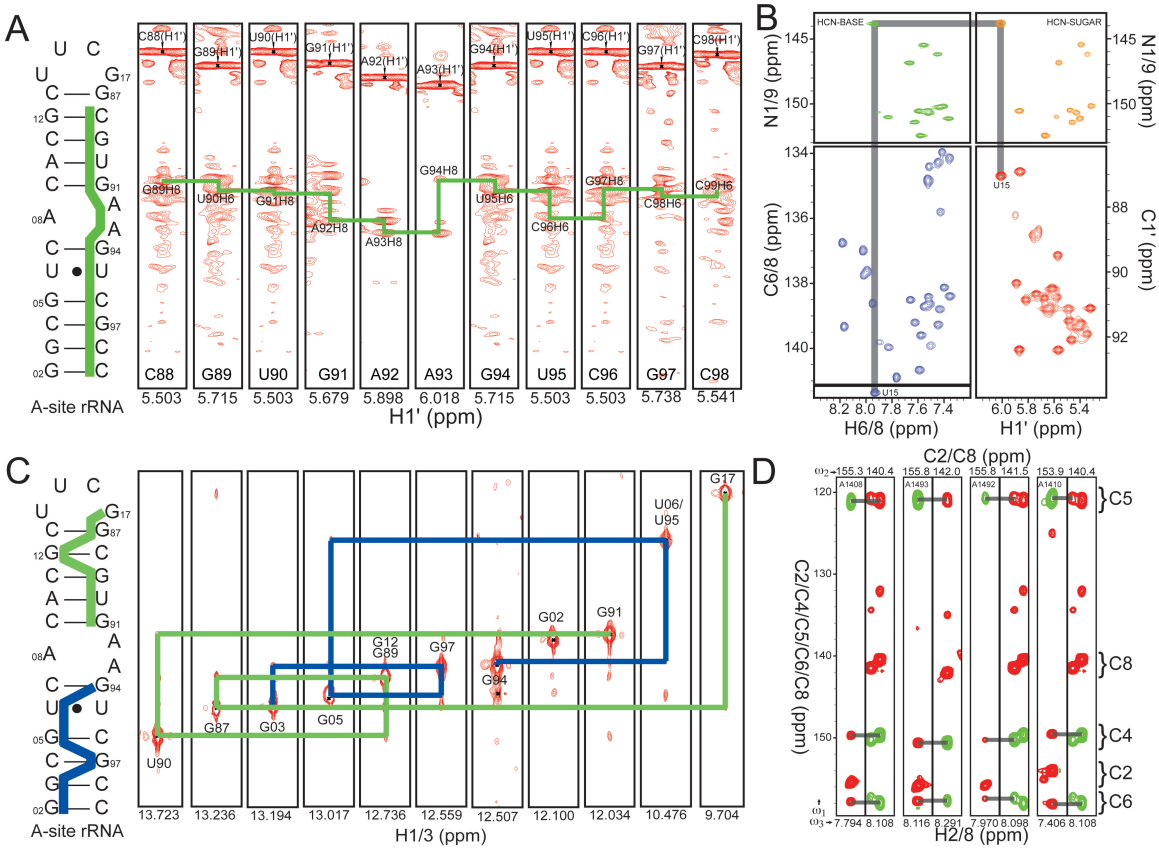

Figure 1.2: Resonance assignments of A-site rRNA. A) On the left panel is the secondary structure of A-site and highlighted in green is the sequential NOESY assignment. The right panel shows the ^{13}C NOESY-HSQC spectra. B) HCN spectra together with the correspondent C6/C8 and C1' HSQC spectra. C) On the left if the secondary structure of A-site. The right panel shows the 15N NOESY-HSQC strips with the sequential assignments highlighted in blue (helix I) and green (helix II). D) 2D strips of the ^{13}C HCCH-COSY

Unstructured regions of the RNA such as loops and bulges are usually more difficult to assign using the conventional NOESY experiments since vague NOEs can occur from non-sequential spatial proximity. In this case, the combination of multidimensional NMR assignment experiments and uniformly ^{13}C/^{15}N labeled RNA can greatly facilitate the chemical shift assignments especially of these unstructured regions. These assignment experiments are mostly based on through-bond and direct coupling

connectivity, thus overcoming ambiguities from vague NOEs. In addition, many of these experiments can be implemented in a 2D or 3D fashion, depending on the difficulty and resonance overlap of the RNA spectra.

Intranucleotide assignments between a nucleobase and its corresponding ribose sugar can be achieved through the HCN triple resonance experiment in isotopically labeled samples (*82, 83*). This experiment directly correlates the C6-H6/C8-H8 in the base to C1'-H1' resonances in the sugar ring through the shared N1/9 atoms of the same residue (*83*) (Figure 1.2B). The HCN detects these correlations by stepwise coherence transfer from ^{1}H to ^{13}C to ^{15}N and back through direct $^{1}J_{CN}$, $^{1}J_{CH}$ coupling (*83*). The different chemical shift ranges for $^{15}N9$ C (150-156 ppm), $^{15}N9$ U (142-146 ppm) and $^{15}N1$ A/G (166-172 ppm) are also very useful to clearly distinguish the nucleobases to ribose sugar connections by residue type (*81*). In adenines, the connection between C2-H2 to C8-H8 can be attained through the HCCH-COSY experiment (*82, 84*) (Figure 1.2D). Moreover, the correlation between exchangeable imino protons (H1/H3) by intranucleotide through-bond connectivity to its corresponding C8 (guanine) and C6 (uridine) can be established with the HCCH-TOCSY experiment (*82, 85, 86*). An experiment that can be used to elucidate the base-pairing and more complex hydrogen bonding pattern within the RNA is the HNN-COSY experiment. Here hydrogen bond donor imino protons (H1/H3) and its nitrogen acceptor (N1/N3) can be correlated through sizable $^{1}J_{NN}$ couplings (*87-89*).

1.2.3 NMR methods to characterize RNA-ligand interactions

Nuclear magnetic resonance has emerged as a powerful technique for the characterization of RNA-ligand interactions with protein, metal ions, small molecules and other RNA molecules at the molecular level. Many NMR applications have been developed to monitor and characterize such molecular interactions like chemical shift mapping, intermolecular NOEs, line-shape analysis, dynamics and exchange perturbation, paramagnetic methods, and dipolar interactions among others (*55, 59, 90*). Using these experiments one can obtain information from site-specific binding up to ligand binding kinetic rates. Of particular interest in our study is the ability to monitor RNA interactions with metals ions and small molecules.

NMR spectroscopic applications to study RNA-metal interactions are based on chemical shift mapping, paramagnetic resonance enhancement and intermolecular NOEs contacts (*82*). The chemical shift mapping upon small additions of metal ion is the most common used method. Chemical shifts are very sensitive to the chemical environment surrounding a particular spin and thus can be affected by diffusive or specific localization of metal ions or induced structural conformations. Here, apparent metal ion binding affinities can be obtain by plotting changes in the chemical shifts of traditionally measured ^{1}H, ^{13}C, ^{15}N and ^{31}P resonances of the RNA as a function of metal ions while assuming a two-state binding model (*78, 91, 92*). The chemical shift perturbations at high sodium (Na^{+}), magnesium (Mg^{2+}) and lead (Pb^{2+}) ion concentrations have been used to identify site-specific metal binding in the lead-dependent ribozyme (*93*). Also, RNA chemical shift analysis in the presence of a combination of different metal ions such as

zinc (Zn^{2+}), Mg^{2+} and cobalt hexamine ($Co(NH_3)_6^{2+}$) have been used to differentiate between diffusive and specific bindings to RNA (*94, 95*). One other technique used to study direct RNA-metal interactions is paramagnetic resonance enhancement (PRE). Here, the presence of a paramagnetic ion, like Mn^{2+}, enhances the relaxation of spins that are in close proximity. This leads to line broadening and ultimately disappearance of the NMR signal. The strength of this effect is dependent on the degree of occupancy of the metal binding site and proportional to $\frac{1}{r^6}$ where r is the distance between the paramagnetic ion and the spin of interest. Therefore, PRE can provide useful distance information that in the end can be used in RNA-metal structure calculations (*82, 95*). The use of intermolecular NOEs contacts is another technique that can provide a direct way to measure the distance between the metal ion and the RNA. The ammonium groups of metal ions complexes such as $Co(NH_3)_6^{2+}$ and ammonium (NH_4^+) can show NOE cross peaks with the nearby protons of the RNA that can be detected with a basic 2D NOESY experiment (*96*). The intensity of the cross peaks can be divided into different groups depending on the distances. Ultimately, this information can be used in RNA-metal complex structure determination. This approach was used in the structure determination of cobalt hexamine bound to the P5 helix of the group 1 intron ribozyme (*97, 98*), GAAA stable tetraloop (*99*) and P4 element of the RNase P ribozyme (*100*).

A variety of NMR experiments can be used to obtain insights into RNA-small molecules interactions in solution at atomic resolution. The most common way of monitoring binding of a small molecule is by following chemical shift perturbations of the isotopically labeled RNA with incremental additions of the unlabeled ligand. This method allows the detection of the RNA-ligand interface, estimation of the affinity,

specificity and kinetics of binding. Moreover, the kinetics of the reaction determine chemical shift perturbations during the ligand titration (*59, 101*). For example, if the dissociation process is fast there will always be a single set of resonances at the binding interface that will move continuously through out the titration. This single set of resonances is a fractionally weighted average of the unbound and bound species. This scenario is known as the fast exchange regime (*59, 101*). If on the opposite end, the dissociation process is slow then one will observe a set of resonances for the unbound species and another for the bound species. During the titration, the free species will slowly disappear while the bound one will appear. This scenario is known as the slow exchange regime (*59, 101*). Line shape analysis, ZZ-exchange and chemical exchange experiments can be used to elucidate the kinetic parameters and binding affinities governing the ligand binding reaction (*55, 58, 80*).

1.3 **Methods to characterize RNA conformational dynamics by NMR**

1.3.1 Residual Dipolar Couplings

The measurement of NMR residual dipolar couplings (RDCs) in partially aligned systems have opened the window of structural dynamics information that now can be obtained for biomolecules, including nucleic acids. RDCs are sensitive to motions occurring over a wide range of biologically important events and thus can provide new insights of the structural plasticity of RNA.

Dipole-dipole interactions between nuclear spins occur as a result of the modulation of the local field of a nucleus by the nuclear magnetic fluctuation from the neighboring

nucleus. The direct dipole-dipole interaction (D_{ij}) between a pair of ½ spin nuclei (i and j) can be calculated using the following expression (*102-104*):

$$D_{ij} = -\frac{\mu_0 \gamma_i \gamma_j h}{8\pi^3 \left\langle r_{ij}^3 \right\rangle} \left\langle \frac{(3\cos^2 \theta_{ij} - 1}{2} \right\rangle \tag{1.1}$$

where γ_i and γ_j are the gyromagnetic ratios of spins i and j, *h* is Planck's constant, μ_0 is the magnetic permittivity of vacuum, r_{ij} is the internuclear distance between the spins (i and j) and θ_{ij} is the angle between the internuclear vector i-j and the magnetic field axis. The angular term ($3\cos^2\theta_{ij}$-1) is the second rank Legendre function, $P_2(\cos\theta_{ij})$ modulated by the angle θ_{ij}. The angular bracket ($\langle\ \rangle$) in Equation 1.1 denotes that the angular term is time-averaged over the molecular motions sampled by the internuclear vector that are faster than the inverse of the dipolar interaction. The molecular motions sample by the vector consists of overall molecular reorientation and internal motions. Motional averaging will generally reduce the value of the angular term and thus the magnitude of observed dipolar couplings.

In solution conditions, isotropic motions allow a given bond-vector to sample directions uniformly averaging the angular term to zero (Figure 1.3A). This explains why dipolar couplings are not usually observed in solution. However, if the solute of interest experiences a degree of alignment then the angular term will no longer average to zero (Figure 1.3A) (*102*). Even a small net orientation of 10^{-3} is sufficient to observe dipolar couplings in solution. In addition, the greater the degree of alignment in the solution, the larger the value of the angular term and magnitude dipolar couplings. As in the case for scalar couplings (*J*), dipolar couplings (*D*) successfully increase and decrease the average

experienced magnetic field of a given nucleus. This fluctuation on the average magnetic field produces the splitting of resonances.

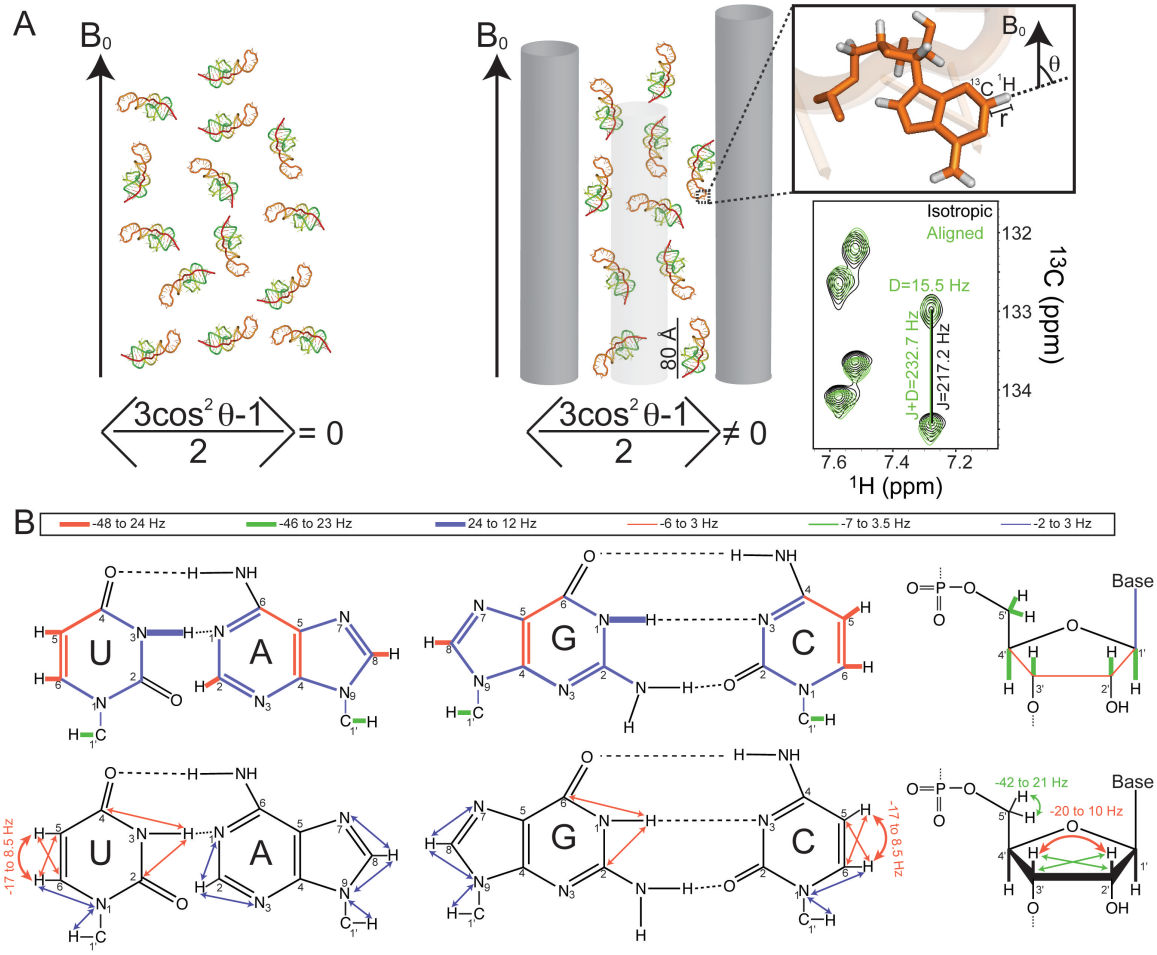

Figure 1.3: Residual Dipolar coupling measurements in RNA. A) No RNA alignment in solution (left panel) and partial RNA alignment using Pf1 phage used to calcualte RDCs (right panel). A representative spectra of RDC measuremtns is shown on the bottom right panel. B) RDCs measured in base and sugar of RNA.

There are different liquid crystalline solvent systems that are used for inducing molecular alignment in biomolecules (*102, 104*). Disc-shaped bicelles (*102, 105, 106*), polyacrylamide gels (*107, 108*), and rod-shape viruses like Pf1 phage and TMV (*109-111*) are some examples of liquid crystalline solvent systems. The type of alignment

media is chosen depending on the pH, temperature or ionic strength conditions of the system of interest (*104*). For the case of nucleic acids, the most common alignment media used is the filamentous bacteriophage Pf1 (*109, 111*). The molecules of Pf1 phage have a rod-like shape, its medium have a low nematic threshold concentration and its negative nature reduces the possibility of interacting with nucleic acids (*110, 112*). Consequently, Pf1 induces alignment in the RNA through steric and electrostatic mechanisms (*112, 113*). The optimum level of alignment is in the order of 10^{-3}, which means that at least 1 from 1,000 RNA molecules is completely aligned. This optimum level of alignment can be obtained for small RNAs (< 30 nt) with concentrations of phage of 18 to 25 mg/ml. The concentration of phage can be calculated from its UV absorbance at 270nm and extinction coefficient of 2.25cm ml/mg (*110*). Another way is to divide the observed deuterium residual quadrupular splitting by a factor of 0.886 (*110*).

Dipolar couplings are often measured as new contributions to scalar couplings (*J*) that are observed under conditions of molecular alignment (*J+D*). In the case of nucleic acids, experimental RDCs are computed from the difference in the splitting of RNA resonances measured in the presence and absence of Pf1 phage (Figure 1.3A, bottom right panel). The most common measured RDCs in nucleic acids are the one bond C-H and N-H in both the ribose sugar and base moieties due to their favorable size (Figure 1.3B). These one-bond RDCs include the vectors C1'H1', C2H2, C5H5, C6H6, C8H8, N1H1, and N3H3 because they are the easiest to assign using basic NOESY and through-bond correlation experiments (*81, 114*). Additional one, two and three bond RDCs can also be measured as shown on Figure 1.3B, but these are smaller and might be difficult to measure in large RNAs (>60 nt). Once the RDCs are measured, one can obtain structural

information through a simulated annealing approach or order tensor analysis. The simulated annealing approach incorporates RDC measurements into a penalty function along with NOEs and other restrains during the calculation of the lowest minimum energy structure for a particular biomolecule (*115, 116*). The order tensor analysis determines the relative orientation of fragments ultimately providing structural and dynamical information for a particular RNA target (*117*).

The RDC analysis in terms of structural and dynamical information for a particular target requires the specification of an order tensor that describes the overall alignment of the molecule relative to the applied magnetic field (*118*). This information is obtained by the interpretation of the angular term in Equation 1.1. This term can be expressed in terms of time independent orientation of an internuclear vector in the molecular frame (α) and five order tensor elements (S_{kl}) (*119*),

$$\left\langle \frac{3\cos^2\theta_{ij} - 1}{2} \right\rangle = \sum_{kl=xyz} S_{kl} \cos(\alpha_k^{ij}) \cos(\alpha_l^{ij}) \ , \tag{1.2}$$

where the α_n is the angle between the internuclear vector and the n^{th} axis of the arbitrary frame. The overall motion and orientation of the alignment frame are absorbed into the elements of S_{kl} which forms a traceless 3 x 3 Cartesian matrix describing the order tensor (*102, 119*). Here, only five parameters are independent (*119*). Two of the principal order parameters define the asymmetry (η, Equation 1.3) and degree (ϑ, equation 1.4) of molecular tensor.

$$\eta = \frac{|S_{yy} - S_{xx}|}{S_{zz}} \tag{1.3}$$

$$\vartheta = \sqrt{\frac{2}{3}(S_{xx}^2 + S_{yy}^2 + S_{zz}^2)}, \qquad |S_{zz}| \geq |S_{yy}| \geq |S_{xx}| \tag{1.4}$$

Two angular parameters define the average orientation of the magnetic field with respect to the molecular frame (S_{zz}) and a third angular parameter defines the orientation of the orthogonal principal axis (S_{yy}) which specifies the alignment of asymmetry. Experimentally, these five order tensor parameters can be elucidated provided the measurement of five or more independent RDCs for a fragment with known local helical structure.

Using the order tensor approach to interpret RDC data in terms of structure and dynamics requires that the alignment tensors be measured individually for each rigid sub-structure of the biomolecule target. In this regard, RNA molecules prove to be suitable for this analysis since by nature they can be broken into different sub-structures consisting of locally stable A-form helixes (*104*). Here, order tensors are calculated for each helical domain. Consequently these order tensors are used to determine their relative structure orientation and dynamics.

The average orientation of helical domains can be obtained by superimposing their order tensor frames (*77, 119, 120*) (Figure 1.4A). This step insists that the helical domains share a common view of the magnetic field direction when assembled into a proper structure. However, RDCs are degenerate to 180° rotations around the principal directions of the order tensor (S_{xx}, S_{yy}, and S_{zz}). This results in 4^{n-1} fold degeneracy in orienting *n* fragments. This degeneracy problem can often be overcome in two different ways: (1) measuring RDCs under at least two different alignments (*121, 122*) and (2)

incorporating additional experimental and non-experimental restraints (*117, 123*). The latter method is the more typical solution for nucleic acids.

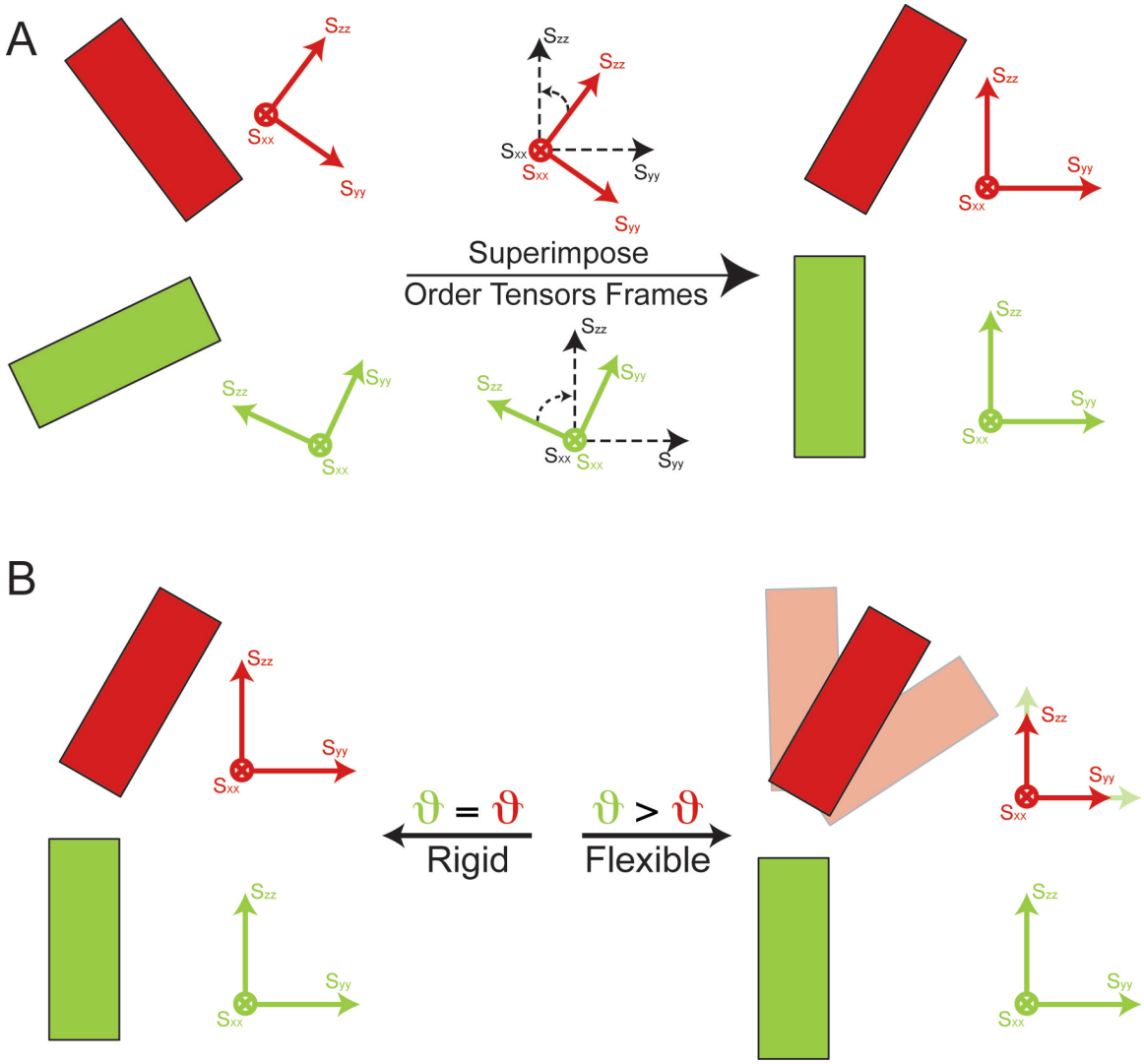

Figure 1.4: Global structure and dynamics determination by RDC analysis. Domain Structural (A) and dynamical (B) characterization

To obtain relative helix motional information over sub-ms timescale, the two principal order tensor parameters (ϑ and η) for each helical domain are compared (*119*) (Figure 1.4B). Two helical domains that are rigid relative to each other will report identical parameters. However, inter-helical motions will lead to differences in the magnitude of the parameters. The degree of order for a given helix (ϑ) will be reduced

relative to the value observed for a helix that dominates total alignment. The internal generalized degree (ϑ_{int}) of order for a pair of helical domains (i and j) is the ratio of the degree of order between i and j and is calculated using the following equation:

$$\vartheta_{int} = \frac{\vartheta_i}{\vartheta_j}, \text{ where } \vartheta_i < \vartheta_j \quad (1.5)$$

This ratio provides a measure of motional amplitudes between helical domains where a $\vartheta_{int} = 1$ corresponds to perfect rigidity and $\vartheta_{int} = 0$ to maximum motions. The asymmetry parameter (η) provides information of the directionality of inter-helical motions with spatially isotropic motions having a smaller effect on the relative helix η values compared to anisotropic motions (*119*).

1.3.2 Spin relaxation

The most common NMR applications to unravel RNA dynamics occurring at the ps-ns timescales is by NMR spin relaxation measurements. Nuclear spin relaxation results from the time dependent stochastic modulation of spin Hamiltonians including the dipole-dipole, chemical shift anisotropy (CSA) and quadrupular Hamiltonians (*124*). A given nuclear spin relaxes back to thermal equilibrium due to fluctuation of the local magnetic field. This fluctuation is a time dependent phenomena related to the internal and overall thermal motions of the molecule. Therefore, the relaxation rates measured for a given nuclei contain dynamical information for that specific site. The most basic NMR application to study ps-ns dynamics is to measure the transverse relaxation rate ($R_2 = 1/T_2$), longitudinal relaxation rate ($R_1 = 1/T_1$) and steady state heteronuclear Overhausser effect (NOE). The R_2 rate, also known as the spin-spin relaxation, describes the decay

rate of the transverse magnetization to zero or the loss of coherence in the XY plane. The R_1 rate, also known as the spin-lattice relaxation rate, describes the recovery rate of the longitudinal (along Z axis) back to its thermal equilibrium state. These two relaxation rates are auto-relaxation rates of the nuclei. In contrast, the NOE is the cross-relaxation rate of a dipolar couple spins like S-H. Here the resonance intensity of spin S will change once the population of spin H is perturbed due to the dipole-dipole cross-relaxation.

The expression of the relaxation rate constants for a given spin S (equal to ^{13}C or ^{15}N) in an S-H system that is subject to chemical shift anisotropy (CSA) interactions of the S spin and dipole-dipole interactions with its bonded H spin are given by the following equations (*54, 125*)

$$\begin{aligned} R_1 &= \frac{d^2}{4}\left[J(\omega_H - \omega_S) + 3J(\omega_S) + 6J(\omega_H + \omega_S)\right] + c^2 J(\omega_S) \\ R_2 &= \frac{d^2}{8}\left[4J(0) + J(\omega_H - \omega_S) + 3J(\omega_S) + 6J(\omega_H) + 6J(\omega_H + \omega_S)\right] \\ &+ \frac{c^2}{6}\left[4J(0) + 3J(\omega_S)\right] + R_{ex} \\ NOE &= 1 + \frac{d^2\gamma_H}{4R_1\gamma_S}\left[6J6J(\omega_H + \omega_S) - J(\omega_H - \omega_S)\right] \end{aligned} \tag{1.6}$$

$$\begin{aligned} d &= \frac{\mu_0 h \gamma_H \gamma_S}{8\pi^2 \left\langle r_{HS}^3 \right\rangle} \\ c &= \frac{\Delta\sigma\omega_S}{\sqrt{3}} \end{aligned} \tag{1.7}$$

where, μ_0 is the permeability of free space, h is Plank's constant, γ_H and γ_S are the gyromagnetic ratios for spins ^1H and S, ω_H and ω_S are the Larmor frequencies of ^1H and S spins, r_{HS} is the H-S bond length, $\Delta\sigma$ is the CSA of the S spin and $J(\omega)$ is the spectral density function. Here the chemical shift tensor is assumed to be asymmetric. The dipole-

dipole interactions of spin S with ^{1}H results from the fluctuation interaction between the S-^{1}H spin pair as the internuclear vector rotates relative to the magnetic field. The CSA interactions of spin S results from the shielding variations from the magnetic field as a consequence of the fluctuating magnetic field experienced by S spin.

The spectral density function is defined as twice of the Fourier transformation of the autocorrelation function *C(t)* and it plays a central role in relaxation theory. The autocorrelation function describes the rotational motions of a bond vector. It measures the probability that a bond vector has the same position relative to the magnetic field at an arbitrary time zero and *t*. Generally, the expression for the spectral density and autocorrelation functions are given by Equations 1.8 and 1.9 respectively (*125*)

$$J(\omega) = 2\int_{0}^{\infty} C(t)\cos(\omega t)dt \tag{1.8}$$

$$C(t) = \frac{1}{5}\left\langle P_2\left(\vec{\mu}_{LF}(0)\cdot\vec{\mu}_{LF}(t)\right)\right\rangle \tag{1.9}$$

where, $\vec{\mu}_{LF}$ describes the laboratory frame orientation of a unit vector connecting two nuclei at time 0 and *t*, and $P_2(x)$ is the second rank Legendre polynomial given by $(3x^2-1)/2$. The shape of the autocorrelation function defines the likelihood of motions on different time scales. For instance, the correlation function of a rigid ^{15}N-^{1}H bond vector within an RNA that is rotating isotropically and has a single characteristic time scale defined as the rotational correlation time of the molecule (τ_m) is given by

$$C(t) = \frac{1}{5}e^{-t/\tau_m} \tag{1.10}$$

In summary, the correlation functions can be related to simple models for rotational of bond vectors and also can be used to separate motions occurring at different time

scales. For example, it can be used to separate internal motions from overall tumbling of a molecule. A model function can be fit to the R_1, R_2 and NOE relaxation data using the model free formalism developed by Lipari and Szabo (*126, 127*). This analysis is widely used to characterize internal motions. Recently it has been successfully applied to characterize ^{13}C and ^{15}N motions in RNA (*78, 128, 129*).

1.3.2.1 Experimental measurements of ^{15}N relaxation

The imino nitrogens in RNA are perfect probes for spin relaxation measurements. Unlike carbon and proton spins, imino nitrogen spins do not possess large homonuclear interactions that could affect relaxation measurements. Unfortunately, imino nitrogens in RNA are only observed when they are protected from exchange with water, such as in canonical Watson-Crick base pairs. The typical NMR pulse sequences used to measure ^{15}N R_1 and R_2 relaxation rates are shown on Figure 1.5. The R_1 and R_2 pulse sequences start with a refocused Insensitive Nucleus Enhanced Polarization Transfer (INEPT), which prepares nitrogen N_x magnetization. In the R_1 experiment, a 90° pulse converts N_x into N_z prior to the relaxation period. The water magnetization is positioned along +z axis. The events proceeding after the relaxation period are the *t1* evolution period, inverse polarization transfer and final detection of imino proton magnetization (Figure 1.5). To suppress the effects of $^{1}H–^{15}N$ dipolar cross-relaxation and ^{15}N CSA/^{1}H $–^{15}N$ dipolar relaxation interference, selective 180° shaped pulses centered on the imino proton region are applied during the relaxation period. The Carr-Purcell-Meiboom-Gill (CPMG) train of 180° pulses is applied during the relaxation period to suppress the effects of chemical exchange (R_{ex}) in the R_2 experiment. Here the CPMG sequence contains a $[0013]^N$ phase

cycling to suppress artifacts arising from off-resonance effects (*130*). Low power train pulses are used to prevent the excitation of the ^{1}H-^{15}N1 (adenine), ^{1}H-^{15}N3 (cytosine) hydrogen bonds. A series of R_1 and R_2 experiments with different lengths of relaxation period are used to achieve the relaxation decay curves.

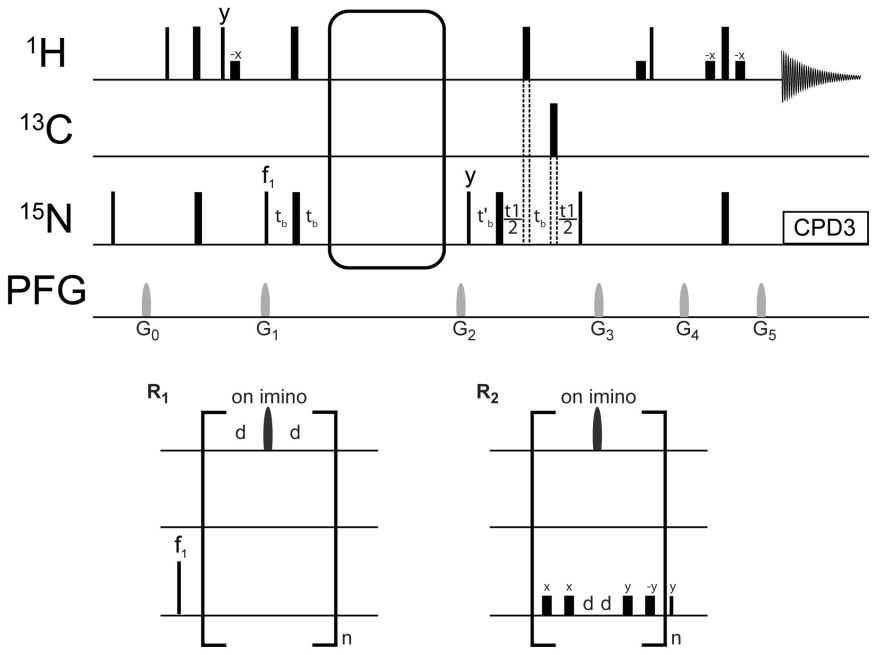

Figure 1.5: Pulse sequence used to measured ^{15}N spin relaxation measurements in RNA.

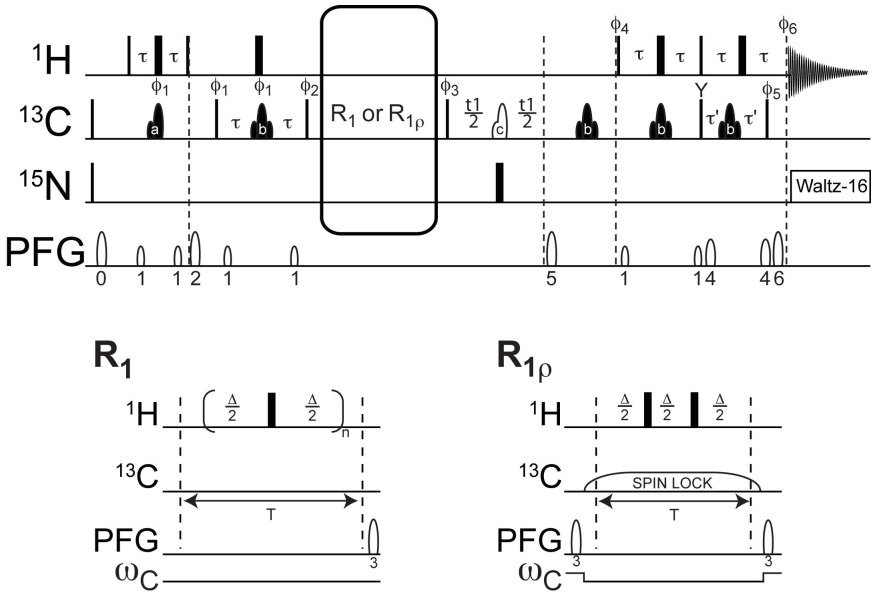

Figure 1.6: Pulse sequence used to measured ^{13}C spin relaxation measurements in RNA

1.3.2.2 Experimental measurements of ^{13}C relaxation

Non-exchangeable carbons are abundant in RNA and thus can be a great source of site-specific dynamical information. Nevertheless, non-exchangeable carbons possess sizable CSA and C-C interactions that affect the relaxation measurements. For example, CC scalar couplings range from 8-12 Hz for 3-4 bond couplings in the aromatic ring and for directly bonded carbons the range is >80 Hz (*131*). The NMR pulse sequences used to measure ^{13}C R_1 and rotating-frame ($R_{1\rho}$) relaxation rates are shown on Figure 1.6. The R_1 and $R_{1\rho}$ pulse sequences start with a refocused INEPT transfer, which prepares carbon C_x magnetization. Selective excitation during the INEPT step is necessary to prevent the buildup of contributions from unwanted neighboring protonated carbons. In addition, the destruction of the equilibrium carbon magnetization prior to the first 90° pulse suppresses any cross-relaxation to quaternary carbons in the aromatic ring. During the relaxation period, the spin of interest is allowed to decay for a time *t* while carefully preventing any unwanted cross-correlated relaxation mechanisms that could affect the relaxation rates.

To prevent unwanted proton cross-relaxation, ^{13}C-^{1}H dipolar and CSA interactions, a train of hard 180° pulses is applied on the proton dimension. Also, adiabatic half passages are used to accurately align the $\pm C_z$ magnetization to and from the effective tilt angle θ at the beginning and end of the relaxation period. Following the relaxation period, the indirect dimension is encoded with the chemical shift of the heteronuclear spin. Pulses to selectively refocus the ^{13}C magnetization are then used to eliminate C-C scalar coupling evolution (these are denoted as *b* and *c* in the pulse sequence). Spin State Selective Coherence Transfer (S_3CT) (*132*) is then applied to return the magnetization back to the directly bonded ^{1}H before detection. High power off-resonance spinlocks are used to minimize contributions from chemical exchange and to suppress any Hartmann Hahn type transfers to scalar coupled ^{13}C spins in the $R_{1\rho}$ experiments. Hartman-Hahn (A_{HAHA}) interactions between homonuclear scalar coupled spins can be reduced up to 1% by choosing offsets and spinlock powers that minimize these interactions (*133*). The expression to calculate A_{HAHA} interactions is given by (*133*)

$$A_{HAHA} = \left(1 + \left(\frac{\omega_{eff,I} - \omega_{eff,S}}{J_{IS}\left(1 + \cos(\theta_I - \theta_S)\right)/2}\right)^2\right)^{-1} \tag{1.11}$$

where J_{IS} is the scalar coupling constant between spins S and I, $\omega_{eff,X}=(\omega_1^2 + \Omega_X^2)^{1/2}$ is the effective spinlock strength at spin X (I or S), $\theta_X = \text{atan}(\omega_1/\Omega_X)$ is the tip angle of the magnetization of spin X with respect to the static magnetic field. For spinlock powers higher than 1000 Hz, the effects of J_{CH} evolution and CH-dipole/CSA cross-correlated relaxation are effectively suppressed by two 180° pulses placed at times T/4 and 3T/4 during the spinlock period (*134, 135*).

A series of R_1 and $R_{1\rho}$ experiments with different lengths of relaxation period was used to achieve the relaxation decay curves. The R_2 rates are calculated using the following equation:

$$R_{1\rho} = R_1 \cos^2 \theta + R_2 \sin^2 \theta \quad (1.12)$$

where, $\theta = \text{atan}(\omega_1/\Omega)$ is the effective tilt angle of the spinlock field, ω_1 is the spinlock field power in Hz and Ω is resonance offset from the spinlock carrier frequency in Hz.

1.3.3 Chemical exchange

A better understanding of nucleic acid biological function requires not only structural information but also knowledge of the dynamical properties at the fast (ps-ns) and slow (μs-ms) timescales of the molecule of interest. NMR spin relaxation measurements, as discussed above, can be used to unravel RNA dynamics occurring at fast timescales. Alternate NMR techniques have been used to study nucleic acid dynamics occurring at slower time scales such as base pair opening (*136*), base flipping (*137*), ligand binding (*80*) and sugar pucker conformational averaging (*138*). Recently, two different classes of ^{13}C relaxation dispersion experiments employing the same techniques used to measure transverse relaxation (discuss on section 1.3.2.2) have been applied to study conformational exchange dynamics in RNA (*74, 139-142*).

The first class of ^{13}C relaxation dispersion experiments monitors the apparent transverse relaxation rate ($R_{2,eff}$) as a function of the spacing between refocusing pulses using CPMG sequences. During the relaxation block of the CPMG experiment, as the spacing between the refocusing pulses becomes tighter, the magnetization of the spins refocuses faster than they can exchange consequently suppressing any chemical exchange process. If we define the CPMG train as $(\delta\text{-}180°\text{-}\delta)_N$ (where $_N$ is an integer number, δ is

the delay between 180° pulses of the CPMG train) and assume that the exchange is fast, we can describe $R_{2,eff}$ as follows (*57, 143, 144*):

$$R_{2,eff} = \frac{1}{2}\left(R_{2,A} + R_{2,B} + k_{ex} - \frac{1}{2\delta}\arccos h(D_+ \cosh \eta_+ - D_- \cosh \eta_- \right)$$

(1.13)

where,

$$\begin{aligned} D_\pm &= \frac{1}{2}\left(\frac{\psi + 2\Delta\omega^2\omega_S^2}{\sqrt{\psi^2 + \zeta^2}} \right) \\ \eta_\pm &= \delta\sqrt{2}\sqrt{\sqrt{\psi^2 + \zeta^2} \pm \psi} \\ \psi &= (R_{2,A} - R_{2,B} - p_A k_{ex} + p_B k_{ex})^2 - \Delta\omega^2\omega_S^2 + 4p_A p_B k_{ex}^2 \\ \zeta &= 2\Delta\omega\omega_S(R_{2,A} - R_{2,B} - p_A k_{ex} + p_B k_{ex}) \end{aligned} \qquad (1.14)$$

and $\Delta\omega = \Omega_A - \Omega_B$ is the chemical shift difference between states A and B, $R_{2,A}$ and $R_{2,B}$ are the intrinsic relaxation rates, p_A and p_B are the populations, k_{ex} is the exchange rate, and ω_s is the Larmor frequency for the heteronucleus. While this experiment is routinely applied in protein systems, is not well suited to study chemical exchange in nucleic acids due to the presence of abundant scalar coupling networks. For instance, even the scalar coupling size of nitrogen spins to their hydrogen bonded partners, which is ~7 Hz can cause significant artifacts (*145*). A way of suppressing this effect is to use low power refocusing pulses to prevent $^1J_{NN}$ coupling evolution during the relaxation delay. Nevertheless, this can lead to off-resonance effects (*146*). Different methods have been developed to suppress and correct these errors (*130, 147*) and this progress have been significant for probing ^{15}N spin dynamics for large RNAs (*78, 128, 148*). Another method that has been implemented in order to use CPMG experiments to study chemical exchange in the RNA sugars is site-specific labeling (*139, 149*).

The second class of ^{13}C relaxation dispersion experiments used to study chemical exchange, monitors the rotating frame relaxation rate ($R_{1\rho}$) as a function of the strength and/or offset of applied radio frequency fields (*150*). During the relaxation block, the higher the spinlock field applied, the more the chemical exchange is suppressed. This dependence of $R_{1\rho}$ on the spinlock field strength will give information on the lifetime of the chemical exchange, site populations and Larmor frequency of the spins affected by chemical kinetics. Recently, expressions have been developed to explain exchange outside the fast exchange regime (*71, 151, 152*). The lack of expressions for events occurring outside fast exchange was primarily due to the relatively strong spinlock field power ($\omega_1/2\pi$) lower limit of approximately 1-2 kHz that automatically almost completely suppressed exchange events lower than 300 μs. The suppression of cross-correlation between dipole-dipole, chemical shift anisotropy interactions and the elimination of evolution of *J* couplings during spinlock powers were some of the difficulties that prevented using weaker radio frequency fields (*153*). However, significant advances on $R_{1\rho}$ relaxation dispersion experiments now permit the use of lower spinlock power up to 25 Hz without distortion of the relaxation decay (*153-155*). This has opened the window of events that could be studied outside the fast exchange limit.

The effect of $R_{1\rho}$ in the fast exchange limit can be expressed by the following equation:

$$R_{1\rho} = R_{1\rho,\infty} + \sin^2\theta \frac{\Phi_{ex} k_{ex}}{k_{ex}^2 - \omega_{eff}^2} \quad , \tag{1.15}$$

where $\Phi_{ex} = p_A p_B \Delta\omega^2$, k_{ex} is the sum of the forward and reverse microscopic rate constants ($k_A + k_B$) for two-site exchange, $R_{1\rho,\infty}$ is the intrinsic relaxation rate given by

equation 1.12, $\omega_{eff} = \sqrt{\omega_1^2 + \Omega_2}$ is the effective spinlock power of the nucleus at the population weighted average resonance offset from the spinlock frequency and $\Omega = \Omega_A p_A + \Omega_B p_B$. A general formula for $R_{1\rho}$ that is valid for all timescales and is very accurate for a two state system where the populations are highly skewed ($p_A >>> p_B$) was generated from approximate solutions to the Bloch-McConnell (*71*).

$$R_{1\rho} = R_{1\rho,\infty} + \frac{\sin^2\theta p_A p_B \Delta\omega^2 k_{ex}}{\frac{\omega_A^2\omega_B^2}{\omega_{eff}^2} + k_{ex}} \approx R_{1\rho,\infty} + \frac{\sin^2\theta p_A p_B \Delta\omega^2 k_{ex}}{\Omega_B^2 + \omega_1^2 + k_{ex}^2} \tag{1.16}$$

Here the exchange contribution depends on the effective field for the nuclear spin on the less populated site B. In addition when the spinlock is on resonance with the less populated state ($\Omega_B = 0$) we can get the most information on chemical exchange.

An extension from the asymmetric population formula for $R_{1\rho}$ that is valid for all timescales can be generated from approximate solutions to the Bloch-McConnell or the stochastic Liouville equation for a two state system equation. The most accurate of these solutions uses the Laguerre's method for polynomial root finding for a two-site exchange system (Equation 1.17) (*71, 151*). This equation has only three unknowns (k_{ex}, p_B and $\Delta\omega$) and it also includes additional parameters for the effective spinlock strength for each state.

$$R_{1\rho} = R_{1\rho,\infty} + \frac{\sin^2\theta p_A p_B \Delta\omega^2 k_{ex}}{\frac{\omega_A^2\omega_B^2}{\omega_{eff}^2} + k_{ex} - \sin^2\theta p_A p_B \Delta\omega^2 k_{ex}\left(1 + \frac{2k_{ex}(p_A\omega_A^2 + p_B\omega_B^2)}{\omega_A^2\omega_B^2 + \omega_{eff}^2 k_{ex}^2}\right)} \tag{1.17}$$

Besides the aforementioned equations, there are expressions for $R_{1\rho}$ that have been generated for other different cases such as when the two populations are equal ($p_A = p_B$),

or more than two site exchange is present (this one is more complicated to solve due to the number of variables)

1.4 References

1. Thomas, J. R., and Hergenrother, P. J. (2008) Targeting RNA with small molecules, *Chemical Reviews 108*, 1171-1224.
2. Al-Hashimi, H. M. (2005) Dynamics-Based Amplification of RNA Function and Its Characterization by Using NMR Spectroscopy, *Chembiochem 6*, 1506-1519.
3. Micura, R., and Hobartner, C. (2003) On secondary structure rearrangements and equilibria of small RNAs, *Chembiochem 4*, 984-990.
4. Draper, D. E. (2004) A guide to ions and RNA structure, *RNA 10*, 335-343.
5. Leulliot, N., and Varani, G. (2001) Current topics in RNA-protein recognition: Control of specificity and biological function through induced fit and conformational capture, *Biochemistry 40*, 7947-7956.
6. Vicens, Q., and Westhof, E. (2003) RNA as a drug target: the case of aminoglycosides, *Chembiochem 4*, 1018-1023.
7. Sucheck, S. J., and Wong, C. H. (2000) RNA as a target for small molecules, *Curr Opin Chem Biol 4*, 678-686.
8. Tor, Y. (2003) Targeting RNA with small molecules, *Chembiochem 4*, 998-1007.
9. Hermann, T. (2005) Drugs targeting the ribosome, *Current Opinion in Structural Biology 15*, 355-366.
10. UNAIDS/WHO. (2009) Global facts and figures 2009.
11. UNAIDS/WHO. (2009) AIDS epidemic update 2009.
12. Reeves, J. D., and Doms, R. W. (2002) Human immunodeficiency virus type 2, *Journal of General Virology 83*, 1253-1265.
13. Klimas, N., Koneru A.O.B, Fletcher, M. A. (2008) Overview of HIV, *Psychosomatic medicine 70*, 523-530.
14. Bannwarth, S., and Gatignol, A. (2005) HIV-1 TAR RNA: the target of molecular interactions between the virus and its host, *Curr HIV Res 3*, 61-71.
15. Muesing, M. A., Smith, D. H., and Capon, D. J. (1987) Regulation of mRNA accumilation by a human immunodeficiency virus trans-activator protein., *Cell 48*, 691-701.
16. Hamy, F., Felder, E. R., Heizmann, G., Lazdins, J., Aboul-ela, F., Varani, G., Karn, J., and Klimkait, T. (1997) An inhibitor of the Tat/TAR RMA interaction that effectively suppresses HIV-1 replication, *Proccedings of the National Academy of Sciences of the United States of America 94*, 3548-3553.
17. Cullen, B. R. (1998) HIV-1 auxiliary proteins: making connections in a dying cell, *Cell 93*, 685-692.
18. Dorion, D., Bonnet, M. C., Bannwarth, S., Gatignal, A., Meurs, E. F., and Vaquero, C. (2003) The TAR RNA-binding protein, TRBP, stimulates the expression of TAR-containing RNAs in vitro and in vivo independently of its ability to inhibit the dsRNA-dependent kinase PKR, *Journal of Biological Chemistry 278*, 4440-4448.

19. Krebs, A., Ludwig, V., Boden, O., and Gobel, M. W. (2003) Targeting the HIV trans-activation responsive region--approaches towards RNA-binding drugs, *Chembiochem 4*, 972-978.
20. Murchie, A. I., Davis, B., Isel, C., Afshar, M., Drysdale, M. J., Bower, J., Potter, A. J., Starkey, I. D., Swarbrick, T. M., Mirza, S., Prescott, C. D., Vaglio, P., Aboul-ela, F., and Karn, J. (2004) Structure-based drug design targeting an inactive RNA conformation: exploiting the flexibility of HIV-1 TAR RNA, *J Mol Biol 336*, 625-638.
21. Yang, M. (2005) Discoveries of Tat-TAR interaction inhibitors for HIV-1, *Current drug targets. Infectious disorders 5*, 433-444.
22. Froeyen, M., and Herdewijn, P. (2002) RNA as a target for drug design, the example of Tat-TAR interaction, *Curr Top Med Chem 2*, 1123-1145.
23. Weeks, K. M., Ampe, C., Schultz, S. C., Steitz, T. A., and Crothers, D. M. (1990) Fragments of the HIV-1 Tat protein specifically bind TAR RNA, *Science 249*, 1281-1285.
24. Churcher, M. J., Lamont, C., Hamy, F., Dingwall, C., Green, S. M., Lowe, A. D., Butler, P. J. G., Gait, M. J., and Karn, J. (1993) High-Affinity Binding of Tar Rna By the Human-Immunodeficiency- Virus Type-1 Tat Protein Requires Base-Pairs in the Rna Stem and Amino-Acid-Residues Flanking the Basic Region, *Journal of Molecular Biology 230*, 90-110.
25. Weeks, K. M., and Crothers, D. M. (1991) Rna Recognition By Tat-Derived Peptides - Interaction in the Major Groove, *Cell 66*, 577-588.
26. Tao, J., and Frankel, A. D. (1992) Specific binding of arginine to TAR RNA, *Proc Natl Acad Sci U S A 89*, 2723-2726.
27. Calnan, B. J., BiNCALANA, S., HUDSON, D. and FRANKEL, A. D. (1991) Analysis of arginine-rich peptides from the HIV Tat protein reveals unusual features of RNA-protein recognition, *Genes & Development 5*, 201-210.
28. Aboul-ela, F., Karn, J., and Varani, G. (1996) Structure of HIV-1 TAR RNA in the absence of ligands reveals a novel conformation of the trinucleotide bulge, *Nucleic Acids Research 24*, 3974-3981.
29. Aboul-ela, F., Karn, J., and Varani, G. (1995) The Structure of the Human-Immunodeficiency-Virus Type-1 Tar RNA Reveals Principles of RNA Recognition By Tat Protein, *Journal of Molecular Biology 253*, 313-332.
30. Puglisi, J. D., Tan, R., Calnan, B. J., Frankel, A. D., and Williamson, J. R. (1992) Conformation of the TAR RNA-arginine complex by NMR spectroscopy, *Science 257*, 76-80.
31. Al-Hashimi, H. M., Gosser, Y., Gorin, A., Hu, W., Majumdar, A., and Patel, D. J. (2002) Concerted motions in HIV-1 TAR RNA may allow access to bound state conformations: RNA dynamics from NMR residual dipolar couplings, *J Mol Biol 315*, 95-102.
32. Ippolito, J. A., and Steitz, T. A. (1998) A 1.3-angstrom resolution crystal structure of the HIV-1 trans- activation response region RNA stem reveals a metal ion-dependent bulge conformation, *Proceedings of the National Academy of Sciences of the United States of America 95*, 9819-9824.

33. Faber, C., Sticht, H., Schweimer, K., and Rosch, P. (2000) Structural rearrangements of HIV-1 Tat-responsive RNA upon binding of neomycin B, *J Biol Chem 275*, 20660-20666.
34. Du, Z., Lind, K. E., and James, T. L. (2002) Structure of TAR RNA complexed with a Tat-TAR interaction nanomolar inhibitor that was identified by computational screening, *Chem Biol 9*, 707-712.
35. Davis, B., Afshar, M., Varani, G., Murchie, A. I., Karn, J., Lentzen, G., Drysdale, M., Bower, J., Potter, A. J., Starkey, I. D., Swarbrick, T., and Aboul-ela, F. (2004) Rational design of inhibitors of HIV-1 TAR RNA through the stabilisation of electrostatic "hot spots", *J Mol Biol 336*, 343-356.
36. Blount, K. F., Tor, Y., Hamasaki, K., and Ueno, A. (2003) Using pyrene-labeled HIV-1 TAR to measure RNA-small molecule binding
Aminoglycoside antibiotics, neamine and its derivatives as potent inhibitors for the RNA-protein interactions derived from HIV-1 activators, *Nucleic Acids Res 31*, 5490-5500.
37. Williamson, J. R. (2008) Biophysical studies of bacterial ribosome assembly, *Current Opinion in Structural Biology 18*, 299-304.
38. Beringer, M., and Rodnina, M. V. (2007) The ribosomal peptidyl transferase, *26 3*, 311.
39. Daviter, T., Gromadski, K. B., and Rodnina, M. V. (2006) The ribosome's response to codon-anticodon mismatches, *Biochimie 88*, 1001-1011.
40. Ogle, J. M., Brodersen, D. E., Clemons Jr., W. M., Tarry, M. J., Carter, A. P., and Ramakrishnan, V. (2001) Recognition of Cognate Transfer RNA by the 30S Ribosomal Subunit, *Science 292*, 897-902.
41. Shandrick, S., Zhao, Q., Han, Q., Ayida, B. K., Takahashi, M., Winters, G. C., Simonsen, K. D., Vourloumis, D., and Hermann, T. (2004) Monitoring molecular recognition of the ribosomal decoding site, *Angew Chem Int Ed Engl 43*, 3177-3182.
42. Ogle, J., Carter, A. P., and Ramakrishnan, V. (2003) Insights into the decoding mechanism from recent ribosome structures, *Trends In Biochemical Science 28*, 259-266.
43. Noller, H. F. (1991) Ribosomal RNA and translation, *Annual Review of Biochemistry 60*, 191-227.
44. Bottger, E. C., Springer, B., Prammananan, T., Kidan, Y., and Sander, P. (2001) Structural basis for selectivity and toxicity of ribosomal antibiotics, *EMBO reports 2*, 318-323.
45. Recht, M. I., and Puglisi, J. D. (2001) Aminoglycoside resistance with homogeneous and heterogeneous populations of antibiotic-resistant ribosomes, *Antimicrobial Agents and Chemotherapy 45*, 2414-2419.
46. Hermann, T. (2006) A-site model RNAs, *Biochimie 88*, 1021-1026.
47. Prammananan, T., Sander, P., Brown, B. A., Frischkorn, K., Onyi, G.O., Zhang, Y., Bottger, E. C., Wallace, R. J. (1998) A single 16S ribosomal RNA substitution is responsible for resistance to amikacin and other 2-deoxystreptamine aminoglycosides in Mycobacterium abscessus and Mycobacterium chelonae, *The Journal of Infectious Diseases 177*, 1573-1581.

48. Sander, P., Prammananan, T., and Bottger, E. C. (1996) Introducing mutations into a chromosomal rRNA gene using genetically modified eubacterial host with a single rRNA openron, *Molecular Microbiology 22*, 841-848.
49. Recht, M. I., Douthwaite, S., and Puglisi, J. D. (1999) Basis for prokaryotic specificity of action of aminoglycoside antibiotics, *The Embo Journal 18*, 3133-3138.
50. Recht, M. I., Douthwaite, S., Dahlquist, K. D., and Puglisi, J. D. (1999) Effect of Mutations in the A Site of 16 S rRNA on Aminoglycoside Antibiotic-Ribosome Interaction, *Journal of Molecular Biology 286*, 33-43.
51. Gregory, S. T., Carr, J. F., Rodriguez-Correa, D., and Dahlberg, A. E. (2005) Mutational analysis of 16S and 23S rRNA genes of Thermus thermophilus, *Journal of Bacteriology 187*, 4804-4812.
52. Kaul, M., Barbieri, C. M., and Pilch, D. S. (2006) Aminoglycoside-Induce Reduction in Nucleotide Mobility at the Ribosomal RNA A-Site as a Potentially Key Determinant of Antibacterial Activity, *Journal of the American Chemical Society 128*, 1261-1271.
53. Wüthrich, K. (1986) *NMR of Proteins and Nucleic Acids*, Wiley, New York.
54. Palmer, A. G., 3rd. (2004) NMR characterization of the dynamics of biomacromolecules, *Chemical Reviews 104*, 3623-3640.
55. Carlomagno, T. (2005) Ligand-target interactions: what can we learn from NMR?, *Annual Reviews of Biophysics and Biomolecular Structure 34*, 245-266.
56. Palmer, A. G., Williams, J., and McDermott, A. (1996) Nuclear magnetic resonance studies of biopolymer dynamics, *Journal of Physical Chemistry 100*, 13293-13310.
57. Palmer III, A. G., Kreoenke, C. D., and Loria, P. J. (2001) Nuclear Magnetic Resonance Methods for Quantifying Microsecond-to-Millisecond Motions in Biological Macromolecules *Methods in Enzymology 339*, 204-238.
58. Akke, M. (2002) NMR methods for characterizing microsecond to millisecond dynamics in recognition and catalysis, *Current Opinion in Structural Biology 12*, 642-647.
59. Zuiderweg, E. R. P. (2002) Mapping protein-protein interactions in solution by NMR Spectroscopy, *Biochemistry 41*, 1-7.
60. Purcell, E. M., Torrey, H. C., and Pound, R. V. (1946) Resonance Absorption by Nuclear Magnetic Moments in a Solid, *Physical Review 69*, 37-38.
61. Bloch, F., Hansen, W. W., and Packard, M. (1946) Nuclear Induction, *Physical Review 69*, 127.
62. Ernst, R. R., and Andersen, A. A. (1966) Application of Fourier Transform Spectroscopy to Magnetic Resonance, *Review of Scientific Instruments 37*, 93-102.
63. Jeener, J. (1971) in *Ampere Summer School*, Basko Polje, Yugoslavia.
64. Vuister, G. M., Boelens, R., and Kaptein, R. (1988) Nonselective Three-Dimensional NMR Spectroscopy. The 3D NOE-HOHAHA Experiment *Journal of Magnetic Resonance 80*, 176-185.
65. Oschkinat, H., Griesinger, C., Kraulis, P. J., Sorensen, O. W., Ernst, R. R., Gronenborn, A. M., and Clore, G. M. (1988) Three-dimensional NMR spectroscopy of a protein in solution, *Nature 332*, 374-376.

66. McDonald, C. C., Phillips, W. D., and Penman, S. (1964) Nucleic Acids - Nuclear Magnetic Resonance Study, *Science 144*, 1234-1237.
67. McTague, J. P., Ross, V., and Gibbs, J. H. (1964) Nuclear Magnetic Resonance Study of Synthetic Polynucleotides and transfer RNA, *Biopolymers 2*, 163-173.
68. Smith, I. C. P., Yamane, T., and Shulman, R. G. (1968) Proton Magnetic resonance of transfer RNA, *Science 159*, 1360-1361.
69. Kearns, D. R., Patel, D. J., and Shulman, R. G. (1971) High resolution nuclear magnetic resonance studies of hydrogen bonded protons of tRNA in water, *Nature 229*, 338-339.
70. Reid, B., and Hurd, R. E. (1977) Application of High-Resolution Nuclear Magnetic Resonance Spectroscopy in the Study of Base Pairing and the Solution Structure of Transfer RNA, *Accounts Chem. Res. 10*, 396-402.
71. Palmer III, A. G., and Massi, F. (2006) Characterization of the Dynamics of Biomacromolecules Using Rotating-Frame Spin Relaxation NMR Spectroscopy, *Chemical Reviews 106*, 1700-1719.
72. Kay, L. E. (1998) Protein dynamics from NMR, *Nature Structural Biology 5*, 513-517.
73. Vallurupalli, P., Hansen, D. F., and Kay, L. E. (2008) Structures of invisible, excited protein states by relaxation dispersion NMR spectroscopy *Proceedings National Academy of Science USA 105*, 11766-11771.
74. Hansen, A. L., Nikolova, E.N., Casiano-Negroni, A. and Al-Hashimi, H. M. (2009) Extending the range of microsecond-to-millisecond chemical exchange detected in labeled and unlabeled nucleic acids by selective carbon R(1rho) NMR spectroscopy., *Journal of the American Chemical Society 131*, 3818-3819.
75. Akke, M., and III, A. G. P. (1996) Monitoring macromolecular motions on microsecond to millisecond time scales by R(1)rho-R(1) constant relaxation time NMR spectroscopy, *J. Am. Chem. Soc. 118*, 911-912.
76. Kay, L. E. (2008) Using relaxation dispersion NMR spectroscopy to determine structures of excited, invisible protein states, *Journal of Biomolecular NMR 41*, 113-120.
77. Al-Hashimi, H. M., and Patel, D. J. (2002) Residual dipolar couplings: Synergy between NMR and structural genomics, *Journal of Biomolecular Nmr 22*, 1-8.
78. Getz, M. M., Andrews, A. J., Fierke, C. A., and Al-Hashimi, H. M. (2007) Structural plasticity and Mg2+ binding properties of RNase P P4 from combined analysis of NMR residual dipolar couplings and motionally decoupled spin relaxation, *RNA 13*, 251-266.
79. Led, J. J., Gesmar, H., and Abildgaard, F. (1989) Applicability of magnetization transfer nuclear magnetic resonance to study chemical exchange reactions, *Methods in Enzymology 176*, 311-329.
80. Latham, M. P., Zimmermann, G. R., and Pardi, A. (2009) NMR chemical exchange as a probe for ligand-binding kinetics in a theophylline-binding RNA aptamer, *Journal of the American Chemical Society 131*, 5052-5053.
81. Wijmenga, S. S., and van Buuren, B. N. M. (1998) The use of NMR methods for conformational studies of nucleic acids, *Progress in Nuclear Magnetic Resonance Spectroscopy 32*, 287-387.

82. Furtig, B., Richter, C., Wohnert, J., and Schwalbe, H. (2003) NMR spectroscopy of RNA, *Chembiochem 4*, 936-962.
83. Sklenar, V., Peterson, R.D, Rejente, M.R., and Feigon, J. (1993) 2-Dimensional And 3- Dimensional Hcn Experiments For Correlating Base And Sugar Resonances In N-15,C-13-Labeled Rna Oligonucleotides., *Journal of Biomolecular NMR 3*, 721-727.
84. Simon, B., Zanier, K., and Sattler, M. (2001) A TROSY relayed HCCH-COSY experiment for correlating adenine H2/H8 resonances in uniformly C-13-labeled RNA molecules, *Journal of Biomolecular NMR 20*, 173-176.
85. Wohnert, J., Gorlach, M., and Schwalbe, H. (2003) Triple resonance experiments for the simultaneous correlation of H6/H5 and exchangeable protons of pyrimidine nucleotides in 13C,15N-labeled RNA applicable to larger RNA molecules, *Journal of Biomolecular NMR 26*, 79-83.
86. Sklenar, V., Dieckmann, T., Butcher, S. E., and Feigon, J. (1996) Through-bond correlation of imino and aromatic resonances in 13C-, 15N-labeled RNA via heteronuclear TOCSY, *Journal of Biomolecular NMR 7*, 83-87.
87. Latham, M. P., Brown, D. J., McCallum, S. A., and Pardi, A. (2005) NMR Methods for Studying the Structure and Dynamics of RNA, *Chembiochem 6*, 1492-1505.
88. Pervushin, K., Ono, A., Fernandez, C., Szyperski, T., Kainosho, M., and Wuthrich, K. (1998) NMR scaler couplings across Watson-Crick base pair hydrogen bonds in DNA observed by transverse relaxation optimized spectroscopy, *Proceedings of the National Academy of Sciences of the United States of America 95*, 14147-14151.
89. Dingley, A. J., and Grzesiek, S. (1998) Direct observation of hydrogen bonds in nucleic acid base pairs by internucleotide (2)J(NN) couplings, *Journal of the American Chemical Society 120*, 8293-8297.
90. Pellecchia, M. (2005) Solution nuclear magnetic resonance spectroscopy techniques for probing intermolecular interactions, *Chemistry & Biology 12*, 961-971.
91. Casiano-Negroni, A., Sun, X., and Al-Hashimi, H. M. (2007) Probing Na(+)-Induced Changes in the HIV-1 TAR Conformational Dynamics Using NMR Residual Dipolar Couplings: New Insights into the Role of Counterions and Electrostatic Interactions in Adaptive Recognition., *Biochemistry 46*, 6525-6535.
92. Sun, X., Zhang, Q., and Al-Hashimi, H. M. (2007) Resolving fast and slow motions in the internal loop containing stem-loop 1 of HIV-1 that are modulated by Mg2+ binding: role in the kissing-duplex structural transition, *Nucleic Acids Research 35*, 1698-1713.
93. Legault, P., Hoogstraten, C. G., Metlitzky, E., and Pardi, A. (1998) Order, Dynamics and Metal-binding in the Lead-dependent Ribozyme, *Journal of Molecular Biology 284*, 325.
94. Koutmou, K. S., Casiano-Negroni, A., Getz, M. M., Pazicni, S., Andrews, A. J., Penner-Hahn, J. E., Al-Hashimi, H. M., and Fierke, C. A. (2010) NMR and XAS reveal an inner-sphere metal binding site in the P4 helix of the metallo-ribozyme ribonuclease P *Proceedings National Academy of Science USA 107*, 2479-2484.

95. Butcher, S. E., Allain, F. H., and Feigon, J. (2000) Determination of metal ion binding sites within the hairpin ribozyme domains by NMR, *Biochemistry 39*, 2174-2182.
96. Gonzalez, R. L., and Tinoco, I. (2001) Identification and characterization of metal ion binding sites in RNA, *Methods in Enzymology 338*, 421-443.
97. Kieft, J. S., and Tinoco, I. (1997) Solution structure of a metal-binding site in the major groove of RNA complexed with cobalt (III) hexammine, *Structure 5*, 713-721.
98. Colmenarejo, G., and Tinoco, I. (1999) Structure and thermodynamics of metal binding in the P5 helix of a group I intron ribozyme, *Journal of Molecular Biology 290*, 119-135.
99. Rudisser, S., and Tinoco, I. (2000) Solution structure of Cobalt(III)hexammine complexed to the GAAA tetraloop, and metal-ion binding to G.A mismatches, *Journal of Molecular Biology 295*, 1211-1223.
100. Schmitz, M., and Tinoco, I., Jr. (2000) Solution structure and metal-ion binding of the P4 element from bacterial RNase P RNA, *Rna 6*, 1212-1225.
101. Meyer, B., and Peters, T. (2003) NMR Spectroscopy Techniques for Screening and Identifying Ligand Binding to Protein Receptors, *Angew Chem Int Ed Engl 42*, 864-890.
102. Prestegard, J. H., Al-Hashimi, H. M., and Tolman, J. R. (2000) NMR structures of biomolecules using field oriented media and residual dipolar couplings, *Quarterly Reviews of Biophysics 33*, 371-424.
103. Prestegard, J. H., Bougault, C. M., and Kishore, A. I. (2004) Residual Dipolar Couplings in structure determination of biomolecules, *Chemical Reviews 104*, 3519-3540.
104. Getz, M. M., Sun, Y., Casiano-Negroni, A., Zhang, Q., and Al-Hashimi, H. M. (2007) NMR studies of RNA dynamics and structural plasticity using NMR residual dipolar couplings, *Biopolymers 86*, 384-402.
105. Tjandra, N., and Bax, A. (1997) Direct measurement of distances and angles in biomolecules by NMR in a dilute liquid crystalline medium, *Science 278*, 1111-1114.
106. Ottiger, M., and Bax, A. (1998) Determination of relative N-H-N N-C ', C-alpha-C ', andC(alpha)-H-alpha effective bond lengths in a protein by NMR in a dilute liquid crystalline phase, *Journal of the American Chemical Society 120*, 12334-12341.
107. Tycko, R., Blanco, F. J., and Ishii, Y. (2000) Alignment of biopolymers in strained gels: A new way to create detectable dipole-dipole couplings in high resolution biomolecular NMR, *J. Am. Chem. Soc. 122*, 9340-9341.
108. Sass, H. J., Musco, G., Stahl, S. J., Wingfield, P. T., and Grzesiek, S. (2000) Solution NMR of proteins within polyacrylamide gels: Diffusional properties and residual alignment by mechanical stress or embedding of oriented purple membranes, *Journal of Biomolecular Nmr 18*, 303-309.
109. Hansen, M. R., Mueller, L., and Pardi, A. (1998) Tunable alignment of macromolecules by filamentous phage yields dipolar coupling interactions, *Nature Structural Biology 5*, 1065-1074.

110. Hansen, M. R., Hanson, P., and Pardi, A. (2000) Filamentous bacteriophage for aligning RNA, DNA, and proteins for measurement of nuclear magnetic resonance dipolar coupling interactions, *Methods in Enzymology 317*, 220-240.
111. Clore, G. M., Starich, M. R., and Gronenborn, A. M. (1998) Measurement of residual dipolar couplings of macromolecules aligned in the nematic phase of a colloidal suspension of rod- shaped viruses, *Journal of the American Chemical Society 120*, 10571-10572.
112. Wu, B., Petersen, M., Girard, F., Tessari, M., and Wijmenga, S. (2006) Prediction of molecular alignment of nucleic acids in aligned media, *Journal of Biomolecular NMR 35*, 103-115.
113. Zweckstetter, M., and Bax, A. (2001) Characterization of molecular alignment in aqueous suspensions of Pf1 bacteriophage, *J Biomol NMR 20*, 365-377.
114. Varani, G., Aboulela, F., and Allain, F. H. T. (1996) NMR investigation of RNA structure, *Progress in Nuclear Magnetic Resonance Spectroscopy 29*, 51-127.
115. Clore, G. M., Starich, M. R., Bewley, C. A., Cai, M. L., and Kuszewski, J. (1999) Impact of residual dipolar couplings on the accuracy of NMR structures determined from a minimal number of NOE restraints, *Journal of the American Chemical Society 121*, 6513-6514.
116. Bewley, C. A., Gustafson, K. R., Boyd, M. R., Covell, D. G., Bax, A., Clore, G. M., and Gronenborn, A. M. (1998) Solution structure of cyanovirin-N, a potent HIV-inactivating protein, *Nature Structural Biology 5*, 571-578.
117. Mollova, E. T., Hansen, M. R., and Pardi, A. (2000) Global structure of RNA determined with residual dipolar couplings, *Journal of the American Chemical Society 122*, 11561-11562.
118. Saupe, A. (1968) Recent results in the field of liquid crystals, *Angew. Chem., Int. Ed. Engl. 7*, 97-112.
119. Tolman, J. R., Al-Hashimi, H. M., Kay, L. E., and Prestegard, J. H. (2001) Structural and dynamic analysis of residual dipolar coupling data for proteins, *Journal of the American Chemical Society 123*, 1416-1424.
120. Losonczi, J. A., Andrec, M., Fischer, M. W. F., and Prestegard, J. H. (1999) Order matrix analysis of residual dipolar couplings using singular value decomposition, *Journal of Magnetic Resonance 138*, 334-342.
121. Ramirez, B. E., and Bax, A. (1998) Modulation of the alignment tensor of macromolecules dissolved in a dilute liquid crystalline medium, *Journal of the American Chemical Society 120*, 9106-9107.
122. Al-Hashimi, H. M., Valafar, H., Terrell, M., Zartler, E. R., Eidsness, M. K., and Prestegard, J. H. (2000) Variation of molecular alignment as a means of resolving orientational ambiguities in protein structures from dipolar couplings, *Journal of Magnetic Resonance 143*, 402-406.
123. Bondensgaard, K., Mollova, E. T., and Pardi, A. (2002) The global conformation of the hammerhead ribozyme determined using residual dipolar couplings, *Biochemistry 41*, 11532-11542.
124. Cavanagh, J., Fairbrother, W. J., Palmer, A. G. I., and Skelton, N. J. (1996) *Protein NMR Spectroscopy*, Academic Press, San Diego, CA.

125. Jarymowycz, V. A., and Stone, M. J. (2006) Fast time scale dynamics of protein backbones: NMR relaxation methods, applications, and functional consequences, *Chemical Reviews 106*, 1624-1671.
126. Lipari, G., and Szabo, A. (1982) Model-free approach to the interpretation of nuclear magnetic resonance relaxation in macromolecules. 2. Analysis of experimental results, *Journal of the American Chemical Society 104*, 4559-4570.
127. Lipari, G., and Szabo, A. (1982) Model-Free Approach to the Interpretation of Nuclear Magnetic Resonance Relaxation in Macromolecules. 1. Theory and Range of Validity, *Journal of the American Chemical Society 104*, 4546-4559.
128. Zhang, Q., Sun, X., Watt, E. D., and Al-Hashimi, H. M. (2006) Resolving the motional modes that code for RNA adaptation, *Science 311*, 653-656.
129. Hansen, A. L., and Al-Hashimi, H.M. (2007) Dynamics of Large Elongated RNA by NMR Carbon Relaxation, *Journal of the American Chemical Society 129*, 16072-16082.
130. Yip, G. N., and Zuiderweg, E. R. (2004) A phase cycle scheme that significantly suppresses offset-dependent artifacts in the R2-CPMG 15N relaxation experiment, *J Magn Reson 171*, 25-36.
131. Fiala, R., Munzarova, M.L., and Sklenar, V. (2004) Experiments for correlating quaternary carbons in RNA bases., *Journal of Biomolecular NMR 29*, 477-490.
132. Sorensen, M. B., Meissner, A., and Sorensen, O. W. (1997) Spin-state-selective coherence transfer via intermediate states of two-spin coherence in IS spin systems: Application to E.COSY-type measurement of J coupling constants., *Journal of Biomolecular NMR 10*, 181-186.
133. Bax, A., and Davis, D. G. (1985) Practical Aspects Of Two-Dimensional Transverse Noe Spectroscopy, *Journal of Magnetic Resonance 63*, 207-213.
134. Massi, F., Johnson, E., Wang, C. Y., Rance, M., and Palmer III, A. G. (2004) NMR R-1 rho rotating-frame relaxation with weak radio frequency fields., *Journal of the American Chemical Society 126*, 2247-2256.
135. Korzhnev, D. M., Skrynnikov, N. R., Millet, O., Torchia, D. A., and Kay, L. E. (2002) An NMR experiment for the accurate measurement of heteronuclear spin-lock relaxation rates. , *Journal of the American Chemical Society 124*, 10743-10753.
136. Gueron, M., and Leroy, J. L. (1995) Studies of base pair kinetics by NMR measurement of proton exchange, *Methods Enzymol 261*, 383-413.
137. Reiter, N. J., Blad, H., Abildgaard, F., and Butcher, S. E. (2004) Dynamics in the U6 RNA intramolecular stem-loop: a base flipping conformational change, *Biochemistry 43*, 13739-13747.
138. Boisbouvier, J., Brutscher, B., Pardi, A., Marion, D., and Simorre, J. P. (2000) NMR determination of sugar puckers in nucleic acids from CSA-dipolar cross-correlated relaxation, *J . Am. Chem. Soc 122*, 6779-6780.
139. Johnson, J. E., and Hoogstraten, C. G. (2008) Extensive backbone dynamics in the GCAA RNA tetraloop analyzed using 13C NMR spin relaxation and specific isotope labeling, *Journal of the American Chemical Society 130*, 16757-16769.

140. Shajani, Z., and Varani, G. (2005) 13C NMR relaxation studies of RNA base and ribose nuclei reveal a complex pattern of motions in the RNA binding site for human U1A protein, *Journal of Molecular Biology 349*, 699-715.
141. Blad, H., Reiter, N. J., Abildgaard, F., Markley, J. L., and Butcher, S. E. (2005) Dynamics and metal ion binding in the U6 RNA intramolecular stem-loop as analyzed by NMR, *Journal of Molecular Biology 353*, 540-555.
142. Oberstrass, F. C., Allain, F. H., and Ravindranathan, S. (2008) Changes in dynamics of SRE-RNA on binding to the VTS1p-SAM domain studied by 13C NMR relaxation, *Journal of the American Chemical Society 130*, 12007-12020.
143. Carver, J. P., and Richards, R. E. (1972) A general two-site solution for the chemical exchange produced dependence of T2 upon the Carr-Purcell pulse separation, *Journal of Magnetic Resonance 6*, 89-105.
144. Korzhnev, D. M., Kloiber, K., and Kay, L. E. (2004) Multiple-quantum relaxation dispersion NMR spectroscopy probing millisecond time-scale dynamics in proteins: theory and application, *Journal of the American Chemical Society 126*, 7320-7329.
145. Mulder, F. A. A., and Akke, M. (2003) Carbonyl 13C transverse relaxation measurements to sample protein backbone dynamics, *Magnetic Resonance in Chemistry 41*, 853-865.
146. Korzhnev, D. M., Tischenko, E. V., and Arseniev, A. S. (2000) Off-resonance effects in N-15 T-2 CPMG measurements., *Journal of Biomolecular NMR 17*, 231-237.
147. Zweckstetter, M., and Holak, T. A. (1998) An adiabatic multiple spin-echo pulse sequence: Removal of systematic errors due to pulse imperfections and off-resonance effects , *Journal of Magnetic Resonance 133*, 134-147.
148. Akke, M., Fiala, R., Jiang, F., Patel, D., and Palmer, A. G. (1997) Base dynamics in a UUCG tetraloop RNA hairpin characterized by N-15 spin relaxation: Correlations with structure and stability, *RNA 3*, 702-709.
149. Johnson, J. E., Julien, K. R., and Hoogstraten, C. G. (2006) Alternate-site isotopic labeling of ribonucleotides for NMR studies of ribose conformational dynamics in RNA, *Journal of Biomolecular NMR 35*, 261-274.
150. Korzhnev, D. M., Orekhov, V. Y., and Kay, L. E. (2005) Off-Resonance R1G NMR Studies of Exchange Dynamics in Proteins with Low Spin-Lock Fields: An Application to a Fyn SH3 Domain, *Journal of the American Chemical Society 127*, 713-721.
151. Miloushev, V. Z., and Palmer III, A. G. (2005) R1ρ relaxation for two-site chemical exchange: General approximations and some exact solutions, *Journal of Magnetic resonance 177*, 221-227.
152. Trott, O., and Palmer III, A. G. (2002) R1rho Relaxation outside of the Fast-Exchange Limit, *Journal of Magnetic Resonance 154*, 157-160.
153. Korzhnev, D. M., Orekhov, V. Y., and Kay, L. E. (2005) Off-resonance R(1rho) NMR studies of exchange dynamics in proteins with low spin-lock fields: an application to a Fyn SH3 domain, *Journal of the American Chemical Society 127*, 713-721.

154. Pelupessy, P., Chiarparin, E., and Bodenhausen, G. (1999) Excitation of selected proton signals in NMR of isotopically labeled macromolecules, *Journal of Magnetic Resonance 138*, 178-181.
155. Pelupessy, P., and Chiarparin, E. (2000) Hartmann-Hahn polarization transfer in liquids: An ideal tool for selective experiments., *Concepts In Magnetic Resonance 12*, 103-124.

Chapter 2

Probing HIV-1 TAR RNA global conformational dynamics induced by Na^+ and Mg^{2+} using NMR Residual Dipolar Couplings

2.1 Introduction

Many regulatory ribonucleic acids (RNAs) undergo large changes in conformation upon binding to proteins and small ligand molecules but the mechanism by which this occurs remains poorly understood (*1-4*). Numerous studies have examined the extent to which molecules induce new RNA conformations versus capture conformations that are dynamically accessible in the unbound state (*1, 5-11*). In contrast, fewer studies have examined the potential role of monovalent and divalent cations in conformational adaptation and target recognition (*12*).

The interaction between the transactivation response element (TAR) RNA (*13*) from the human immunodeficiency type I virus (HIV-1) and the viral transactivator protein (Tat) is a paradigm for understanding the rules of RNA adaptive recognition (*1, 5, 8, 14*) and a primary target for developing anti-HIV therapeutics (*15-17*). Several high-resolution structures have been reported for HIV-I TAR (Figure 2.1), including the free form (*18*), bound to divalent cations (*19*), peptide mimics of Tat (*20, 21*), and six distinct

small molecules containing a different number of cationic groups designed to inhibit its interaction with Tat (*22-24*). These TAR conformations differ dramatically both in the global orientation of helices (inter-helical bend angle ranging between ~5° and ~47°) as well as the local conformation of bulge and neighboring residues where molecules bind. Thus, by adopting different conformations, TAR is capable of binding chemically diverse targets (Figure 2.1).

The molecular basis for TAR conformational adaptation is key for understanding its role in Tat-mediated transcription elongation of HIV-1 genes and for rationally designing inhibitors of its interaction with Tat (*16, 17*). Electrostatic interactions play important roles in both RNA folding and recognition (*25-30*) and thus can provide a basis for driving conformational changes accompanying complex formation. Previous studies have emphasized the importance of electrostatic interactions in TAR recognition. The spatial arrangements of basic groups in Tat relative to the negative TAR surface is an important determinant of Tat binding and its induced TAR conformational changes (*31*). The Tat bound TAR conformation (*20, 21*) can be stabilized by distinct small molecules that can satisfy two key electrostatic interactions (*24*). Aminoglycosides bind TAR with affinities that correlate with their total number of positive amines (*32*). Our NMR studies suggest that the changes in the TAR conformational dynamics induced by small molecules are also correlated to their total number of positive groups (*33*).

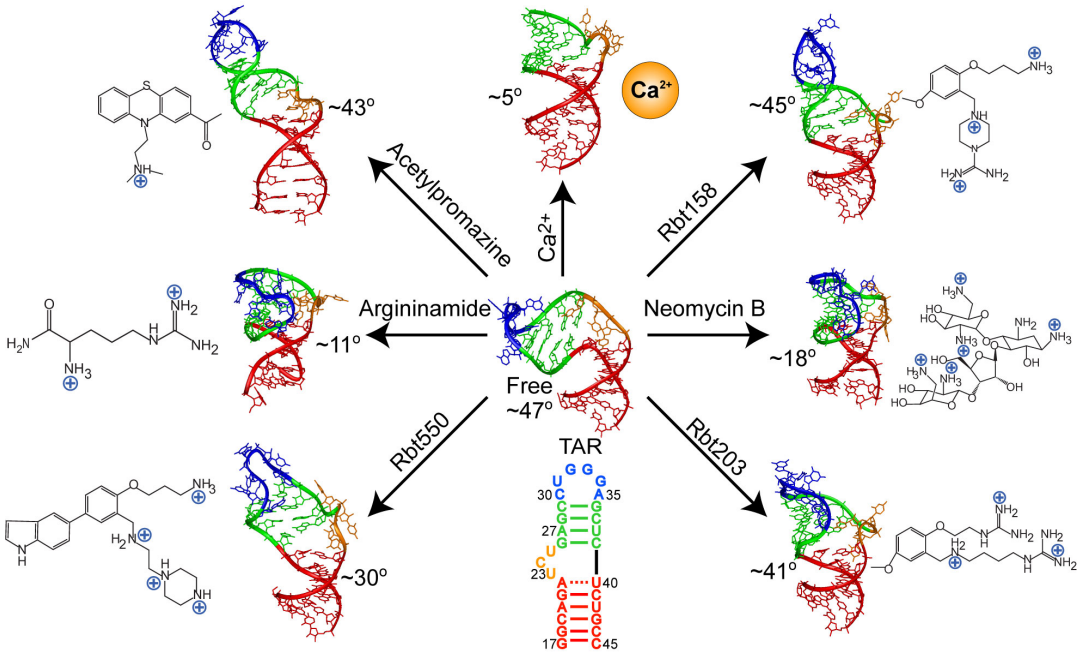

Figure 2.1: Conformation of HIV-1 TAR unbound and bound to distinct molecular targets. The inter-helical angles are indicated next to each conformation.

RNA electrostatic hot-spots, which would normally be stabilized by cationic groups on proteins and small molecules, are expected to be energetically unfavorable in the unbound RNA. One can therefore expect that these structural elements only become significantly stabilized during or following complex formation. However, metal cations can also stabilize such electrostatic hot-spots and thus pre-adapt the RNA conformation for target recognition. Several studies have shown that a variety of monovalent and divalent cations can associate with the TAR bulge (*19, 34-36*). Transient electric birefringence (*37*) and NMR (*38*) studies have shown that the addition of Mg^{2+} results in a significant reduction in the TAR inter-helical bend angle and dynamics (*19*). However, as is often the case, it remains unclear whether the Mg^{2+} induced transition is driven by non-specific electrostatic interactions with diffusive counterions, which could be recapitulated by cationic groups on small molecules, or by inner-sphere contacts with

specifically bound metals. Another unresolved question, which has also proven generally difficult to address, is whether the TAR conformations observed at various metal concentrations represent distinct conformations or a dynamical average of two or more states.

A number of studies suggest that the metal-induced TAR structural transition is driven by specific inner sphere contacts. An X-ray structure of TAR shows four specifically bound Ca^{2+} ions that stabilize a unique UCU bulge conformation through several inner-sphere contacts with TAR ligands (*19*). Furthermore, transient electric birefringence studies have shown that Mg^{2+} induced transitions in bulge containing RNAs are not recapitulated by Na^{+} even when using up to 50-fold higher concentrations (*37*). On the other hand, EPR studies show that Na^{+} and Ca^{2+} induce similar TAR conformational changes but that other metals can induce distinct effects (*34*).

Metal induced RNA conformational transitions have been studied using a variety of experimental biophysical techniques including EPR (*34*), fluorescence spectroscopy (*39*), hydroxyl radical footprinting (*40*), analytical ultracentrifugation (*41*), small angle x-ray scattering (*42*), and small angle neutron scattering (*43*). Although it can uniquely provide information about both structure and dynamics at site-specific resolution, few studies have employed NMR to structurally characterize metal-induced RNA transitions. This is in part because conventional NOE derived distance restraints can be insensitive to global conformational changes (*44*) and because high-resolution structure determination remains time consuming which makes characterizing structures at multiple metal concentrations impractical (*45, 46*).

In this study, we exploit the exquisite conformational sensitivity of NMR residual dipolar couplings (RDCs) (*47-50*) to characterize how the structure and dynamics of TAR change as a function of increasing Na^+ concentration and compare findings with changes induced by Mg^{2+} and small molecules. Aiding our study is an order tensor based analysis of RDCs, which permits studies of global conformational dynamics with high efficiency (*14, 45, 46, 51, 52*). The RDCs allowed us to detect Na^+ induced changes in the TAR conformation which are indistinguishable from those induced by Mg^{2+} even though chemical shift mapping data suggest that the two metals may bind TAR using distinct modes. These results together with electrostatic calculations offer new insights into the possible role of electrostatic interactions and counterion condensation in TAR adaptive recognition.

2.2 Materials and methods

2.2.1 NMR sample preparation

Samples of uniformly $^{13}C/^{15}N$ labeled TAR were prepared by *in vitro* transcription using synthetic double stranded DNA templates containing the T7 promoter and sequence of interest (Integrated DNA Technologies, Inc.), T7 RNA polymerase (Takara Mirus Bio, Inc.), and $^{13}C/^{15}N$ labeled nucleotide triphosphates (ISOTEC, Inc.). The RNA was purified by 20% (w/v) denaturing polyacrylamide gel electrophoresis containing 8M Urea and 1X TBE followed by electroelution in 20 mM Tris pH 8 buffer and ethanol precipitation. The RNA pellet was dissolved and exchanged into NMR buffer (15 mM sodium phosphate, 0.1 mM EDTA, and 25 mM NaCl at pH ~6.4,) using a centricon ultracel YM-3 concentrator (Millipore Corp.). The final RNA concentrations in

the aligned NMR samples were 0.3/0.5 mM for Na^+/Mg^{2+} respectively. The aligned samples were prepared by adding Pf1 phage (50 mg/ml) (*53, 54*) in NMR buffer to a pre-concentrated TAR RNA sample to yield a final Pf1 phage concentration of 17-20 mg/ml. The addition of phage did not affect the 'effective' Na^+ or Mg^{2+} concentration as judged from careful comparison of the chemical shifts in the absence and presence of phage (see Figure A4.1).

2.2.2 NMR Spectroscopy Measurements

All NMR experiments were performed at 298 K on an Avance Bruker 600 MHz spectrometer equipped with a triple-resonance cryogenic (5mm) probe with the exception of the 320 mM Na^+ RDCs which were measured on a Varian Inova 800 MHz spectrometer equipped with a triple resonance Z-gradient probe. NMR spectra were analyzed using NMR Draw (*55*) or Felix (Accelrys Inc, 2002) and overlaid using Sparky 3 (*56*).

Chemical shift titrations were performed on HIV-1 TAR RNA by recording 2D ^{13}C-^{1}H HSQC spectra following incremental additions in [Na^+] (25, 40, 80, 160 and 320mM against 0.2 mM TAR) or [Mg^{2+}] (0, 0.2, 0.4, 0.8, 1.6, 3.2 and 6.4 mM against 0.2mM TAR).

RDC measurements were collected on three separate samples of HIV-1 TAR in the presence of 160 mM Na^+, 320 mM Na^+ and 25 mM Na^+/4 mM Mg^{2+} respectively. One bond $^{1}D_{C6H6}$, $^{1}D_{C8H8}$, $^{1}D_{C5H5}$, $^{1}D_{C2H2}$, $^{1}D_{C1'H1'}$, and $^{1}D_{N1/3H1/3}$ RDCs were measured using 2D ^{13}C–^{1}H (or ^{15}N-^{1}H) S^3E HSQC experiments (*33, 57*) from the difference in splitting measured along the ^{13}C (or ^{15}N) dimension observed in the presence and absence

of Pf1 phage (*53, 54*). The same experiments and conditions were used to measure all the Na^+ and Mg^{2+} RDCs. The measurements of TAR in the presence of Mg^{2+} (0.5 mM RNA and 25 mM Na^+ /4 mM Mg^{2+}) were consistent with previously reported values (*38*). The measurement error was estimated from duplicate measurements using experiments that yield splittings along the ^1H and $^{13}C/^{15}N$ dimension (standard deviation between two RDC sets was 0.9 Hz, Figure A4.2). The RDCs of HIV-1 TAR in 25mM NaCl used in this study has been previously reported by Al-Hashimi *et. al* (*14*). The measured RDCs are listed in Table 2.1.

Table 2.1: HIV-1 TAR one bond $^1D_{C\text{-}H}$ and $^1D_{N\text{-}H}$ (in Hz) measured under different metal conditions.

Residue (bond vector)	160mM NaCl	320mM NaCl	25mM NaCl/4mM $MgCl_2$
17(C8H8)	-4.5	0.2	0.2
18(C1'H1')	*NA*	-29.5	*NA*
18(C8H8)	0.3	-1.6	-1.8
18(N1H1)	-7.3	*NA*	-2.8
19(C6H6)	9.6	10	8.4
20(C1'H1')	-6.6	-19.5	-26.4
20(C8H8)	12.2	16.4	13.6
20(C2H2)	7.9	4.4	6.1
21(C1'H1')	-6.6	-13	-19.9
21(C8H8)	15.6	20.8	18.6
21(N1H1)	-6.2	*NA*	-8.5
22(C8H8)	11.7	17.2	16.4
22(C2H2)	4.9	13.6	17.9
40(C1'H1')	-5.7	-8.7	*NA*
40(C5H5)	14.2	14.7	11.6
41(C6H6)	11.8	15.2	12.6
41(C5H5)	11.1	11.2	13.8
42(N3H3)	-5.6	*NA*	-7.8
43(C1'H1')	14.6	7.4	*NA*
43(C8H8)	13	15.5	11.9
43(N1H1)	-4.3	*NA*	-2.7
44(C6H6)	1.3	1.2	*NA*
44(C5H5)	12	17.2	*NA*
45(C1'H1')	2.9	-1.1	-16.9
45(C6H6)	-5	-4.3	-6.9
45(C5H5)	9.9	11.3	*NA*
23(C1'H1')	3.4	3.3	0.6
23(C6H6)	8.4	8.3	5.3
23(C5H5)	-0.5	0.2	0.5
24(C5H5)	1.1	-1.5	-1.7
25(C5H5)	4.7	4.5	2.3
26(C1'H1')	-16.4	-17.8	5.7
26(C8H8)	16.9	17.9	17.3

26(N1H1)	-4	*NA*	-8
27(C1'H1')	-14.5	-13.6	-12
27(C8H8)	14.6	14.8	12.4
27(C2H2)	16.9	13.7	16.3
28(C1'H1')	-8.9	-12.8	-11.5
28(C8H8)	16.5	18.3	14.6
28(N1H1)	*NA*	*NA*	-8.4
29(C6H6)	20.9	22.4	18.1
29(C5H5)	8.3	7.1	12.8
31(C1'H1')	-1.8	-8.4	-8.3
31(C6H6)	18.1	19.9	15.6
31(C5H5)	16.6	19.1	15
32(C1'H1')	8.1	13.1	11.7
32(C6H6)	9.4	10	10.1
32(C5H5)	6.4	12.4	10.3
33(C1'H1')	-10.5	-12.4	-10.3
33(C6H6)	4.2	6.4	6.8
33(C5H5)	0.6	0.8	0.8
34(C1'H1')	6.6	9.9	9.9
34(C8H8)	10	14.9	14.4
34(N1H1)	-5.6	*NA*	-9.3
36(C8H8)	22.9	25.3	22.5
36(N1H1)	-10.1	*NA*	-8.9
37(C5H5)	20.6	22.1	15.4
38(C1'H1')	*NA*	*NA*	-8.6
38(C6H6)	*NA*	16.8	15.6
38(C5H5)	19.9	25.2	19.9
38(N3H3)	-6.5	*NA*	-6.5
39(C5H5)	19.6	23.6	16.4

2.2.3 Data analysis

The thermodynamic equilibrium for an RNA-ligand reaction can be characterized by the dissociation constant (K_d). For the simple case where there is a single ligand-binding site in the RNA (1:1 complex), the K_d can be express as follows:

$$\text{RNA} + \text{Ligand} \rightleftharpoons \text{RNA-Ligand}$$

$$K_d = \frac{[RNA][Ligand]}{[RNA - Ligand]} \tag{2.1}$$

where the [RNA], [Ligand] and [RNA-Ligand] are the equilibrium concentrations of all the three species present in the reaction. A K_d value in the mM range implies that a ratio of ~1:1000 free and bound states is present in an equimolar mixture of RNA and ligand.

Conversely, a K_d in the μM range implies that a ratio of ~1:10,000 for these states are present forming a more stable RNA-Ligand complex than free species. To measure the dissociation constant we have to measure the free and bound species involved in the reaction. Thus the solution composition can be further defined as $[RNA]_{total} = [RNA]_{free} + [RNA]_{bound}$ and $[Ligand]_{total} = [RNA]_{free} + [RNA]_{bound}$. Experimentally, K_d measurements can be obtained by following NMR observables such as chemical shifts for a particular species involved in the RNA-Ligand reaction. These observables together with the known $[RNA]_{total}$ and $[Ligand]_{total}$ can be use to calculate the K_d.

Apparent dissociation constants were obtained by fitting the observed changes in chemical shift to the equation (*58*):

$$\delta_{obs} = \delta_{Free} + \frac{(\Delta\delta_T)\{([M]_T + [RNA]_T + K_d) - \sqrt{([M]_T + [RNA]_T + K_d)^2 + (4[M]_T[RNA]_T)}\}}{2[RNA]_T} \quad (2.2)$$

where $[M]_T$ is the total concentration of metal (Na^+ or Mg^{2+}), $[RNA]_T$ is the HIV-1 TAR concentration based on UV absorbance at 260 nm, $\Delta\delta_T$ is the difference in chemical shifts between the "free" and "metal associated" states (in ppm), δ_{obs} is the observed chemical shift (in ppm), and δ_{Free} is the chemical shift in the "free" state (in ppm). The data was fitted using the Origin software (OriginLab Corporation) in which $\Delta\delta_T$ and K_d (and δ_{Free} for Na^+) were allowed to vary during the fit. The K_d errors obtained from the fit were in excellent agreement with values obtained independently using a Monte Carlo approach. For the latter; "residuals" corresponding to the difference between the measured and best-fitted chemical shifts in the titration curves were computed for all the fitted data. The resulting distribution of residuals was fitted to a Gaussian distribution.

Next, simulations were performed in which perfect chemical shift titration data points corresponding to experimental values were generated and each point perturbed by a value randomly chosen from the Gaussian distribution. The perturbed points were then fitted to Equation 1 and the calculations repeated a hundred times. The difference between the "true" K_ds used in the simulation and values obtained from the curve fitting were then fitted to a Gaussian distribution and the resulting standard deviation assumed to be the K_d error. The fits that yielded chemical shift values that are outside the known chemical shift ranges for various nuclei were omitted from the analysis.

The RDCs measured in the TAR helices were subjected to an order tensor analysis using idealized A-form helices as input coordinates (*14*) as implemented in the program AFORM-RDC (*52*). The helices were constructed using the Biopolymer module in Insight II (Molecular Simulations, Inc.) followed by correction of propeller twist angles from +15º to -15º (*59*). The measured RDCs were fitted to idealized A-form helices using singular value decomposition (*60*) implemented in the in-house written program RAMAH (*61*). RDCs from terminal residues (17, 45, 22 and 40), bulge residues (23-25), and hairpin loop residues (31-34) were excluded from the analysis. The order tensor errors due to parameterized "A-form structural noise" and RDC uncertainty were estimated using the program AFORM-RDC (*52*). For each metal condition, helices were rotated into the principal axis system (PAS) of their best-fitted order tensor and assembled using the program Insight II (Molecular Simulations, Inc) by linking U40 (P) to C39 (O3') (~1.59 Å). Due to the order tensor degeneracy (*62*), this yielded four possible inter-helical orientations, three of which could be discarded; two because they lead to anti-parallel helix alignments and one because it resulted in a distance between

A22 (O3') and G26 (P) (>30 Å) that cannot be satisfactorily linked using the trinucleotide bulge. Inter-helical angles for all TAR structures were calculated using an in-house program.

Key statistics for the order tensor analysis of TAR under different metal conditions are on Table 2.2. For each helical stem of TAR, this table shows the number of RDCs (N), the condition number (CN) describing the orientational spread of the RDC targeted bond vectors (*63*), the root-mean-square deviation (RMSD), the correlation coefficient (*R*) between measured and back-predicted RDCs, the order tensor asymmetry ($\eta = |S_{yy} - S_{xx}|/S_{zz}$) and generalized degree of order (ϑ). The internal generalized degree of order (ϑ_{int}), inter-helical bend (θ) and twist (ξ) angles values for TAR at different metal conditions are also listed in this table (Table 2.2). Errors are estimated using the program AFORM-RDC (*52*)

Table 2.2: Order tensor analysis of HIV-1 TAR RDCs measured under different metal conditions.

Metal Condition	Stem	N	*CN*	RMSD (Hz)	*R*	η	ϑ x 10^{-3}	ϑ_{int}	θ (º)	ξ (º)
25 mM	I	13	2.9	1.1	0.99	0.27±0.04	0.48±0.04	0.56±0.05	46±4	61±50
NaCl	II	11	3.1	1.1	0.99	0.11±0.07	0.88±0.04			
160 mM	I	15	2.9	1.3	0.99	0.15±0.03	0.57±0.03	0.67±0.05	37±7	-1±50
NaCl	II	14	4.2	1.2	0.99	0.15±0.04	0.85±0.04			
320 mM	I	12	2.8	1.5	0.98	0.23±0.04	0.67±0.04	0.74±0.08	22±7	-18±50
NaCl	II	12	4.0	1.1	0.99	0.20±0.04	0.90±0.08			
4 mM	I	13	2.9	1	0.99	0.26±0.04	0.80±0.03	0.85±0.04	17±7	-58±50
$MgCl_2$	II	14	4.1	1	0.99	0.17±0.08	0.94±0.03			

Table 1: Shown for each helical stem are the number of RDCs (*N*), the condition number (*CN*) *(63)* describing the orientational spread of the RDC targeted bond vectors, the root-mean-square deviation (RMSD) and correlation coefficient (*R*) between measured and back-predicted RDCs, the order tensor asymmetry ($\eta = |S_{yy}-S_{xx}|/S_{zz}$), generalized degree of order (ϑ), internal generalized degree of order (ϑ_{int}), inter-helical bend (θ) and twist (ξ) angles. Errors are estimated using the in-house program AFORM-RDC

2.2.4 Electrostatic calculations

HIV-1 TAR RNA structures in free form (PDB ID#1ANR) and bound to argininamide (PDB ID#1ARJ), Ca^{2+} (PDB ID#397D), acetylpromazine (PDB ID#1LVJ), neomycin B (PDB ID#1QD3), Rbt158 (PDB ID#1UUI), Rbt203 (PDB ID#1UUD) and Rbt550 (PDB ID#UTS1) were obtained from the Protein Data Bank and used in the analysis. The electrostatic calculations were performed by solving the non-linear Poisson Boltzmann equation using the Delphi (*64*) module of Insight II (Molecular Simulations, Inc). No bound waters, ions or ligands were included in the calculation. The DNA-RNA AMBER force field (*65*) was used for the partial charges of atoms. An interior dielectric constant of 2 was used for the RNA molecule. The continuum dielectric constant for the solvent (water) was set to 80 with a 1:1 electrolyte distribution according to the Boltzmann weighted average of the mean potential. A 2.0 Å exclusion radius was added to the surface of the RNA to account for ion size and a 1.4 Å probe used to determine the RNA molecular surface. A monovalent salt concentration of 0.025 M was used in the calculations to mimic the low ionic strength NMR conditions. 3D structures were mapped onto a grid (65 x 65 x 65 grid points/side) and the boundary potential at each lattice calculated using the Debye-Huckel and full Columbic equations implemented in Delphi (*64*). The calculated electrostatic potential maps were displayed using the program GRASP provided by the Honig lab (*66*). Figures 2.5D and 2.6D show the calculated electrostatic surfaces for the unbound and bound (following removal of the ligands) TAR structures for all the models of the NMR ensemble.

2.3 Results

2.3.1 Chemical shift mapping of Na^+ and Mg^{2+} association with TAR RNA

As shown in Figure 2.2A, large and specific changes in chemical shift were observed in 2D HSQC spectra of TAR (0.3 mM) upon incrementally increasing the NaCl concentration from 25 mM to 320 mM in a background buffer containing 15 mM sodium phosphate and 0.1 mM EDTA at pH ~6.4. The largest chemical shift changes were observed in and around the bulge. In contrast, little to no changes were observed for residues in the UUCG loop. For the majority of resonances, the directions of the chemical shift perturbations were similar to those induced by Mg^{2+} although the magnitude of the latter was uniformly larger (Figure 2.2A). This can be attributed to tighter association of Mg^{2+} with TAR. As shown in Figure 2.2B, fitting of the chemical shift titration data to a two-state model yields apparent K_ds that are more than two orders of magnitude smaller for Mg^{2+} (K_d ~0.074 ± 0.002 – 0.10 ± 0.01 mM) compared to Na^+ (K_d ~0.11 ± 0.01 -0.28 ± 0.09 M), as has been reported for other RNAs. No further changes in the TAR chemical shifts were apparent beyond 6.4 mM Mg^{2+}, which is consistent with saturation kinetics and specific metal-induced transition. In the case of Na^+, chemical shift data could not be recorded near saturation point since this would require salt concentrations (~1 M) outside the tuning capacity of our probe.

Despite many similarities, subtle but detectable differences between the Mg^{2+} and Na^+ chemical shift perturbations were observed for residues G26, U23, and A27 (highlighted with a box, Figure 2.2A). Significantly, these are precisely the residues that are involved in inner sphere contacts with Ca^{2+} cations in the X-ray structure of TAR

(*19*). Thus, Na^+ and Mg^{2+} either stabilize a different conformation for these residues and/or associate with them in a different manner.

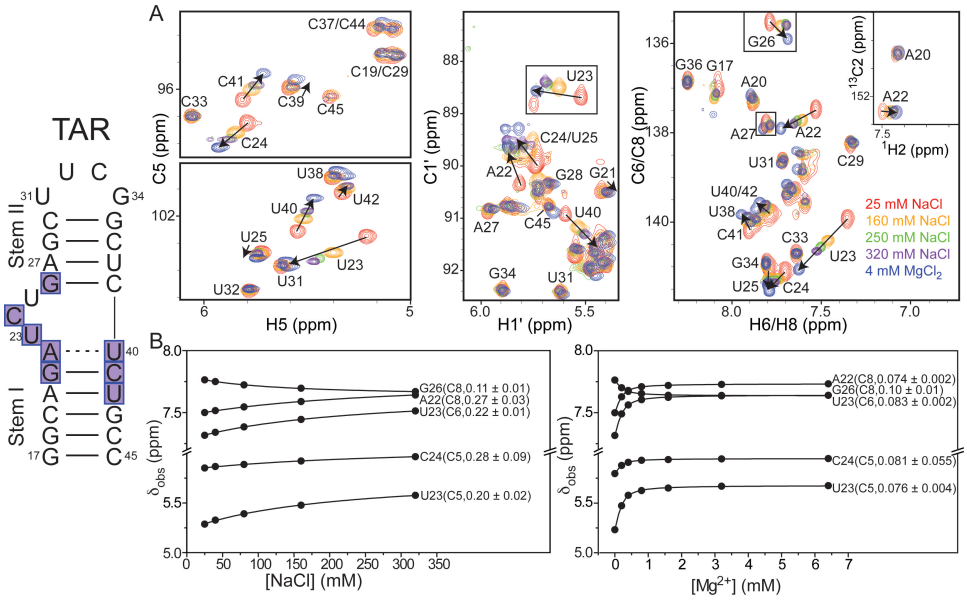

Figure 2.2: Chemical shift mapping of Na^+ and Mg^{2+} association with TAR RNA. On the left panel is the secondary structure of HIV-1 TAR RNA. The wild type loop was replaced here with a UUCG loop. (A) 2D HSQC spectra of TAR in the presence of Na^+ (25, 160, and 320 mM) and Mg^{2+} (25 mM Na^+/4 mM Mg^{2+}). The residues undergoing in the largest chemical shift perturbations (top 20% for a given type of resonance) upon Na^+ and Mg^{2+} are highlighted in blue and purple square boxes, respectively, on the TAR secondary structure. (B) Representative Na^+ and Mg^{2+} titration curves with K_d values (in M for Na^+ and in mM Mg^{2+}) shown at the end of the curve.

2.3.2 Structure and dynamics of TAR as a function of Na^+ and Mg^{2+} using RDCs

The interpretation of chemical shift perturbations is complicated by the fact that they are sensitive to changes in structure, dynamics, and metal localization. To specifically characterize the metal induced TAR conformational changes, we measured RDCs in TAR (0.3 mM) at Na^+ concentration of 25 mM, 160 mM, and 320 mM. Based on the apparent K_ds (Figure 2.2B), these correspond to 10%, 43%, and 60% of TAR being in the Na^+ "bound" state. For comparison, RDCs in the presence of 25 mM Na^+ /4 mM Mg^{2+} (83% of TAR bound) were measured using the same NMR experiments and

sample conditions used to measure the Na^+ RDCs. The Mg^{2+} RDCs were measured slightly below saturation, allowing insight into the dynamical nature of the metal-induced TAR transition under physiological Mg^{2+} concentrations. The Mg^{2+} RDCs were in very good agreement with values reported previously at slightly different Mg^{2+} concentrations (*38*).

As shown in Figure 2.3A, continuous and significant changes in RDCs (normalized for differences in total degree of order, see Figure legend) were observed upon increasing the Na^+ concentration, providing strong evidence for Na^+ induced changes in the TAR conformation. The 320 mM Na^+ RDCs are in better agreement with those measured at 25 mM Na^+ in the presence rather than in the absence of 4 mM Mg^{2+} (Figure 2.3A), indicating that Na^+ and Mg^{2+} induce similar TAR conformational changes.

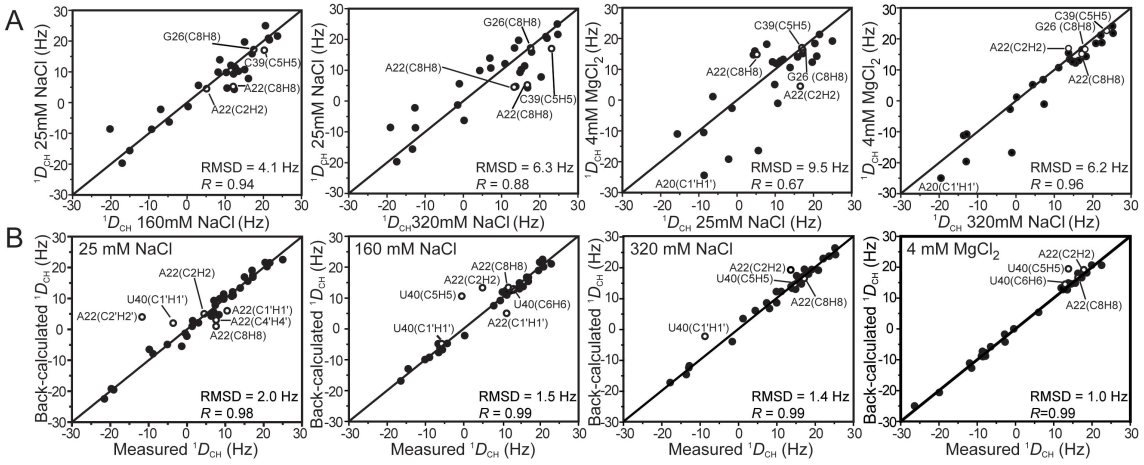

Figure 2.3: HIV-1 TAR RDCs as a function of Na^+ and Mg^{2+}. (A) Comparison of RDCs measured at 25, 160 and 320 mM Na^+ and Mg^{2+} (25 mM Na^+/4 mM Mg^{2+}). The RDCs were normalized (relative to 25 mM Na^+) to account for differences in the degree of order. This was done by scaling the RDCs measured under salt condition "X" by the ratio of stem II degree of order measured at X and 25 mM (i.e., through multiplication by $\vartheta_{Na\text{-}25mM}/\vartheta_X$). Stem II was used because it dominated the total degree of alignment in all cases. (B) Order tensor fits against an idealized A-form geometry carried out independently for stems I and II using RDCs measured at 25, 160, and 320 mM Na^+ and Mg^{2+} (25 mM Na^+/4 mM Mg^{2+}). Shown in each case is the root-mean-square deviation (RMSD) between the measured and back-predicted RDCs as well as the correlation coefficient (*R*).

To further characterize the metal induced transition, the RDCs were subjected to an order tensor analysis (*60, 63, 67*). Here, non-terminal Watson-Crick (WC) base pairs in individual helical stems were modeled assuming an idealized A-form geometry (*45, 51, 52*). The RDCs and idealized A-form geometry were then used to determine order tensors for each helical stem (statistics summarized in Table 2.2). As shown in Figure 2.3B, an excellent order tensor fit was obtained for RDCs measured under all metal conditions examined. In all cases, the root-mean-square-deviation (RMSD) between measured and back-predicted RDCs compared favorably with the RDC measurement uncertainty (0.9 Hz SD from comparison of ^{1}H and ^{13}C dimension RDCs, see Figure A4.2). Thus, the local conformation of the WC base pairs does not vary significantly from the ideal A-form geometry. The excellent RDC fits observed for residues G26 and A27 argue that the observed chemical shift differences with Na^{+} and Mg^{2+} (Figure 2.2A) are unlikely due to different metal-induced conformational changes at these sites but rather to differences in the modes of metal association with TAR. Likewise, both Na^{+} and Mg^{2+} yield slightly reduced values in the already attenuated bulge RDCs particularly for U23 (Figure A4.3). As mentioned previously (*19*), this is consistent with an increase in the local flexibility accompanying looped out bulge residues (*19*). The agreement for the flexible terminal A22-U40 base-pair RDCs (*14, 38*) (shown as open symbols, Figure 2.3B) that were not included in the order tensor fit, improves with increasing metal concentration (rmsd = 6.9 Hz, 5.1 Hz, and 3.4 Hz at 160 mM, 320 mM Na^{+} and 25 mM Na^{+} /4 mM Mg^{2+} respectively). This stabilization is consistent with the observed increase in coaxial stacking between the two stems with increasing metal concentration.

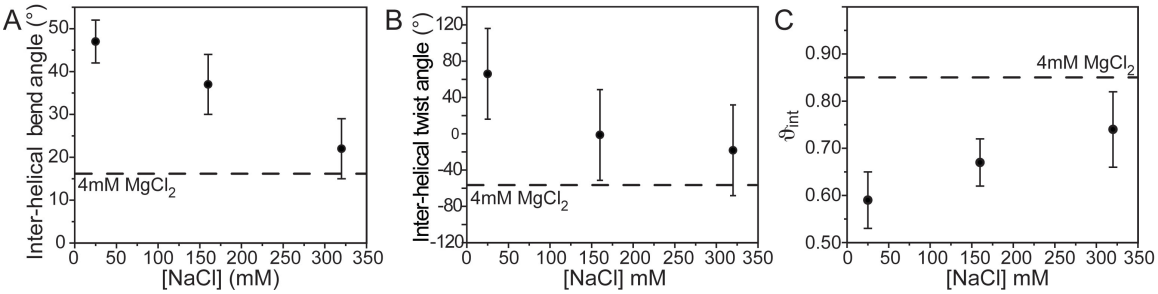

Figure 2.4: Probing the metal-induced TAR structure-dynamical transition using an order analysis of RDCs. Shown are (A) the inter-helical bend angle (θ), (B) inter-helical twist (ξ) (positive/negative values correspond to over/under twisting, respectively), and (C) inter-helical mobility (ϑ_{int}) as a function of Na^+ concentration. Values in the presence of 25 mM Na^+/4 mM Mg^{2+} are shown using a horizontal line.

Given the excellent fit to the A-form geometry, the observed changes in RDCs with increasing Na^+ concentration must be attributed to changes in the global orientation and/or dynamics of the two helices. To this end, we used the order tensors computed for each helix to determine their relative orientation and dynamics (*60, 67*) with estimated errors calculated using the program AFORM-RDC, which yields order tensor errors due to a combination of A-form structural noise and RDC uncertainty (*52*). In this analysis, the relative orientation of helices is obtained by superimposing their order tensor frames describing helix alignment relative to the applied magnetic field. The amplitude of inter-helical motions is computed from the ratio of the generalized degree of order ($\vartheta_{int} = \vartheta_i / \vartheta_j$; $\vartheta_i < \vartheta_j$) describing the degree of helix alignment relative to the applied magnetic field (*45, 63*). The ϑ_{int} value ranges between 1 for inter-helical rigidity and 0 for maximum inter-helical motions. Owing to possible correlations between helix motions and overall alignment, the ϑ_{int} value will generally underestimate the real motional amplitudes (*45, 68*).

As shown in Figure 2.4, increasing the Na^+ concentration from 25 to 320 mM led to a gradual reduction in the inter-helical bend from $\theta = 46° \pm 4°$ to $22° \pm 7°$ (Figure

2.4A). This was accompanied by a reduction in the inter-helical twist angle from $\xi = 66° \pm 50$ to $-18° \pm 50$ (Figure 2.4B) and amplitude of inter-helical motions from $\vartheta_{int} = 0.59 \pm 0.06$ to 0.74 ± 0.08 (Figure 2.4C). The comparatively large error in the inter-helical twist angle reflects the larger uncertainty in the principal $S_{xx} - S_{yy}$ directions arising due to near axial symmetry ($\eta \sim 0$) of the helix order tensors (Table 2.2). Similar but significantly larger conformational changes were induced by 25 mM Na^+ / 4 mM Mg^{2+} ($\theta = 17° \pm 7°$, $\xi = -58 \pm 50$, and $\vartheta_{int} = 0.85 \pm 0.04$, shown as horizontal lines in Figure 2.4). This suggests that the similar Na^+ and Mg^{2+} induced TAR chemical shift perturbations (Figure 2.2A) likely reflect a similar TAR conformational change that is driven by non-specific electrostatic interactions with counterions.

2.3.3 A two state non-specific electrostatic switch underlies the metal-induced TAR structure-dynamical transition

The TAR conformations observed at 25 mM, 160 mM and 320 mM Na^+ and 25 mM Na^+ /4 mM Mg^{2+} may either represent distinct conformations, or a population weighted average of two or more conformational states. Although these scenarios can be difficult to resolve (*43*), the latter can be tested for a simple two-state phenomenological model that is consistent with apparent good fit of chemical shift perturbations to a two state model (Figure 2.2B). Here, it is assumed that TAR consists of a population weighted average of two states; a metal "free" ensemble, characterized by inter-helical bend angle θ(free), and inter-helical flexibility ϑ_{int}(free), that is weakly associated with metals and which is favored at low ionic strength conditions (Figure 2.5A). The metal "bound" state, characterized by inter-helical bend angle θ(bound) and inter-helical

flexibility ϑ_{int}(bound), is more strongly associated with metals and within our metal concentration range is favored at high ionic strength conditions (Figure 2.5A). Assuming that the dynamical inter-conversion between the "free" and "bound" states occurs at timescales faster than the inverse of the measured RDCs (i.e. faster than milliseconds), the observed RDCs will be a population weighted average over the two states. Simulations using the TAR helices (data not shown) show that to a good approximation, the observed ϑ_{int} (ϑ_{int}(obs)) and inter-helical bend angle (θ(obs)) at a given Na^+ (or Mg^{2+}) will be given by a population weighted average of "free" and "bound" ensembles (*69, 70*):

$$\theta(obs) = (1-p_{bound}) \times \theta(free) + p_{bound} \times \theta(bound) \quad (2.3)$$

$$\vartheta_{int}(obs) = (1-p_{bound}) \times \vartheta_{int}(free) + p_{bound} \times \vartheta_{int}(bound) \quad (2.4)$$

where the values of p_{bound} can be computed from the apparent K_d values determined for Na^+ and Mg^{2+} based on the chemical shift titrations (Figure 2.2B). Assuming that Mg^{2+} stabilizes a similar bound structure as Na^+, which is supported by RDC measurements (Figure 2.3), the ϑ_{int}(obs) and θ(obs) measured under all four metal conditions (25 mM, 160 mM, and 320 mM Na^+ and 25 mM Na^+ /4 mM Mg^{2+}) can be fitted to Equation 2.3 to solve for the two unknowns in each case (ϑ_{int}(free), ϑ_{int}(bound) and θ(free), θ(bound) respectively). As shown in Figure 2.5, a good fit could be obtained for both the inter-helical bend angle θ(obs) (Figure 2.5B) and flexibility ϑ_{int}(obs) (Figure 2.5C). The average K_d values obtained for the largest chemical perturbations (described in section 2.2.3) were used in computing p_{bound} with minor differences observed when using various K_d values from the range observed (Figure 2.2B). No attempts were made to fit the inter-

helical twist angles given their much larger uncertainty. The fit yields parameters for the metal "bound" state (ϑ_{int}(bound) = 0.89 ± 0.02 and θ(bound) = 8° ± 4°) that is in very agreement with expectations based on the X-ray structure of TAR (θ(bound) = -11° and (ϑ_{int}(bound) = 1.0) which was determined in the presence of saturating amounts of divalent ions (100mM $CaCl_2$) (*19*).

Model conformations for the "free" and "bound" TAR states have been reported, namely an NOE-based NMR structure of unbound TAR under low ionic strength conditions in the absence of divalent ions (50 mM NaCl and 5 mM phosphate buffer) (*18*) and an X-ray structure of TAR determined in the presence of saturating Ca^{2+} concentrations (100 mM $CaCl_2$, 50 mM Na-cacodylate and 200 mM NH_4Cl) (*19*). To gain insight into the molecular basis for the metal-induced structural transition, we performed nonlinear Poisson-Boltzmann calculations (*30, 64*) and compared the surface electrostatic potential for these two TAR conformations.

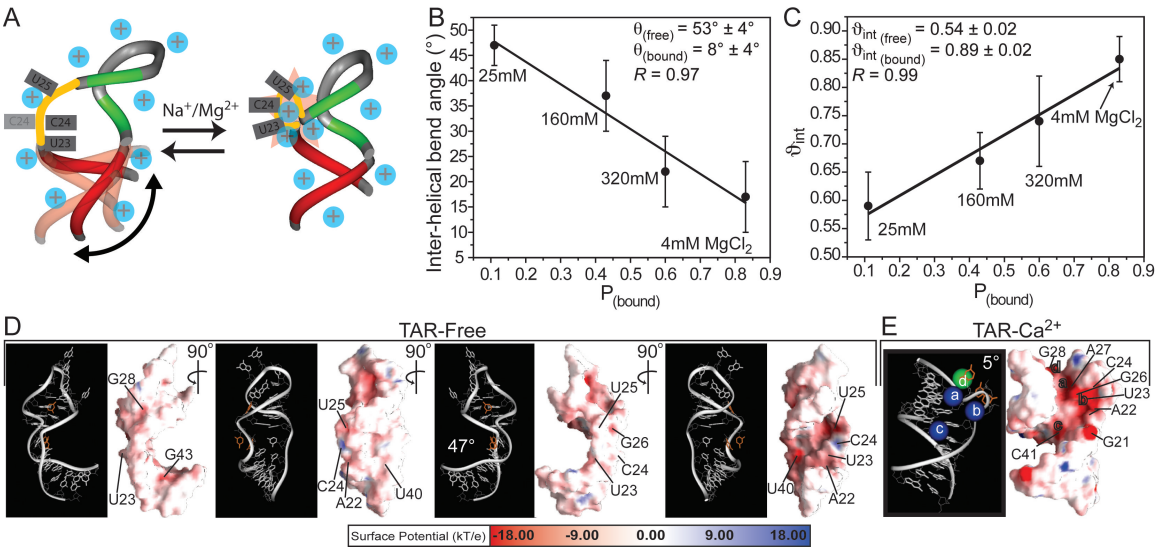

Figure 2.5: (A) Two-state model for the metal-induced TAR structural transition. (B-C) Fitting of the observed (B) inter-helical bend angle (θ(obs)) and (C) amplitude of inter-helical motions (ϑ_{int}(obs) as a function of the fractional bound populations (p_{bound}) using Equation 2.4. The "free" and "bound" θ and ϑ_{int} values obtained from the fit are shown together with the correlation coefficient (*R*). (D-E) Electrostatic surfaces for TAR (D) in "free" form (PDB ID #1ANR) *(18)* under moderate ionic strength conditions (50mM NaCl and 5mM phosphate buffer) with different views showing the weaker electrostatic potential and (E) bound to Ca^{2+} cations (PDB ID #397D) *(19)* with residues undergoing the largest metal-induced chemical shift perturbations highlighted

For unbound TAR, no significant electrostatic potential was observed (Figure 2.5D) for all models of the NMR ensemble. Rather, inter-helical bending allows the bulge to adopt an extended conformation that minimizes negative charge repulsion while allowing U23 to adopt a looped in stacked conformation (*18*) (Figure 2.5A). The looping in of this bulge residue accounts for the over-twisting observed at low ionic strength (positive ξ angles, Figure 2.4B) (*18*). In stark contrast, as shown in Figure 2.5E, a strong electrostatic potential was observed for the Ca^{2+} bound TAR structure in and around the bulge (G21-C24, and A27) precisely at residues that exhibit large metal-induced chemical shift perturbations (Figure 2.2A). This strong negative potential explains in part why coaxial TAR conformations are not favored at low ionic strength conditions despite the energetic benefits of helical stacking, metals are required to screen repulsive forces. The

metal bound TAR conformation is also likely disfavored by the looping out of U23 and loss of stacking interactions with A22 and U24 (Figure 2.5A).

2.3.4 Comparison with small molecule binding

We previously used RDCs to characterize the conformational dynamics of TAR bound to the small molecules argininamide (*71*), acetylpromazine, and neomycin B (*33*). We noted qualitatively that the small molecules induce a reduction in the TAR inter-helical bend angle and dynamics by an amount that is apparently dependent on their total number of positive groups. These trends are shown more quantitatively in Figure 2.6 using an expanded set of TAR structures. An inverse correlation is apparent between the TAR inter-helical bend angle (θ) (Figure 2.6A) and dynamics (ϑ_{int}) (Figure 2.6C) and the net positive charge delivered by the small molecule. This is analogous to the trend observed with increasing metal concentration (Figure 2.4). In contrast, no significant correlation is observed with the inter-helical twist (ξ) angle (Figure 2.6B), which as mentioned previously, is also influenced by the local bulge conformation. For the Tat mimic argininamide (ARG), a charge of both +2 and +6 is shown. The latter is based on surface plasmon resonance measurements indicating that up to three ARG molecules bind TAR under NMR conditions (*24*).

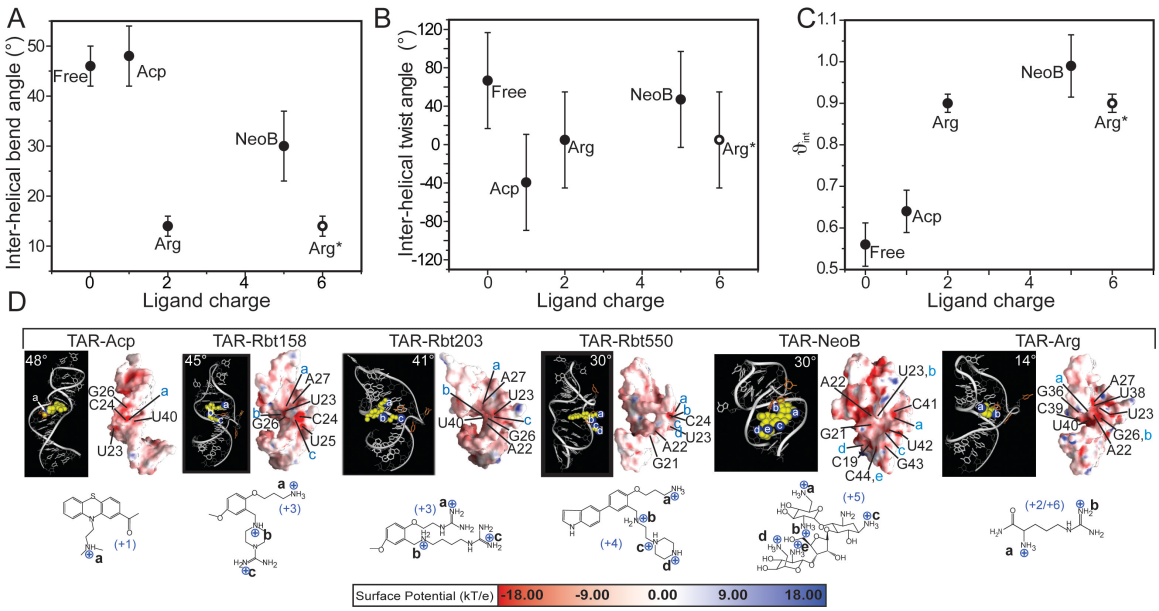

Figure 1.6: TAR conformational dynamics when bound to the small molecules argininamide (ARG), acetylpromazine (ACP), neomycin B (NeoB), Rbt 158, Rbt 203, and Rbt 550. Shown are the (A) inter-helical bend angle (θ), (B) inter-helical twist angle (ξ), and (C) amplitude of inter-helical motions (ϑ_{int}) as a function of total positive charge delivered by the small molecules. The inter-helical bend angles for ARG, ACP, and NeoB were obtained from order tensor analysis of RDCs, as reported previously *(33,71)*. For remaining structures, the angles were obtained from model 1 of the NOE-based NMR structure (Rbt 158, Rbt 203, and Rbt 550) *(24)* or the X-ray structure (Ca^{2+}) *(19)*. For ARG, which has a charge of +2, a total charge of +6 is also shown based on surface plasmon resonance measurements that indicate that up to three ARG molecules bind TAR *(24)*. For Ca^{2+}, a charge of +8 is assumed based on observation of 4 x Ca^{2+} ions in the X-ray structure *(19)*. (D) Electrostatic surfaces for the bound TAR structures following removal of ligands. Highlighted in blue letters are the positions of cationic groups on small molecules relative to the TAR electrostatic surface. The TAR orientation in each case was chosen to illustrate proximity of cationic groups near the strong negative TAR charge potential

The above results suggest that electrostatic interactions also dominate the TAR global conformational changes that are induced by small molecule recognition. To explore this further, we performed nonlinear Poisson-Boltzmann calculations on the TAR complexes following removal of bound ligands. Despite variations due to the structural uncertainty of the NMR ensemble, cationic groups from small molecules were frequently observed near TAR regions of strong electrostatic potential (Figure 2.6D), particularly for regions in and around the bulge, as previously noted for the Rbt family of ligands (*24*). Furthermore, as expected, linear TAR conformations (e.g. TAR-NeoB, TAR-Ca^{2+} and

TAR-ARG) generally have a stronger electrostatic potential compared to the more bent conformations (e.g. TAR-ACP) (Figure 2.6D). The electrostatic hot-spots in the linear conformations are primarily composed of backbone phosphates (O1P, O2P) which explains why for example Mg^{2+}, NeoB, and ARG are effective at stabilizing the TAR global backbone conformation. In contrast, for the highly bent conformations (TAR-ACP, TAR-Rbt158 and TAR-Rbt203), they are primarily composed of oxygen and nitrogen atoms in sugar (O2', O3', O5') and base (U(O4, O2), G(N7, O6), A(N7)) moieties. The lack of involvement of backbone phosphates helps rationalize why ACP is ineffective at stabilizing the TAR overall conformation. No dynamical data has been obtained for the Rbt family of small molecules.

2.3.5 Possible role for counterions in TAR adaptive recognition

In Figure 2.7, we show the inter-helical bend (θ) and twist angles (ξ) for TAR in different ligand bound states along with the conformational changes that are induced by metals ions. Many of the ligand bound TAR conformations fall along or near the predicted two-state metal induced conformational transition. This highlights the similar changes in the TAR conformation that are induced by small molecules and metals. The largest deviation from the pathway is observed for ACP, which among the bound TAR conformations has the weakest electrostatic potential composed of sugar and base moieties. Interestingly, at the extremity of our two state metal transition, we find the functionally relevant TAR conformation that is stabilized by the Tat mimic ARG (Figure 2.7). Thus, metals may act to increase the probability of sampling productive conformations that mimic the functional protein bound state by screening unfavorable backbone repulsive forces. By also reducing the population of non-productive

conformations, counterions may decrease the likelihood for non-specific adaptation and promiscuous recognition. In this context, metals may act to bias the specificity of internal motions towards functionally active conformations.

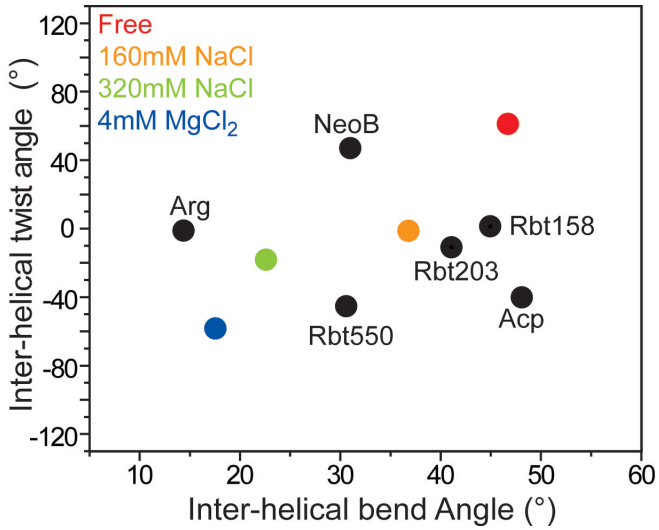

Figure 2.7: Comparison of metal and small molecule induced changes in the TAR inter-helical conformation

2.4 Conclusion

Our results show that Na^+ and Mg^{2+} ions induce a similar TAR structural and dynamical transition from a bent flexible to coaxial rigid state though the binding modes of the two metals may be different. This is in contrast to previous transient electric birefringence studies indicating that the Mg^{2+} induced transitions in model bulge containing RNAs are not reproduced by Na^+ even when using up to 50-fold higher concentrations (*72*). It remains to be established if the observed effects of monovalent ions on the TAR conformation are a general feature of bulge containing RNAs.

The similar structural and dynamical changes induced by Na^+ and Mg^{2+} strongly suggests that non-specific electrostatic interactions with diffusive counterions, and not

specifically bound metals observed in the X-ray structure, drive the TAR global structure-dynamical transition. Our results do not however rule out the presence of inner sphere contact(s) particularly with Mg^{2+}. Similar electrostatic interactions seem to dominate the TAR conformational transitions that are induced by Tat derived peptides and other small molecules. Many of these ligand bound TAR conformations fall near the pathway of the metal-induced conformational transition (Figure 2.7) suggesting that metals may be involved in adapting the TAR conformation for target recognition.

Finally, our study underscores the intricate sensitivity of RNA structural dynamics to environmental conditions. The range of ionic strength (25 mM – 320 mM) over which significant changes in the TAR structural and dynamical changes could be detected falls within a range of buffer conditions that are often used interchangeably. This emphasizes the need to consider differences in buffer conditions as a potential cause for any observed differences in RNA conformations and dynamics. Our results also demonstrate the ability to use RDCs in quantitatively measuring subtle differences in RNA conformational dynamics.

This work has been published in the journal of Biochemistry (*73*). The idea was conceived by Al-Hashimi, H. M. and Casiano-Negroni, A. The oligonucleotide TAR RNA was synthesized by Sun, X. The NMR data was recorded and analyzed by Casiano-Negroni, A.

2.5 References

1. Leulliot, N., and Varani, G. (2001) Current topics in RNA-protein recognition: Control of specificity and biological function through induced fit and conformational capture, *Biochemistry 40*, 7947-7956.
2. Micura, R., and Hobartner, C. (2003) On secondary structure rearrangements and equilibria of small RNAs, *Chembiochem 4*, 984-990.
3. Al-Hashimi, H. M. (2005) Dynamics-Based Amplification of RNA Function and Its Characterization by Using NMR Spectroscopy, *Chembiochem 6*, 1506-1519.
4. Storz, G. (2002) An expanding universe of noncoding RNAs, *Science 296*, 1260-1263.
5. Williamson, J. R. (2000) Induced fit in RNA-protein recognition, *Nature Structural Biology 7*, 834-837.
6. Kim, H. D., Nienhaus, G. U., Ha, T., Orr, J. W., Williamson, J. R., and Chu, S. (2002) Mg2+-dependent conformational change of RNA studied by fluorescence correlation and FRET on immobilized single molecules, *Proccedings of the National Academy of Sciences of the United States of America 99*, 4284-4289.
7. Mu, Y., and Stock, G. (2006) Conformational dynamics of RNA-peptide binding: a molecular dynamics simulation study, *Biophys J 90*, 391-399.
8. Zhang, Q., Sun, X., Watt, E. D., and Al-Hashimi, H. M. (2006) Resolving the motional modes that code for RNA adaptation, *Science 311*, 653-656.
9. Dayie, K. T., Brodsky, A. S., and Williamson, J. R. (2002) Base Flexibility in HIV-2 TAR RNA Mapped by Solution (15)N, (13)C NMR Relaxation, *J Mol Biol 317*, 263-278.
10. Pitici, F., Beveridge, D. L., and Baranger, A. M. (2002) Molecular dynamics simulation studies of induced fit and conformational capture in U1A-RNA binding: do molecular substates code for specificity? , *Biopolymers 65*, 424-435.
11. Noeske, J., Buck, J., Furtig, B., Nasiri, H. R., Schwalbe, H., and Wohnert, J. (2007) Interplay of 'induced fit' and preorganization in the ligand induced folding of the aptamer domain of the guanine binding riboswitch, *Nucleic Acids Research 35*, 572-583.
12. Hermann, T., and Westhof, E. (1999) Simulations of the dynamics at an RNA-protein interface, *Nat Struct Biol 6*, 540-544.
13. Muesing, M. A., Smith, D. H., and Capon, D. J. (1987) Regulation of mRNA accumilation by a human immunodeficiency virus trans-activator protein., *Cell 48*, 691-701.
14. Al-Hashimi, H. M., Gosser, Y., Gorin, A., Hu, W., Majumdar, A., and Patel, D. J. (2002) Concerted motions in HIV-1 TAR RNA may allow access to bound state conformations: RNA dynamics from NMR residual dipolar couplings, *J Mol Biol 315*, 95-102.
15. Bannwarth, S., and Gatignol, A. (2005) HIV-1 TAR RNA: the target of molecular interactions between the virus and its host, *Curr HIV Res 3*, 61-71.
16. Krebs, A., Ludwig, V., Boden, O., and Gobel, M. W. (2003) Targeting the HIV trans-activation responsive region--approaches towards RNA-binding drugs, *Chembiochem 4*, 972-978.

17. Froeyen, M., and Herdewijn, P. (2002) RNA as a target for drug design, the example of Tat-TAR interaction, *Curr Top Med Chem 2*, 1123-1145.
18. Aboul-ela, F., Karn, J., and Varani, G. (1996) Structure of HIV-1 TAR RNA in the absence of ligands reveals a novel conformation of the trinucleotide bulge, *Nucleic Acids Research 24*, 3974-3981.
19. Ippolito, J. A., and Steitz, T. A. (1998) A 1.3-angstrom resolution crystal structure of the HIV-1 trans- activation response region RNA stem reveals a metal ion-dependent bulge conformation, *Proceedings of the National Academy of Sciences of the United States of America 95*, 9819-9824.
20. Puglisi, J. D., Tan, R., Calnan, B. J., Frankel, A. D., and Williamson, J. R. (1992) Conformation of the TAR RNA-arginine complex by NMR spectroscopy, *Science 257*, 76-80.
21. Aboul-ela, F., Karn, J., and Varani, G. (1995) The Structure of the Human-Immunodeficiency-Virus Type-1 Tar RNA Reveals Principles of RNA Recognition By Tat Protein, *Journal of Molecular Biology 253*, 313-332.
22. Faber, C., Sticht, H., Schweimer, K., and Rosch, P. (2000) Structural rearrangements of HIV-1 Tat-responsive RNA upon binding of neomycin B, *J Biol Chem 275*, 20660-20666.
23. Du, Z., Lind, K. E., and James, T. L. (2002) Structure of TAR RNA complexed with a Tat-TAR interaction nanomolar inhibitor that was identified by computational screening, *Chem Biol 9*, 707-712.
24. Davis, B., Afshar, M., Varani, G., Murchie, A. I., Karn, J., Lentzen, G., Drysdale, M., Bower, J., Potter, A. J., Starkey, I. D., Swarbrick, T., and Aboul-ela, F. (2004) Rational design of inhibitors of HIV-1 TAR RNA through the stabilisation of electrostatic "hot spots", *J Mol Biol 336*, 343-356.
25. Law, M. J., Linde, M. E., Chambers, E. J., Oubridge, C., Katsamba, P. S., Nilsson, L., Haworth, I. S., and Laird-Offringa, I. A. (2006) The role of positively charged amino acids and electrostatic interactions in the complex of U1A protein and U1 hairpin II RNA, *Nucleic Acids Research 34*, 275-285.
26. Draper, D. E., Grilley, D., and Soto, A. M. (2005) Ions and RNA folding, *Annual Review of Biophysics And Biomolecular Structure 34*, 221-243.
27. Draper, D. E. (2004) A guide to ions and RNA structure, *RNA 10*, 335-343.
28. Woodson, S. A. (2005) Metal ions and RNA folding: a highly charged topic with a dynamic future, *Curr. Opin. Chem. Biol. 9*, 104-109.
29. Garcia-Garcia, C., and Draper, D. E. (2003) Electrostatic interactions in a peptide--RNA complex, *J Mol Biol 331*, 75-88.
30. Chin, K., Sharp, K. A., Honig, B., and Pyle, A. M. (1999) Calculating the electrostatic properties of RNA provides new insights into molecular interactions and function, *Nat Struct Biol 6*, 1055-1061.
31. Tao, J., and Frankel, A. D. (1993) Electrostatic interactions modulate the RNA-binding and transactivation specificities of the human immunodeficiency virus and simian immunodeficiency virus Tat proteins, *Proceedings National Academy of Science USA 90*, 1571-1575.
32. Blount, K. F., Tor, Y., Hamasaki, K., and Ueno, A. (2003) Using pyrene-labeled HIV-1 TAR to measure RNA-small molecule binding aminoglycoside antibiotics,

neamine and its derivatives as potent inhibitors for the RNA-protein interactions derived from HIV-1 activators, *Nucleic Acids Res 31*, 5490-5500.
33. Pitt, S. W., Zhang, Q., Patel, D. J., and Al-Hashimi, H. M. (2005) Evidence that electrostatic interactions dictate the ligand-induced arrest of RNA global flexibility, *Angew Chem Int Ed Engl 44*, 3412-3415.
34. Edwards, T. E., and Th Sigurdsson, S. (2002) Electron paramagnetic resonance dynamic signatures of TAR RNA-small molecule complexes provide insight into RNA structure and recognition, *Biochemistry 41*, 14843-14847.
35. Olejniczak, M., Gdaniec, Z., Fischer, A., Grabarkiewicz, T., Bielecki, L., and Adamiak, R. W. (2002) The bulge region of HIV-1 TAR RNA binds metal ions in solution, *Nucleic Acids Res 30*, 4241-4249.
36. Edwards, T. E., Okonogi, T. M., and Sigurdsson, S. T. (2002) Investigation of RNA-protein and RNA-metal ion interactions by electron paramagnetic resonance spectroscopy. The HIV TAR-Tat motif, *Chem Biol 9*, 699-706.
37. Zacharias, M., and Hagerman, P. J. (1995) The Bend in RNA Created By the Transactivation Response Element Bulge of Human-Immunodeficiency-Virus Is Straightened By Arginine and By Tat-Derived Peptide, *Proceedings of the National Academy of Sciences of the United States of America 92*, 6052-6056.
38. Al-Hashimi, H. M., Pitt, S. W., Majumdar, A., Xu, W., and Patel, D. J. (2003) Mg2+-induced variations in the conformation and dynamics of HIV-1 TAR RNA probed using NMR residual dipolar couplings, *J Mol Biol 329*, 867-873.
39. Bokinsky, G., and Zhuang, X. (2005) Single-molecule RNA folding, *Acc Chem Res 38*, 566-573.
40. Brenowitz, M., Chance, M. R., Dhavan, G., and Takamoto, K. (2002) Probing the structural dynamics of nucleic acids by quantitative time-resolved and equilibrium hydroxyl radical "footprinting", *Curr Opin Struct Biol 12*, 648-653.
41. Takamoto, K., He, Q., Morris, S., Chance, M. R., and Brenowitz, M. (2002) Monovalent cations mediate formation of native tertiary structure of the Tetrahymena thermophila ribozyme, *Nature Structural Biology 9*, 928-933.
42. Caliskan, G., Hyeon, C., Perez-Salas, U., Briber, R. M., Woodson, S. A., and Thirumalai, D. (2005) Persistence length changes dramatically as RNA folds, *Physical Review Letters 95*, 268303.
43. Perez-Salas, U., Rangan, P., FKrueger, S., Briand, R. M., Thirumalai, D., and Woodson, S. A. (2004) Compaction of a bacterial group I ribozyme coincides with the assembly of core helices, *Biochemistry 43*, 1746-1753.
44. Mollova, E. T., and Pardi, A. (2000) NMR solution structure determination of RNAs, *Current Opinion in Structural Biology 10*, 298-302.
45. Al-Hashimi, H. M., and Patel, D. J. (2002) Residual dipolar couplings: Synergy between NMR and structural genomics, *Journal of Biomolecular Nmr 22*, 1-8.
46. Al-Hashimi, H. M., Gorin, A., Majumdar, A., Gosser, Y., and Patel, D. J. (2002) Towards structural genomics of RNA: rapid NMR resonance assignment and simultaneous RNA tertiary structure determination using residual dipolar couplings, *J Mol Biol 318*, 637-649.
47. Prestegard, J. H., Al-Hashimi, H. M., and Tolman, J. R. (2000) NMR structures of biomolecules using field oriented media and residual dipolar couplings, *Quarterly Reviews of Biophysics 33*, 371-424.

48. Tjandra, N., and Bax, A. (1997) Direct measurement of distances and angles in biomolecules by NMR in a dilute liquid crystalline medium, *Science 278*, 1111-1114.
49. Tolman, J. R., Flanagan, J. M., Kennedy, M. A., and Prestegard, J. H. (1995) Nuclear Magnetic Dipole Interactions in Field-Oriented Proteins - Information For Structure Determination in Solution, *Proceedings of the National Academy of Sciences of the United States of America 92*, 9279-9283.
50. Bax, A., and Grishaev, A. (2005) Weak alignment NMR: a hawk-eyed view of biomolecular structure, *Current Opinion in Structural Biology 15*, 563-570.
51. Mollova, E. T., Hansen, M. R., and Pardi, A. (2000) Global structure of RNA determined with residual dipolar couplings, *Journal of the American Chemical Society 122*, 11561-11562.
52. Musselman, C., Pitt, S. W., Gulati, K., Foster, L., Andricioaei, I., and Al-Hashimi, H. M. (2006) Impact of static and dynamic A-form heterogeneity on the determination of RNA global structural dynamics using NMR residual dipolar couplings *Journal of Biomolecular NMR 36*, 235-249.
53. Hansen, M. R., Hanson, P., and Pardi, A. (2000) Filamentous bacteriophage for aligning RNA, DNA, and proteins for measurement of nuclear magnetic resonance dipolar coupling interactions, *Methods in Enzymology 317*, 220-240.
54. Clore, G. M., Starich, M. R., and Gronenborn, A. M. (1998) Measurement of residual dipolar couplings of macromolecules aligned in the nematic phase of a colloidal suspension of rod- shaped viruses, *Journal of the American Chemical Society 120*, 10571-10572.
55. Delaglio, F., Grzesiek, S., Vuister, G. W., Zhu, G., Pfeifer, J., and Bax, A. (1995) Nmrpipe - a Multidimensional Spectral Processing System Based On Unix Pipes, *Journal of Biomolecular Nmr 6*, 277-293.
56. Goddard, T. D. K., D.G. (2004) SPARKY 3, in *University of California, San Francisco*.
57. Meissner, A., and Sorensen, O. W. (1999) Suppression of diagonal peaks in TROSY-type H-1 NMR NOESY spectra of N-15-labeled proteins, *Journal of Magnetic Resonance 140*, 499-503.
58. Gonzales, R. L. J., and Tinoco, I. Jr. (1999) Solution structure and thermodynamics of a divalent metal ion binding site in an RNA pseudoknot., *Journal of Molecular Biology 289*, 1267-1282.
59. Neidle, S. (1999) *Oxford Handbook of Nucleic Acid Structure*, Oxford University Press, New York.
60. Losonczi, J. A., Andrec, M., Fischer, M. W. F., and Prestegard, J. H. (1999) Order matrix analysis of residual dipolar couplings using singular value decomposition, *Journal of Magnetic Resonance 138*, 334-342.
61. Hansen, A. L., and Al-Hashimi, H. M. (2006) Insight into the CSA tensors of nucleobase carbons in RNA polynucleotides from solution measurements of residual CSA: towards new long-range orientational constraints, *J Magn Reson 179*, 299-307.
62. Al-Hashimi, H. M., Valafar, H., Terrell, M., Zartler, E. R., Eidsness, M. K., and Prestegard, J. H. (2000) Variation of molecular alignment as a means of resolving

orientational ambiguities in protein structures from dipolar couplings, *Journal of Magnetic Resonance 143*, 402-406.
63. Tolman, J. R., Al-Hashimi, H. M., Kay, L. E., and Prestegard, J. H. (2001) Structural and dynamic analysis of residual dipolar coupling data for proteins, *Journal of the American Chemical Society 123*, 1416-1424.
64. Nicholls, A., Sharp, K. A., and Honig, B. (1991) Protein folding and association: insights from the interfacial and thermodynamic properties of hydrocarbons, *Proteins 11*, 281-296.
65. Cornell, W. D., Cieplak, P., Bayly, C. I., Gould, I. R., Merz, K. M., Ferguson, D. M., Spellmeyer, D. C., Fox, T., Caldwell, J. W., and Kollman, P. A. (1995) A 2nd Generation Force-Field For The Simulation Of Proteins, Nucleic-Acids, And Organic-Molecules, *Journal Of The American Chemical Society 117*, 5179-5197.
66. Nicholls, A., and Honing, B. (1991) A rapid difference algorith, utilizing successive over relaxation to solve the Poisson-Boltzmann equation., *J. Comp. Chem. 12*, 435-445.
67. Saupe, A. (1968) Recent results in the field of liquid crystals, *Angew. Chem., Int. Ed. Engl. 7*, 97-112.
68. Zhang, Q., Throolin, R., Pitt, S. W., Serganov, A., and Al-Hashimi, H. M. (2003) Probing motions between equivalent RNA domains using magnetic field induced residual dipolar couplings: accounting for correlations between motions and alignment, *J Am Chem Soc 125*, 10530-10531.
69. Al-Hashimi, H. M., and Gorin, A. (2003) Application of NMR residual dipolar couplings in studies of RNA: Towards high throughput investigations, *Applied Genom Proteomic 2*, 3-16.
70. Bolon, P. J., Al-Hashimi, H. M., and Prestegard, J. H. (1999) Residual dipolar coupling derived orientational constraints on ligand geometry in a 53 kDa protein-ligand complex, *Journal of Molecular Biology 293*, 107-115.
71. Pitt, S. W., Majumdar, A., Serganov, A., Patel, D. J., and Al-Hashimi, H. M. (2004) Argininamide binding arrests global motions in HIV-1 TAR RNA: comparison with Mg2+-induced conformational stabilization, *J Mol Biol 338*, 7-16.
72. Zacharias, M., and Hagerman, P. J. (1995) Bulge-induced bends in RNA: quantification by transient electric birefringence, *J Mol Biol 247*, 486-500.
73. Casiano-Negroni, A., Sun, X., and Al-Hashimi, H. M. (2007) Probing Na(+)-Induced Changes in the HIV-1 TAR Conformational Dynamics Using NMR Residual Dipolar Couplings: New Insights into the Role of Counterions and Electrostatic Interactions in Adaptive Recognition., *Biochemistry 46*, 6525-6535.

Chapter 3

Dynamics of A-site ribosomal RNA in the presence and absence of paromomycin

3.1 Introduction

A-site is a ribosomal RNA located in the small subunit of the ribosome. This ribosomal RNA is essential during protein synthesis because it provides a mechanism for maintaining the fidelity of translation (*1, 2*). Matching of the correct codon-anticodon forms a mini-helix that is directly monitored by the adenines of the internal loop in A-site rRNA. During decoding, a conformational change occurs in the internal loop of A-site involving the looping out of A1492 and A1493 (denoted here as A92 and A93) bases which interact with and stabilize the first two base pairs in the mini-helix (*3, 4*). In prokaryotes, the decoding site has been a major site for natural aminoglycosides antibiotics (*3, 5*). Upon binding, aminoglycosides induce the transition of A92 and A93 to the extra-helical conformation resulting in the stabilization of the mini-helix even if an incorrect anticodon-codon is paired (*6, 7*). The activity of aminoglycosides has been linked to their specific ability to bind the decoding-site and stabilize a looped out conformation (*8*). Aminoglycosides disrupt the fidelity of the anticodon-codon pairing, decrease the rate of protein production, and thereby cause cell death.

A key component of the decoding mechanism is the conformational switch involving the 2:1 adenine internal loop consisting of residues A92, A93 and A08. X-ray and NMR structures reveal that A92 or A93 can interact with A08 to form non-canonical A-A base pair pairs. A statistical overview of different A-site structures in the ribosome context also reveals that A92 and A93 can adopt intra- or extra-helical conformations in the absence of antibiotics (*9*) suggesting that the internal loop is intrinsically flexible. This flexibility is consistent with high-density B factors seen for internal loop bases in the X-ray and NMR structures in the absence of drugs (*6, 9, 10*). In addition, molecular dynamics (MD) simulations on unbound A-site rRNA revealed base flipping events occurring at picosecond timescales that involve single or double base transitions with several intermediate conformations (*11*). The energy landscape of flipping events traced for A-site rRNA showed that in the absence of drugs there is a major basin for the flip in state compared to the flip out states (*9, 11*). A lower energy barrier was also calculated for the in/out switch of A93 (~1.38 kcal/mol) compared with A92 (~1.68 - 3.5 kcal/mol) (*9, 11*).

In this study, we exploit the exquisite sensitivity of NMR carbon (^{13}C) relaxation experiments to characterize the conformational dynamics of A-site rRNA in the absence and presence of the aminoglycoside paromomycin. In particular, we are interested in gaining insight of the dynamic behavior of the internal loop adenines A92 and A93 that are essential for decoding and antibiotic activity. Carbon spin relaxation measurements allow us to monitor local motions occurring at picoseconds – nanoseconds timescales while ^{13}C relaxation dispersion measurements will provide information on slower motions occurring at microsecond – millisecond timescales. Our goal is to test the main

hypothesis that adenine residues can adopt the looped out conformation in the absence of the aminoglycoside or mini-helix.

3.2 Material and Methods

3.2.1 NMR sample preparation

Uniformly $^{13}C/^{15}N$ labeled A-site rRNA samples were prepared by *in vitro* transcription using T7 RNA polymerase (Takara Mirus Bio, Inc.), $^{13}C/^{15}N$ labeled NTPs (Cambridge Isotopes, Inc. and ISOTEC, Inc.), synthetic double stranded DNA templates containing the sequence of interest (Integrated DNA Technologies, Inc.) and the T7 promoter. The RNA was purified by 15% and 20% (w/v) denaturing polyacrylamide gel electrophoresis containing 1x TBE and 8M Urea for elongated (EAU-A-site and EGC-A-site) and short (A-site rRNA) RNAs respectively. The RNA was then electroeluted from the gel in 20 mM Tris pH 8 buffer followed by ethanol precipitation. The RNA pellet was dissolved and exchanged into NMR buffer (15 mM sodium phosphate, 0.1 mM EDTA, and 25 mM NaCl at pH ~6.4) using a 0.22 μM filter (Millipore Corp.). For the non-exchangeable NOE experiment, above prepared A-site rRNA sample was lyophilized in the presence of NMR buffer. The RNA pellet was then dissolved with 99.90% D_2O (Cambridge Isotope Laboratories, Inc.).

The A-site construct used in this study was derived from the *E.coli* ribosomal RNA sequence and it is the same model used in previous NMR studies (*1, 12, 13*). This sequence includes the universally conserved U-U base pair, adenine internal bulge (A1408, A1492, A1493), nucleotides important for aminoglycoside binding and the UUCG loop was used for stability of the RNA (*1*) (Figure 3.1A). A GC base pair was added to the second stem of this construct to have more measurements on the second

helix of this RNA as compared to helix one. This was very valuable during the analysis of relaxation data where the data from both helixes were compared. In addition, helix one was extended by two GC base pairs to optimize the RNA synthesis by *in vitro* transcription.

The elongated A-site rRNA samples were prepared elongating helix I by 22 NMR-invisible A-U or G-C Watson-Crick base pairs. In both constructs, two G-C base pairs were added at the end of the elongated helix to facilitate *in vitro* synthesis of the RNA. The constructs were uniformly $^{13}C/^{15}N$ AU (EGC-A-site rRNA) or GC (EAU-A-site rRNA) labeled respectively to avoid spectral overlap due to the elongation residues (Figure 3.1A).

3.2.2 NMR Spectroscopy Measurements

All NMR experiments were carried out on an Avance Bruker 600 MHz NMR spectrometer equipped with a triple-resonance 5-mm cryogenic probe at 298K. RNA samples of 250 to 300 uL in Shigemi tubes were used for all the experiments. NMR spectra were processed using NMRPipe/NMRDraw (*14*), analyzed using NMRDraw or NMRView (*15*) and overlaid using Sparky 3 (*16*).

All non-exchangeable and exchangeable resonances were assigned using standard NMR experiments (*17*). The exchangeable resonances (N1/3-H1/3) were assigned using a combination of 2D and 3D exchangeable $^{1}H-^{15}N$ NOESY-HSQC experiments. The non-exchangeable resonances (C1'/2/5/6/8-H1'/2/5/6/8) were assigned using a combination of 3D non-exchangeable $^{1}H-^{13}C$ NOESY-HSQC, 2D IP COSY (correlated H5 to H6) (*18, 19*), 2D HCN (*20*) and HCCH-COSY (correlates H2 to H8) experiments (*17, 21*). The

assignments were in good agreement with the ones previously reported by (*12, 13*), with the exception of A08C1' residue of the Asite rRNA – paromomycin complex.

Paromomycin chemical shift titrations were performed on A-site rRNA by recording 2D ^{13}C-^{1}H HSQC spectra upon incremental additions of the drug. Spectra of A-site rRNA (0.2 mM) were recorded with increments of 0, 0.05, 0.11, 0.20, 0.25, 0.30 and 0.60 mM paromomycin solution. This yielded a 99% bound A-site rRNA. A second titration yielding a 95% bound A-site rRNA (0.4 mM) was performed by adding 0, 0.04, 0.11, 0.20 and 0.39 mM paromomycin.

^{15}N spin relaxation was measured for guanine and uridine residues in both the non-elongated and elongated samples of A-site and mA-site rRNA. ^{15}N longitudinal (R_1) and transverse ($R_{2,CPMG}$) relaxation rates were measured using a combination of 2D (A-site, EAU-A-site) and 1D (EGC-A-site) experiments as described by (*22*). The R_1 experiments contained a heat compensation element to ensure constant heating during the different relaxation periods (*23*). The $R_{2,CPMG}$ experiment employed a $[0013]^N$ phase cycle in the Carr-Purcell-Meiboom-Gill (CPMG) pulse train to suppress artifacts arising from off-resonance effects (*24*). Two separate sets of R_1 and $R_{2,CPMG}$ experiments were run to get the guanine and uridine rates respectively. The delays used are summarized on Tables 3.1.

Table 3.1: Relaxation delays used in the carbon R_1 and $R_{2,CPMG}$ experiments for A-site. Duplicate and quadruplicate measurements used to estimate error are indicated using "(x2)" and "(x4)" respectively.

Delays (ms) for G experiments		
	R_1	$R_{2,CPMG}$
A-site rRNA	60, 720 (x2)	5.2, 130 (x2)
EAU-A-site rRNA	60, 1600 (x4)	6.2, 55.8 (x4)
Delays (ms) for U experiments		
	R_1	$R_{2,CPMG}$
A-site rRNA	60, 720 (x2)	5.2, 130 (x2)
EGC-A-site rRNA	60, 900 (x2)	6.2, 37.2 (x2)

Longitudinal (R_1) and rotating-frame ($R_{1\rho}$) relaxation rates were measured for A-site (in the presence and absence of paromomycin), EAU-A-site and EGC-A-site samples. The ^{13}C relaxation for the nucleobases C2, C5, C6 and C8 were measured using a TROSY-detected carbon relaxation experiment (*25-28*). A non-TROSY detected experiment was used to measure the relaxation data for the C1' (*25*). In the R_1 experiment, cross-relaxation to the neighboring carbons was suppressed by dephasing the carbon magnetization using gradients at the beginning of the pulse sequence followed by selective excitation of the carbon of interest using selective refocusing ^{13}C 180° pulses during the INEPT period. (*29*) Hansen and Al-Hashimi calibrated the spinlock powers used in the experiments (*25*) as previously described by Palmer *et.al* (*30*). Spinlock powers of 4.1 kHz, 5.1 kHz, 2.0 kHz and offsets of 2.8 kHz, -2.0 kHz, 2.0 kHz were used for the C2/C6/C8, C5 and C1' $R_{1\rho}$ experiments respectively. The high off-resonance spinlock powers were used to suppress the Hartman Hann transfers to scalar coupled carbon spins *(vide infra)* and minimize any chemical exchange contributions to the $R_{1\rho}$ measurements. Half Adiabatic passages were used to accurately align the $\pm C_z$ magnetization to and from the effective field tilt angle θ at the beginning as well as at the end of the relaxation period (*31*). A correction to the $R_{1\rho}$ rates was done to account for

off-resonance effects according to the $R_{1\rho} = R_1 \cos^2 \theta + R_2 \sin^2 \theta$ equation, in which $\theta = \arctan(\omega_{SL}/\Omega)$ is the effective tilt angle of the spinlock field, ω_{SL} is the spinlock field power in Hz and Ω is the resonance offset from the spinlock carrier frequency in Hz. The delays (T) used in the relaxation experiments were chosen as described by (*25*) such that the first delay is at or very close to zero and the last two to four points are 1.3T (*32*). All the delays used in the R_1 and $R_{1\rho}$ experiments are summarized in Table 3.2.

The $R_{1\rho}$ data for the C2, C6 and C8 nucleobases of EGC-A-site RNA were measured using a 1D off-resonance $R_{1\rho}$ experiment. In this experiment the carbon of interest was selectively excited as described by (*33*). Four or five point relaxation profiles were recorded using a spinlock power of 3.0 kHz and offset of 3.7 kHz. The C5 and C1' carbon relaxation measurements for EGC-A-site RNA (0.2mM) were not collected due to the non-optimal sample concentration. The delays used in the 1D ^{13}C Selective off-resonance $R_{1\rho}$ experiments are summarized in Table 3.3. All the relaxation rates and errors were determined by fitting the intensities to a mono-exponential decay using Origin 7.0 (OriginLab Corporation) and RlxAnalysis an in-house software. All the carbon relaxation measurements are summarized in Appendix 1.

Table 3.2: Relaxation delays used in the carbon R_1 and $R_{1\rho}$ experiments. Duplicate, triplicate or quadruplicate measurements used to estimate error are indicated by using "(x2)", "(x3)" and "(x4)" respectively.

	Delays (ms) for R_1 experiment		
	C2, C6, and C8	C5	C1'
A-site rRNA	20, 500 (x2)	20, 600 (x3)	20, 580 (x2)
EAU-Asite rRNA	20, 600 (x4)	20, 500 (x4)	20, 600 (x3)
EGC-Aiste rRNA	20, 540 (x2)		
A-site rRNA-paromomycin	20, 480 (x2)	20, 540 (x2)	20, 600 (x2)
	Delays (ms) for $R_{1\rho}$ experiment		
	C2, C6, and C8	C5	C1'
A-site rRNA	4, 25, 50 (x2)	4, 44 (x3)	4, 58 (x3)
EAU-Asite rRNA	4, 12, 20 (x2)	2, 12, 20 (x2)	2, 12, 26 (x2)
A-site rRNA-paromomycin	4, 25, 50 (x2)	4, 25, 50 (x2)	4, 22, 44 (x2)

Table 3.3: Relaxation delays used in the carbon $R_{1\rho}$ experiments for EGC-A-site rRNA. Duplicate measurements used to estimate error are indicated using "(x2)".

	Delays (ms) for $R_{1\rho}$ experiment	
	C2	C8
A08	0, 4 (x2), 8	
A92	0, 5 (x2), 10	0, 5 (x2), 10
A93	0, 4 (x2), 8, 12	0, 6 (x2), 12
A10	0, 3 (x2), 6	

A 1D selective ^{13}C $R_{1\rho}$ relaxation dispersion experiment was used to measure motions in the μs-ms time scale for A-site rRNA in the absence and presence of paromomycin. This experiment selectively excites the carbon of interest as described previously by Hansen *et. al* (*33*). A heat compensation block was implemented after acquisition time to maintain a constant radiofrequency power was applied to the sample. Four to seven point (including duplicates for error estimation) profiles were recorded per spinlock power. The spinlock powers used were 100, 200, 300, 400, 600, 800, 900, 1000, 1500, 2000, 2500, 3000, and 3500 Hz. These powers were calibrated as previously described (*25*). Duplicate $R_{1\rho}$ measurements at spinlock field strengths of 100, 400 and 800 Hz were also collected to account for measurement errors. For on-resonance data the carbon spinlock carrier was placed at the desired ^{13}C frequency of the resonance of interest. For off-resonance experiments the carbon spinlock carrier was placed at the desired offset (Ω) from the ^{13}C frequency of the resonance of interest. The off-resonance experiments were run at spinlock field strengths of 100, 400 and 800 Hz for C2/C8; 100, 500 and 1000 Hz for C1'. The offsets used in ± Hz are the following: {25, 50, 75, 100, 150, 200, 250 and 300} for 100 Hz, {50, 100, 150, 200, 250, 400, 800, 1000 and 1200} for 400Hz, {50, 100, 150, 200, 400, 600, 800, 1000, 1600, 2000 and 2400} for 800 Hz,

{50, 100, 150, 200, 250, 400, 600, 800, 900, 1200 and 1500} for 500 Hz, and {100, 150, 200, 250, 400, 600, 800, 1500, 1700, 2000, 2300, 2700, and 3000} for 1000 Hz spinlock powers. All the relaxation delays used in the experiments are summarized in tables 3.4 and 3.5. The same delays were used for the on- and off-resonance experiments respectively.

Table 3.4: Relaxation delays used in the ^{13}C $R_{1\rho}$ dispersion experiments for unbound A-site rRNA. Duplicate measurements used to estimate error are indicated using "(x2)".

	Delays (ms) for $R_{1\rho}$ experiment		
	C2	C8	C1'
A08	0, 4, 8, 16, 24 (x2)		
A92	0, 4, 12, 24, 32, 42(x2)	0, 4, 12, 24, 32, 42(x2)	0, 4, 8, 16, 24(x2)
A93	0, 4, 12, 24, 32, 42(x2)	0, 4, 12, 24, 32, 42(x2)	0, 2, 4, 6, 12(x2)
A10	0, 4, 12, 24, 32, 42(x2)		
G94	0, 4, 12, 24, 32(x2)		

Table 3.5: Relaxation delays used in the carbon $R_{1\rho}$ dispersion experiments for A-site rRNA 95% and 99% bound to paromomycin. Duplicate measurements used to estimate error are indicated using "(x2)".

	Delays (ms) for $R_{1\rho}$ experiment					
	95%			99%		
	C2	C8	C1'	C2	C8	C1'
A08		0, 16, 32 (x2)			0, 6, 18, 24, 40 (x2)	
A92	0, 16, 38 (x2)	0, 16, 32 (x2)		0, 6, 18, 24, 40 (x2)	0, 6, 18, 24, 40 (x2)	
A93	0, 24, 42 (x2)	0, 24, 42 (x2)	0, 12, 26 (x2)	0, 6, 18, 24, 40 (x2)	0, 6, 18, 24, 40 (x2)	0, 6, 24, 40 (x2)
A10	0, 16, 32 (x2)			0, 6, 18, 24, 40 (x2)		

3.2.3 Data Analysis

All resonance intensities (peak heights) were measured using 2D TROSY-HSQC spectra (*22*). The resonance intensities for all the ^{13}C-^{1}H spins were divided into groups defined by base type (A, U, G and C) and spin pair (C2-H2, C5-H5, C6-H6, C8-H8 and C1'-H1') for normalization. The resonances were further normalized to a minimum value of 0.1. Peaks that had unusually small intensities, which could be attributed to exchange broadening, were not used for the normalization to 0.1. These intensities appear as less than 0.1 in the plots (Figure 3.2A). The normalization was carried out independently for A-site (absence and in the presence of paromomycin), EAU-A-site and EGC-A-site samples.

All the $^{13}C/^{15}N$ R_1, ^{13}C $R_{1\rho}$ and ^{15}N $R_{2,CPMG}$ values were obtained by non-linear least squares fitting the peak height to the mono-exponential function $I_{(t)} = I_{(0)}e^{(-R_x t)}$, based on the Levenberg-Marquardt (LM) algorithm. The data was fitted using the Origin software (OriginLab Corporation). The 2D ^{13}C R_1 and $R_{1\rho}$ data was fitted using in-house software (*25*). The final $^{13}C/^{15}N$ R_2 values were corrected to account for the off-resonance effects (*24*). Uncertainties were also verified using duplicate, triplicate and quadruplicate relaxation measurements. The relative order parameter (S^2_{rel}) values were estimated from the ratio of $2R_2$-R_1 measured for each residue to that of the largest value in the well-structured RNA helix (*34*). The $2R_2$-R_1 values are, to a good approximation, proportional to $S^2 \times J(0)$, where J(0) is the spectral density function at zero field and S^2 is an order parameter used to describe motions occurring at time scales faster than the overall tumbling. In addition, $2R_2$-R_1 values are independent of the time scale of the internal motions and the number of contributing relaxation mechanisms under the assumption that

all the relaxation mechanisms experience similar amplitude of isotropic motions (*25, 34, 35*). All the R_1, R_2 and S^2_{rel} data are listed in Appendix 1 (Tables A1.1 to A1.4).

The maximum efficiency of Hartman-Hahn transfers between spins S and I were computed using the following equation (*36*)

$$A_{HAHA} = \left(1 + \left(\frac{\omega_{eff,I} - \omega_{eff,S}}{J_{IS}\left(1 + \cos(\theta_I - \theta_S)\right)/2}\right)^2\right)^{-1} \tag{3.1}$$

where $\omega_{eff,X} = (\omega_1^2 + \Omega_X^2)^{1/2}$ is the effective spinlock strength at spin X, $\theta_X = \text{atan}(\omega_1/\Omega_X)$ is the tip angle of the magnetization of spin X with respect to the static magnetic field and J_{IS} is the scalar coupling constant between spins S and I. The chemical shift of quaternary carbons in the purine bases were determined using a TROSY relayed HCCH-COSY experiment.(*21*) Data with A_{HAHA} of >1% for the C2-C4 or C2-C6 couplings (J_{CC} = -1 Hz), C8-C5 couplings (J_{CC} = 1 Hz) and >0.1% for C8-C4 or C8-C6 couplings (J_{CC} = 10 Hz), C2-C5 couplings (J_{CC} = 11 Hz), C1'-C2' couplings (J_{CC} = 40 Hz) were excluded from the analysis (Tables A1.4 to A1.6) (*37, 38*). Mono-exponential decays were observed for all the offset/power combinations for the C2 spins of {A08, A10, A92, A93}, C8 spins of {A92, A93, G94}, and C1' spins of {A92, A93} (Figure A1.1).

The chemical exchange data for A-site rRNA in the absence and presence of paromomycin were first analyzed by fitting the on-resonance dispersion data to the fast chemical exchange equation for a two site system (*33, 39*):

$$R_{1\rho} = R_1 \cos^2\theta + R_{2,0} \sin^2\theta + \sin^2\theta \frac{\Phi_{ex} k_{ex}}{k_{ex}^2 - \omega_{eff}^2} \tag{3.2}$$

where $\Phi_{ex} = p_a p_b \Delta\omega_{ba}^2$ was used as a single parameter and $\omega_{eff} = \sqrt{\omega_{13C}^2 + \Omega^2}$, $\Omega = 0$ is the resonance offset from the spinlock carrier, ω_{13C} is the spinlock field strength. The Φ_{ex}, R_2 and k_{ex} were allowed to vary during the fit. The chemical exchange parameters are not accurately measured using this equation due to the simplicity of this expression. For these reasons, the chemical exchange parameters were obtained by combining the on- and off-resonance data followed by fitting it to a two-site asymmetric population chemical exchange equation (*33, 39*):

$$R_{1\rho} = R_1 \cos^2\theta + R_{2,0} \sin^2\theta + \sin^2\theta \frac{p_a p_b \Delta\omega_{ab}^2 k_{ex}}{(\Omega + \Delta\omega_{ab}^2) + k_{ex}^2 + \omega_1^2} \tag{3.3}$$

where $\Omega \approx \Omega_a$ is the resonance offset from the spinlock carrier, ω_1 is the spinlock field strength, $\tan(\theta) = \omega_1/\Omega_{avg}$, , $\Omega_{avg} = p_a\Omega_a + p_b\Omega_b$, , p_a is the population of state a, p_b is the population of state b, $\Delta\omega_{ba} = \Omega_b - \Omega_a$ is the change in chemical shift for states a and b. A more accurate two-site chemical exchange expression (equation 1.4, described in the introduction) using the Laguerre's method for polynomial root finding was used to determine the chemical exchange parameters. (*39, 40*)

$$R_{1\rho} = R_{1\rho,\infty} + \frac{\sin^2\theta p_A p_B \Delta\omega^2 k_{ex}}{\frac{\omega_A^2\omega_B^2}{\omega_{eff}^2} + k_{ex} - \sin^2\theta p_A p_B \Delta\omega^2 k_{ex}\left(1 + \frac{2k_{ex}(p_A\omega_A^2 + p_B\omega_B^2)}{\omega_A^2\omega_B^2 + \omega_{eff}^2 k_{ex}^2}\right)} \tag{3.4}$$

Each data set (A08C2, A10C2, A92C8, A92C1', A93C1' and G94C8) was fitted individually allowing p_b, R_1, R_2, $\Delta\omega$, and k_{ex} to vary during the fit. A global fit using the A08C2, A92C1' and A93C1' data sets was done using equation 1.4. During this fit p_b and k_{ex} were shared among all the residues. All the parameters were also allowed to vary. All the analysis was implemented using the Origin software (OriginLab Corporation). The

best-fit parameters, were finally determined from F-statistics at the 99% confidence level (Table 3.6).

The free Gibbs energy (ΔG) was calculated using the following equation (*41*):

$$K_{flippingout} = e^{\left(\frac{-\Delta G^{o}_{flippingout}}{RT}\right)} \tag{3.6}$$

where K is the equilibrium constant ($K_{flipping\ out} = k_{AB}/k_{BA}$) and $\Delta G_{flipping\ out}$ is the free energy in kcal/mol for the flipping out event, T is the temperature in Kelvin (298.15 K) and R is the gas constant.

Table 3.6: Parameters obtained from chemical exchange analysis.

Base	R_2	R_1	k_{ex} (s^{-1})	p_b	$\Delta\omega/2\pi$ (Hz)
A93C1'	29 ± 1	1.3 ± 0.3	4265 ± 127	(2.5 ± 0.1) x10^{-2}	-774 ± 9
A92C1'	23 ± 0.4	1.6 ± 0.1			328 ± 7
A08C2	34 ± 0.1	1.4 ± 0.1			-123 ± 4
A10C1'	35 ± 0.1	2.02 ± 0.03			
G94C8	34 ± 0.1	2.4 ± 0.2			
A92C8	28 ± 0.1	2.7 ± 0.1			

3.3 Results

3.3.1 Resonance assignments of A-site and E-A-site rRNAs

The resonances of A-site rRNA were assigned using standard NMR experiments (*17*) using uniformly $^{13}C/^{15}N$ labeled RNA samples. The exchangeable NOE walk was continuously traced for both helixes respectively (from G03 to G94 and G91 to G17) (Figure 1.3). In addition, the non-exchangeable NOE connectivity was uninterrupted in both RNA strands indicating a continuous helical conformation of the RNA helixes. No or weak NOEs were found for the connection of G02 - G03 and C98 - C99 due to end

fraying effects of the RNA helix. A continuous inter-nucleotide NOE connectivity was observed for G94 – A92 – A93 – G91 suggesting that these adenines are stacked and bulged inside the helix. A weak NOE was also observed between H1' of A93 and H8 of A08 suggesting an inter-helical conformation for A08/A93 as well as a possible base pair interaction. These NOE connectivities were also observed by Fourmy *et. al.* when they solved the NMR structure of this oligonucleotide model of A-site rRNA (*12*). HCN, HNCCH-TOCSY and COSY experiments were also used to assign the base and sugar resonances. The 2D HCN experiment correlates the C6-H6/C8-H8 in the base to C1'-H1' resonances in the sugar ring through the N1/9 atoms of the same residue (*20*). The nitrogen (N1/N9) chemical shifts ranges for the HCN spectra are ^{15}N1 A/G (168-172 ppm), ^{15}N9 C (150-154 ppm) and ^{15}N9 U (144-148 ppm). The proton chemical shifts were then correlated to its corresponding carbon and nitrogen resonances using a 2D C8/C6-H8/H6 and C1'-H1' HSQC spectra (Figure 1.3). The HNCCH-TOCSY experiment was used to verify the imino and C8/C6 resonances of the guanine and uridine bases. The imino protons (H1/H3) were correlated to its corresponding carbon and nitrogen resonances using a 2D C8/C6-H8/H6 and N1/N3-H1/H3 HSQC spectra. The C5 chemical shifts were assigned using a 2D COSY experiment, which correlates the H5 and H6 protons (*18, 19*). Ultimately, the assignments were compared to those previously reported by Fourmy *et. al.* and they were found to be in good agreement (*12, 13*).

To study more in detail any motions occurring in the ps-ns time scales, we used the domain elongation strategy developed in the Al-Hashimi laboratory (*22*). The elongation scheme required the preparation of two elongated A-site rRNA constructs to avoid spectral crowding due to elongated resonances: EGC-A-site rRNA and EAU-A-site

rRNA (described in section 3.2.1, Figure 3.1A). The resonances of the elongated A-site rRNA were assigned by comparing its spectra with the non-elongated A-site rRNA spectra as described here. Shown on figure 3.1B are the 2D HSQC spectra obtained for the GC and AU elongated RNA samples. The asterisks denote the resonances that correspond to the two GC base pairs added at the end of the elongation site. The EGC- and EAU-A-site spectra exhibited excellent agreement when overlapped with the non-elongated A-site rRNA.

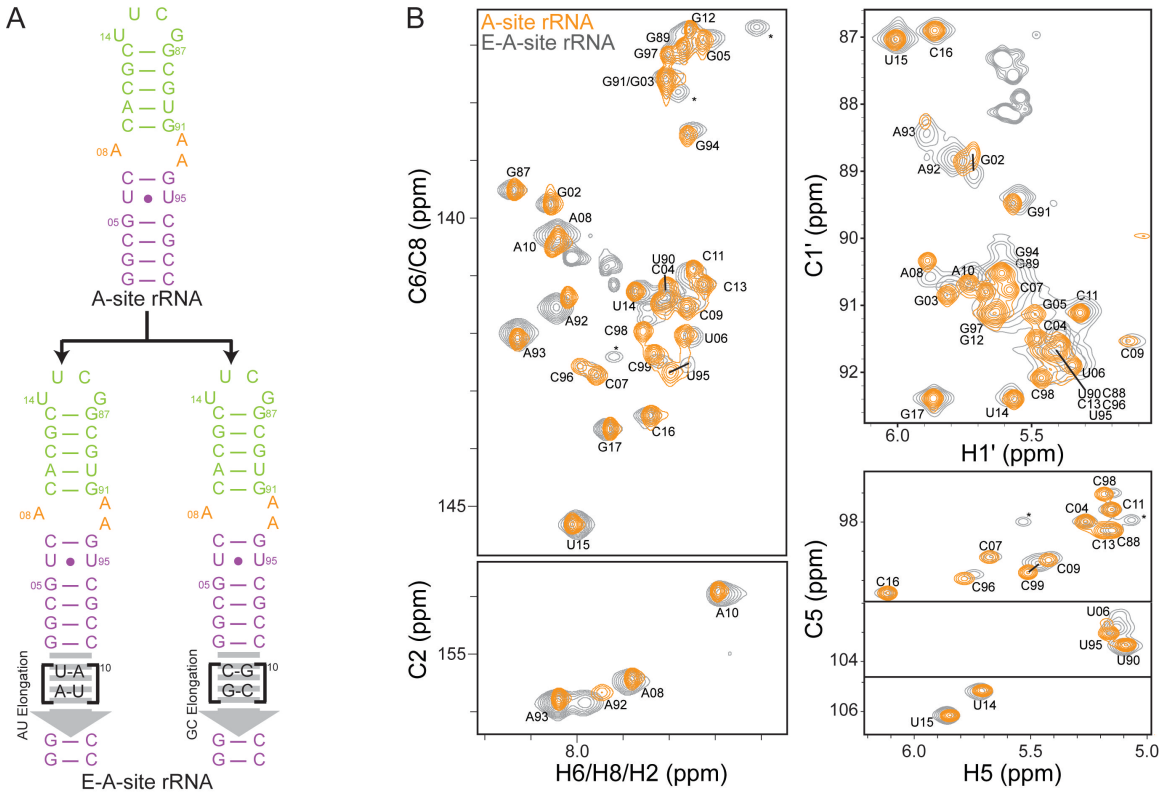

Figure 3.1: Resonance assignments of A-site and E-A-site rRNA. A) Secondary structure of non-elongated (top) and elongated (bottom) A-site rRNA. The purple (helix I), orange (internal loop), green (helix II), and gray (NMR invisible elongation site) represent different parts if the RNA. B) Overlay of 2D ^{13}C-^{1}H HSQC of E-Asite rRNA (gray) and non-elongated A-site rRNA (orange). C) Normalized resonance intensities for A-site (left) and E-A-site (right) rRNA. Shown are values for C1' (diamonds), C2 (circles), C5 (squares), C6 (triangles) and C8 (upside down triangles)

Only minor differences in chemical shifts were observed for residues close to the elongation site (the terminal end of helix I of the non-elongated RNA) (Figure 3.1B). Chemical shifts are very sensitive to the chemical environment of a given nucleus and thus these differences reflect the changes in the chemical environment at the elongation site. The excellent spectral overlay shows that the elongated RNA adopts the proper secondary structure without affecting the short A-site rRNA. The effective preparation of these elongated samples shows the applicability of this strategy to study the ps to ns dynamics of the A-site ribosomal RNA.

3.3.2 Picosecond-to-nanosecond motions of A-site rRNA by spin relaxation

Unusual resonances for the C8 and C1' atoms of A92 and A93 within the internal loop were observed in the A-site rRNA spectra (Figure 3.1B). The C8 resonances were shown downfield from usual purine C8 chemical shift while the C1' resonances were slightly shifted upfield. In addition, the spectra showed resonances that were line broadened as well as resonances that were very sharp. The line broadening effects are seen for residues located in the internal loop and the UU base pair. A combination of these effects reflects interesting structural and motional features in the decoding center of unbound A-site rRNA. These effects were observed in previous NMR studies of A-site rRNA but they were not characterized further (*12*). Of interest is to understand the dynamic behavior of A92 and A93 that are essential for A-site rRNA function.

To gain initial qualitative information of internal motions we examined the ^{13}C-^{1}H resonance intensities or peak heights of the non-elongated A-site rRNA. The non-elongated RNA has optimal relaxation properties for detecting any chemical exchange

contribution to a given site. The intensities were normalized to a minimum of 0.1 as described in section 3.2.3 In figure 3.2A, the resonances exhibit an array of intensities greater, equal and lower than 0.1. Resonances corresponding to helical parts of the RNA have intensities very close or equal to 0.1. Using this as a reference, we can conclude that greater or lower intensities correspond to the presence of local internal motions or exchange broadening, respectively. One site on A-site rRNA that displays high intensities is the UUCG apical loop, which is located at the tip of helix II. High intensities at this region correspond to the presence of domain and local motions as has been previously observed for other elongated RNAs such as TAR and P4 (*22, 42*). The residue A1408 in the internal loop have intensities comparable to those in the helix, suggesting that this adenine is staked within the two helices. This agrees very well with the available crystal and NMR structures of A-site rRNA that show A1408 loop inside the helix and stacked between both domains (*13, 43, 44*). The other two adenines of the internal loop (A1492 and A1493) display a combination of high and low intensities values. For example, A1493 has low intensities for the C1' spin while higher intensities are observed for the C2 and C8 spins (Figure 3.1C).

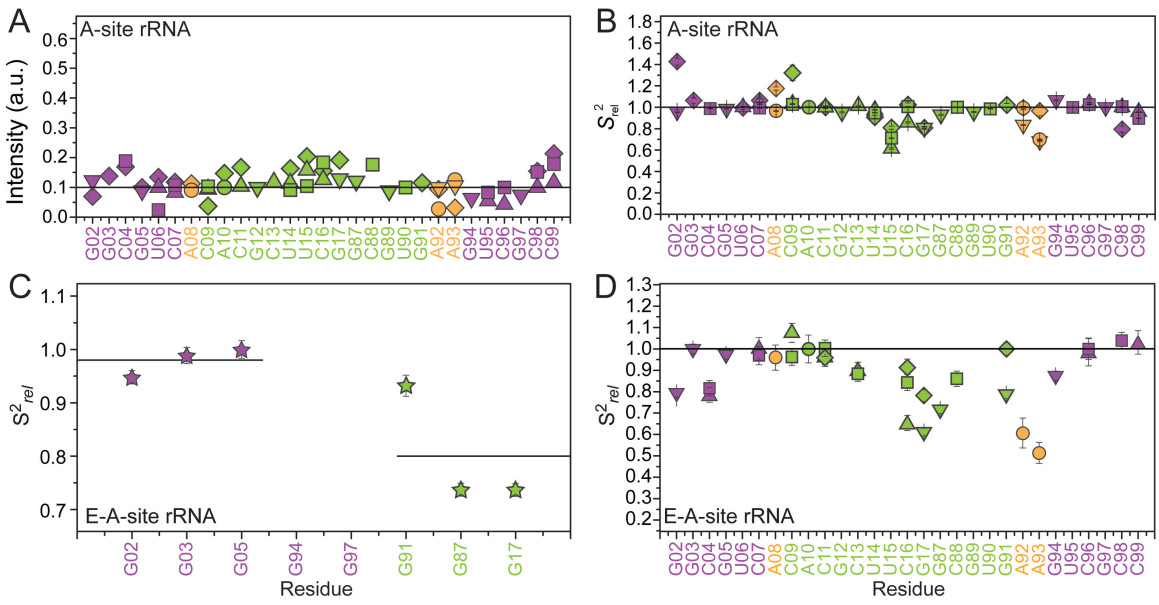

Figure 3.2: A-site rRNA dynamics. A) Normalized resonance intensities for A-site. ^{13}C qualitative order parameters (S^2_{rel}) are shown for non-elongate (B) and elongated (D) A-site rRNAs. Shown are values for C1' (diamonds), C2 (circles), C5 (squares), C6 (triangles) and C8 (upside down triangles). C) ^{15}N S^2_{rel} measurements for the N1 (stars) nucleobase of E-A-site rRNA.

These motions could be arising due to local fluctuations at the base and/or the base exchanging between a flipped "in" and "out" states. To shed light on this matter we collected carbon spin relaxation measurements to gain insight on the fast motions and carbon relaxation dispersion measurements for information on slow motions present in the internal loop.

We measured R_1 and R_2 relaxation rate constants for the C2, C8, C5 nucleobases and C1' sugar in the non-elongated A-site rRNA. Order parameters (S^2_{rel}) describing the amplitude of internal motions over picosecond-to-nanosecond timescales were then derived by normalizing the value of $S^2_{rel}= 2R_2-R_1$ for various spin types (see section 3.2.3) (*25, 34, 35*). The value of S^2_{rel} ranges between 1 and 0 for minimum and maximum motions. As expected, the S^2_{rel} values for helical regions are ~ 1 with deviations observed for terminal residues of helix I (Figure 3.2B and D) likely due to end fraying effects. The

adenine internal loop shows an array of S^2_{rel} values. Residue A08 has large $S^2_{rel} \sim 1$ values consistent with a looped in rigid state. By contrast, lower S^2_{rel} values consistent with great mobility is observed for A93 and A92, with greater mobility observed for A93 (Figure 3.2B). Fluorescence data for unbound A-site rRNA have shown that A93 is solvent exposed while A92 is mostly stacked within the helix (*8, 45*).

We also measured the corresponding carbon and nitrogen spin relaxation data for elongated RNA constructs. Here, the elongation decouples internal and overall motions, and makes it possible to probe collective motions between the helices which may evade detection in the non-elongated constructs (*22*). By slowing down the overall tumbling of the molecule, the elongation also broadens the timescale sensitivity of the spin relaxation data deep into the nanosecond timescales. Hence it could be possible that A93 has a greater degree of extra-helical conformation allowing greater amplitude of local motions at this site.

Figure 3.2C shows the ^{15}N S^2_{rel} values for E-A-site rRNA. The uniformly smaller S^2_{rel} values measured for helix II as compared to helix I indicates the existence of inter-helical motions about the flexible adenine rich internal loop. Residue G91 shows an anomalously high ^{15}N S^2_{rel} values. This can be attributed to (i) presence of exchange broadening (see below) and (ii) possibly to the unique of orientation of the $^{15}N - {}^{1}H$ bond vector relative to the elongated axis (*22, 25*).

The ^{13}C S^2_{rel} measurements for E-A-site rRNA (Figure 3.2D) follow the same trend seen for non-elongated A-site rRNA. The apical UUCG loop shows the lowest S^2_{rel} values consistent with previous studies of other elongated RNAs (*22, 42*). Again

significant mobility is observed for A92 and A93 with greater flexibility observed for A93 (Figure 3.2D).

3.3.3 Microsecond-to-millisecond motions of A-site rRNA by ^{13}C relaxation dispersion

To study slower micro-to-millisecond motions in A-site rRNA that might be important for decoding, we performed ^{13}C relaxation dispersion measurements. For a two-state dynamic transition between an A and B state, A $\Leftrightarrow$ B, these experiments can provide the exchange rate (k_{ex}), change in chemical shift between both states ($\Delta\omega_{AB}$) and the population of both states (p_A and p_B). In particular, we used a 1D selective ^{13}C $R_{1\rho}$ dispersion experiment (*33*) to measured data for C2, C8 and/or C1' in A08, A10, A92, A93, and G94 (Figure 3.3A-E). Key statistics for this analysis are summarized in Table 3.6. As expected, we did not observed any evidence for exchange at C2 of A10 located in the canonical helix. Likewise, we did not observe any chemical exchange for the nucleobases of A92 and A93 in the internal loop as well as G94. However, we did observe chemical exchange for C2 in the nucleobase of A08 as well as in the sugar C1' carbons of A92C1' and A93C1' (Figure 3.3A-C).

Interestingly, F-statistics with 99% confidence revealed that these data could be fitted simultaneously to a single exchange process indicating that they all report on the same concerted molecular event. The fitting yielded a rate of 4265 ± 127 s^{-1} and a low populated "invisible state" of 2.5%. The sign and magnitude of the chemical shift difference ($\Delta\omega$) with the "invisible" state was obtained for these resonances. The $\Delta\omega$ values are -0.81 ± 0.03 ppm, 2.17 ± 0.05 ppm and -5.13 ± 0.06 ppm for A08C2,

A92C1' and A93C1' respectively. This slow transition occurring on a timescale of 234 μs timescales may reflect the looping in and out of the adenines.

Taken together, the carbon spin relaxation and relaxation dispersion data reveals a complex manifold of fast picosecond-to-nanosecond motions in the nucleobases that correlate with stacking interactions and slower microsecond motions in the sugar backbone that may reflect transitions between looped in and out states.

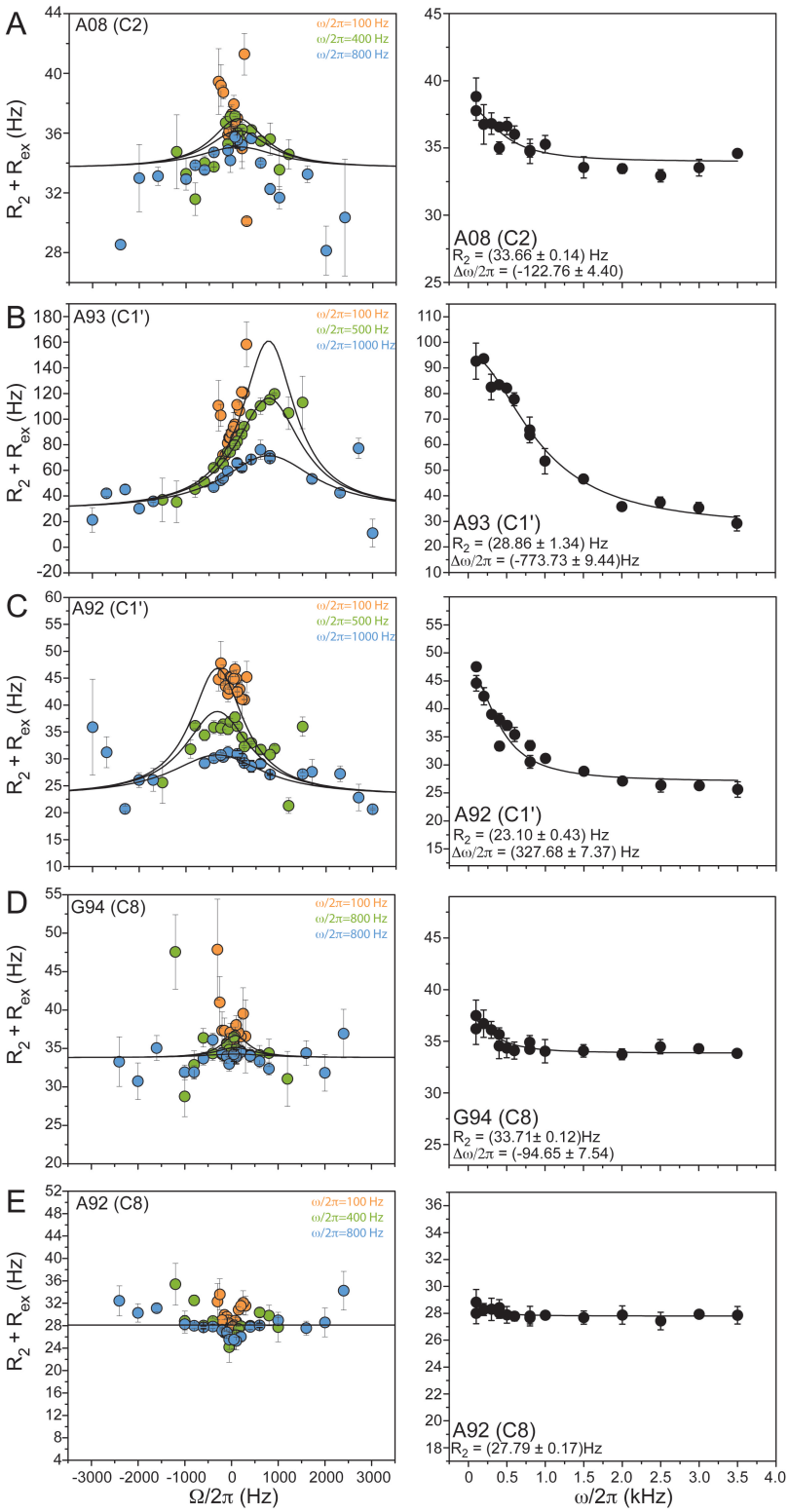

Figure 3.3: Characterization of slow motions in A-site rRNA. Relaxation dispersion profiles for: C2 in A08 (A), C1' in A93 (B), C1' in A92 (C), C8 in G94 (D), and C8 in A92 (E). The left panels show the offset (Ω/2π) and power (ω/2π) dependence of R_2 at spinlock powers of 100 (orange), 400 or 500 (green), 800 or 1000 (blue) Hz. The right panels show the on-resonance dependence of R_2.

3.3.4 Structural dynamics of A-site rRNA in the presence of the aminoglycoside paromomycin

Previous studies have shown that upon binding aminoglycosides such as paromomycin, A92 and A93 adopt an extra-helical looped out conformation. If the motions observed in unbound A-site were somehow connected to the looping in and out dynamics, then we would expect changes in these dynamics upon paromomycin binding. Thus, to gain further insights into the motions observed in unbound A-site and also characterize the dynamical properties of the "inactive" drug bound states, we used the same NMR methodology to characterize the dynamics of A-site rRNA when bound to paromomycin. As shown in Figure 3.4A, incremental addition of paromomycin led to large and specific changes in 2D HSQC spectra of A-site rRNA. The largest chemical shift perturbations were observed in and around the adenine internal loop, which is the site of binding. In contrast, little to no changes were observed in the UUCG loop, which is remote from the binding site. These changes are consistent with previously reported NMR spectra of A-site – paromomycin complex (*12*).

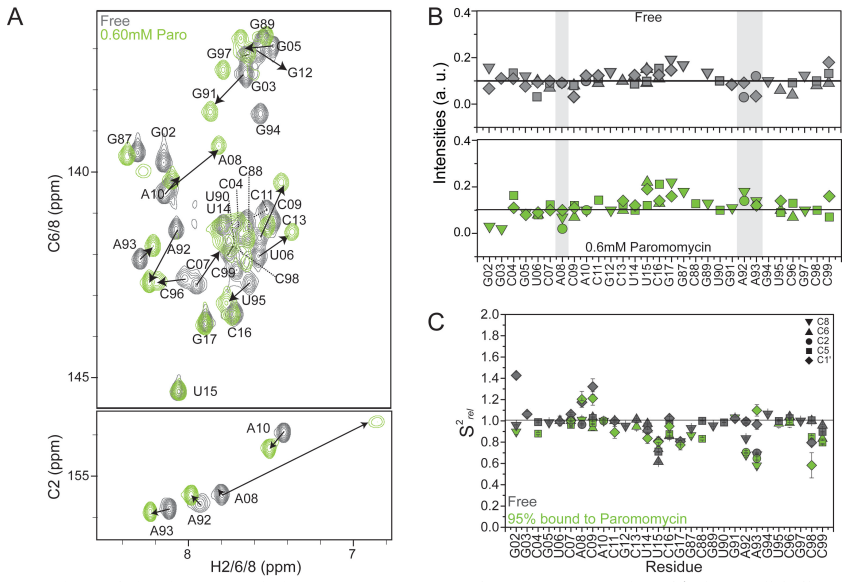

Figure 3.4: Dynamics of A-site rRNA in the presence of paromomycin. A) 2D HSQC spectra of A-site rRNA in the presence of 0.6 mM paromomycin. B) Normalized resonance intensities. C) S^2_{rel} measurements. Shown are values for C1' (diamonds), C2 (circles), C5 (squares), C6 (triangles) and C8 (upside down triangles). D) Relaxation dispersion profiles for C2 in A10, A92 and A93.

Addition of paromomycin also resulted in significant changes in the intensities of the internal loop resonances indicating that it induces changes in their intrinsic dynamic properties. In particular, a large increase in the resonance intensities of the nucleobases C2, C8 and C1' of A92 and A93 was observed on paromomycin binding indicating an increase in fast ps – ns motions and consistent the two bases adopting a flexible looped out conformation. Such an increase in the local mobility of A92 and A93 on binding aminoglycosides was also observed using fluorescence measurements (*8, 45, 46*). By contrast, paromomycin binding induced exchange broadening in internal loop residue A08 indicating that the complex is dynamic in nature. Finally, paromomycin binding resulted in little to no changes in the resonance intensities of residues in the helix and UUCG loop.

We measured ^{13}C R_1 and R_2 relaxation measurements for the C2, C8, C5 and C1' nucleobases in the non-elongated A-site rRNA 95% bound to paromomycin. The S^2_{rel} measurements were also determined based on the calculation of $2R_2$-R_1. These values were then compared to values measured in unbound A-site rRNA. As shown on figure 3.4C, the helical parts of the RNA exhibited S^2_{rel} near or equal to 1. Again, deviations were seen at the terminal ends due to end fraying effects. Very little to no changes were observed for the UUCG apical loop S^2_{rel} measurements going from unbound to bound A-site rRNA. The residue A08 shows enhanced S^2_{rel} measurements when compared to unbound A-site rRNA indicative of exchange broadening. The S^2_{rel} values for A92 were significantly attenuated upon ligand binding. For A93, the changes were not as significant but it did become more flexible. Lower S^2_{rel} values are observed for C2 and C8 nucleobases of A93 as compared to A92, indicating that A93 remains more flexible than A92 even in the paromomycin-bound state. The only exception is A93C1' which exhibits exchange broadening in the 95% bound state.

Next, we performed carbon relaxation dispersion experiments to characterize slow motions in A-site rRNA 95% and 99% bound to paromomycin (Figure 3.5). Binding of paromomycin quenched most of the exchange broadening observed at A92C1', A92C8, A93C1'. By contrast, paromomycin binding induced exchange broadening specifically at A08. Thus, in the 99% bound state, significant exchange could only be detected at residues A08 and to a much lesser degree in A93C1'. Again, these data suggest that the complex remains dynamic in nature consistent with MD simulations which observe looping in and out transitions of A92 and A93 even when in complex with gentamicin (*9*).

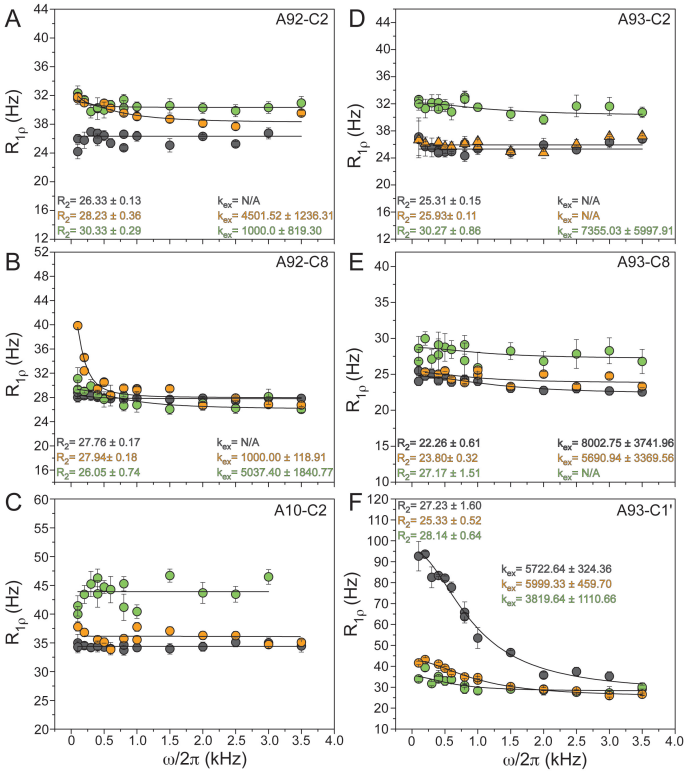

Figure 3.5: Relaxation dispersion profiles for A-site rRNA bound to paromomycin. On-resonance dependence on $R_{1\rho}$ for: C2 in A92 (A), C8 in A92 (B), C2 in A10 (C), C2 in A93 (D), C8 in A93 (E) and C1' in A93 (F). Shown are the data for A-site rRNA unbound (black), 95% bound (orange) and 99% bound (green). The insert in all the plots is the R_2 and k_{ex} values for each fit.

3.3.5 The "invisible" excited state of unbound A-site rRNA exhibits a drug bound-like conformation

What is the excited state observed by relaxation dispersion measurements of unbound A-site? Several lines of evidence suggest that this corresponds to a conformation in which the adenines are flipped out as observed in the drug bound state. First, the sign of the $\Delta\omega_{disp} = \omega_{excited} - \omega_{ground}$ for A08C2, A92C1' and A93C1', as calculated by carbon relaxation dispersion measurements, is consistent with the corresponding chemical shift difference observed between unbound and bound A-site $\Delta\omega$

$= \omega_{\text{bound}} - \omega_{\text{unbound}}$. In other words, the chemical shifts of the excited state are similar to the chemical shifts observed for A-site when bound to paromomycin. While we do not expect perfect agreement with respect to the magnitude of the perturbations, this is not to be expected given that the presence of the drug itself, in addition to the conformational exchange, affects the chemical shifts observed in the drug bound state. We were able to support these data by performing DFT calculations of carbon chemical shifts on a variety of unbound A-site rRNA structures. This allowed us to compute $\Delta\omega_{DFT}$ between a variety of states including ones in which both A92/A93 are completely looped in, looped out, or partially loop in and out in various combinations. The best agreement was observed for $\Delta\omega_{DFT} = \omega_{(\text{partially loop out})} - \omega_{(\text{loop in})}$.

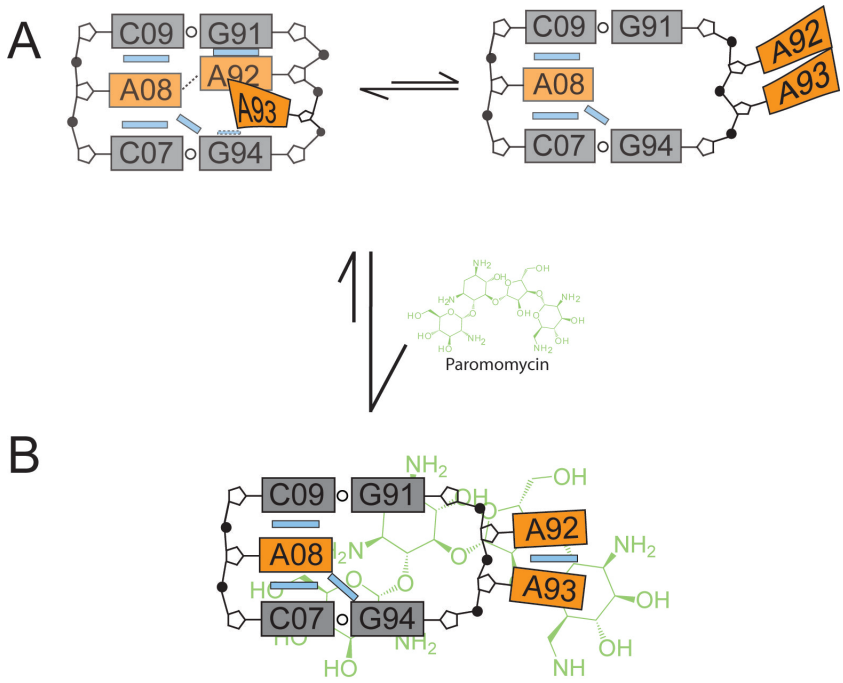

Figure 3.6: Proposed model for A-site in the absence and presence of paromomycin. A) Proposed "ground" (left) and "invisible" (right) states. B) Proposed bound state. Shown are: GC closing base pairs (gray), internal loop adenines (orange), stacking interactions (blue boxes), paromomycin (green).

Second, the free energy difference between the ground and excited states measured by relaxation dispersion (2.17 kcal/mol) is in good agreement with the values computed using replica exchange MD simulations (0.8 kcal/mol) (*9*).

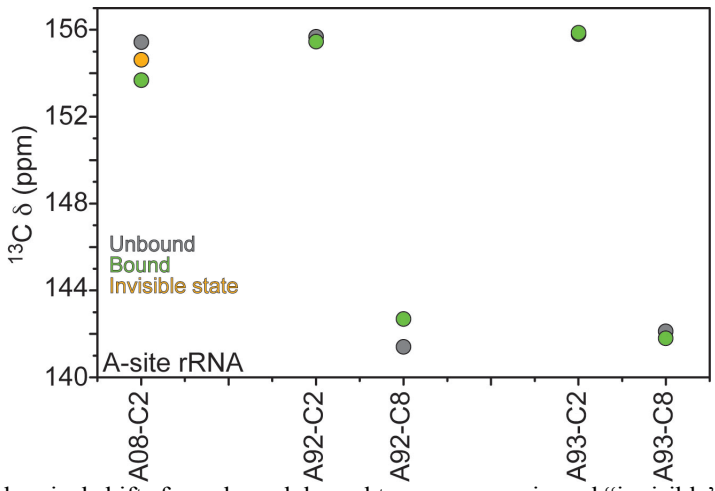

Figure 3.7: Carbon chemical shifts for unbound, bound to paromomycin and "invisible" state for A-site rRNA

3.4 Conclusion

Our results show that unbound A-site rRNA experiences fast and slow conformational dynamics and these motions might be important for decoding mechanism. The nitrogen spin relaxation data shows the presence of inter-helical motions about the flexible adenine rich internal loop. In addition, ^{13}C S^2_{rel} showed that A93 have higher amplitude motions than A92, while A08 always had values comparable to the helical regions. The carbon dispersion relaxation experiments showed that A08C2, A92C1' and A93C1' are experiencing a single exchange process with a rate of 234 μs and a population of the "invisible" state of 2.5%.

First, we proposed that the "invisible" state is a bound-like state where A92 and A93 are flipped out of the helix as observed in the bound state (Figure 3.6A, right panel). The direction of the chemical shift agrees with the bound state (Figure 3.7) suggesting

that the adenines in the invisible state are adopting an extra-helical conformation like in the bound state. The free energy of flipping out also agrees with the one calculated by MD simulations of A-site rRNA. We proposed that the "ground" state of this process is when A92 and A93 adopt a more intra-helical state. Within this intra-helical state, our data suggest that A92 is more stacked within the helix and A93 adopts a more partially out dynamical conformation (Figure 3.6A, left panel). This is consistent with the chemical shift positions of the nucleobases C2/C8 for A92 and A93 respectively. The C2 and C8 chemical shifts for A92 are more upfield compared to the resonances of A93. This upfield position is characteristic for residues in a helix or undergoing stacking (Figure 3.1B) (*47*). Second, the carbon spin relaxation data shows that A93 is more flexible than A92. These results agree very well with the previously shown 2-aminopurine fluorescence data for unbound A-site rRNA that shows that A93 is more solvent exposed and A92 stacked inside the helix 69% of the time (*8, 45*). Third, upon ligand binding the chemical shift and carbon spin relaxation values for A93 resonances barely change, suggesting that this adenine partially looped out the helix. In contrast, the direction of change in chemical shift upon ligand binding for A92 and the dramatically decreased S^2_{rel} measurements in the presence of paromomycin indicate that A92 undergoes a conformational change towards looping out. This conformational state has a population of 97.5% and it is more energetically favored when compared to the "invisible" state. In both states we propose that A08 is always in an intra-helical state. The chemical shift of A08 C8 is located at the same region as A10, in the canonical helix. The resonance intensities and S^2_{rel} measurements for A08 were also observed to be comparable with the helical parts of the unbound A-site rRNA. Hence, the exchange

experienced by A08C2 represents the change in chemical environments produced by the flipping events in A92 and A93.

In the presence of paromomycin, A92 and A93 flip outside the helix, stack with each other and become more flexible. Furthermore, the chemical exchange observed in unbound A-site rRNA dramatically gets attenuated once its ~99% bound to paromomycin. This shows that the tightly bound drug locks the adenine in the extra-helical conformation (Figure 3.6B). Nevertheless, the fact that chemical exchange was not completely quenched for A93C1' suggests the possibility that this adenines might be experiencing different extra-helical states. To further characterize any possible conformational exchange in the bound state, more data acquisition and analysis are needed. For example, off-resonance data for the carbon relaxation dispersion experiments needs to be collected in order to obtain information of other possible states.

Some of this work has been published on the Journal of the American Chemical Society (*33*). The idea was conceived by Casiano-Negroni, A. and Al-Hashimi, H. M. The undergraduate student Gulati, N synthesized the elongated RNA. Hansen, A. L. designed and implemented the ^{13}C relaxation dispersion experiments. Nikolova, E. performed the DFT calculations and was involved with implementing the ^{13}C relaxation dispersion experiment. Casiano-Negroni, A, collected and analyzed the NMR data.

3.4 References

1. Hermann, T. (2006) A-site model RNAs, *Biochimie 88*, 1021-1026.
2. Green, R., and Noller, H. F. (1997) Ribosomes and translation, *Annual Review of Biochemistry 66*, 679-716.
3. Ogle, J. M., and Ramakrishnan, V. (2005) Structural insights into translational fidelity, *Annual Review of Biochemistry 74*, 129-177.
4. Ogle, J., Carter, A. P., and Ramakrishnan, V. (2003) Insights into the decoding mechanism from recent ribosome structures, *Trends In Biochemical Science 28*, 259-266.
5. Vicens, Q., and Westhof, E. (2003) RNA as a drug target: the case of aminoglycosides, *Chembiochem 4*, 1018-1023.

6. Recht, M. I., Fourmy, D., Blanchard, S. C., Dahlquist, K. D., and Puglisi, J. (1996) RNA sequence determinants for aminoglycoside binding to an A-site rRNA model aligonucleotide, *Journal of Molecular Biology 262*, 421-436.
7. Daviter, T., Gromadski, K. B., and Rodnina, M. V. (2006) The ribosome's response to codon-anticodon mismatches, *Biochimie 88*, 1001-1011.
8. Kaul, M., Barbieri, C. M., and Pilch, D. S. (2006) Aminoglycoside-Induce Reduction in Nucleotide Mobility at the Ribosomal RNA A-Site as a Potentially Key Determinant of Antibacterial Activity, *Journal of the American Chemical Society 128*, 1261-1271.
9. Vaiana, A. C., and Sanbonmatsu, K. Y. (2009) Stochastic gating and drug-ribosome interactions, *Journal of Molecular Biology 386*, 648-661.
10. Lynch, S. R., Gonzales, R. L., Jr, and Puglisi, J. (2003) Comparison of X-Ray Crystal Structure of the 30S Subunit-Antibiotic Complex with NMR Structure of Decoding Site Oligonucleotide-Paromomycin Complex, *Structure 11*, 43-53.
11. Sanbonmatsu, K. Y. (2006) Energy landscape of the ribosomal decoding center, *Biochimie 88*, 1053-1059.
12. Fourmy, D., Yoshizawa, S., and Puglisi, J.D. (1998) Paromomycin Bidning Induces a Local Conformational Change in the A-site of 16 S rRNA, *Journal of Molecular Biology 277*, 333-345.
13. Fourmy, D., Recht, M. I., Blanchard, S. C., and Puglisi, J. D. (1996) Structure of the A site of Escherichia coli 16S ribosomal RNA complexed with an aminoglycoside antibiotic, *Science 274*, 1367-1371.
14. Delaglio, F., Grzesiek, S., Vuister, G. W., Zhu, G., Pfeifer, J., and Bax, A. (1995) Nmrpipe - a Multidimensional Spectral Processing System Based On Unix Pipes, *Journal of Biomolecular Nmr 6*, 277-293.
15. Johnson, B. A., and Blevins, R. A. (1994) Nmr View - A Computer-Program For The Visualization And Analysis Of Nmr Data, *Journal Of Biomolecular Nmr 4*, 603-614.
16. Goddard, T. D. K., D.G. (2004) SPARKY 3, in *University of California, San Francisco*.
17. Furtig, B., Richter, C., Wohnert, J., and Schwalbe, H. (2003) NMR spectroscopy of RNA, *Chembiochem 4*, 936-962.
18. Xia, Y. L., Legge, G., Jun, K.Y., Qi, Y., Lee, H., and Gao, X. (2005) IP-COSY, a totally in-phase and sensitive COSY experiment., *Magnetic Resonance in Chemistry 43*.
19. Fiala, R., Czernek, J., and Sklenar, V. (2000) Transverse relaxation optimized triple-resonance NMR experiments for nucleic acids, *Journal of Biomolecular Nmr 16*, 291-302.
20. Sklenar, V., Peterson, R.D, Rejente, M.R., and Feigon, J. (1993) 2-Dimensional And 3- Dimensional Hcn Experiments For Correlating Base And Sugar Resonances In N-15,C-13-Labeled Rna Oligonucleotides., *Journal of Biomolecular NMR 3*, 721-727.
21. Simon, B., Zanier, K., and Sattler, M. (2001) A TROSY relayed HCCH-COSY experiment for correlating adenine H2/H8 resonances in uniformly C-13-labeled RNA molecules, *Journal of Biomolecular NMR 20*, 173-176.

22. Zhang, Q., Sun, X., Watt, E. D., and Al-Hashimi, H. M. (2006) Resolving the motional modes that code for RNA adaptation, *Science 311*, 653-656.
23. Yip, G. N., and Zuiderweg, E. R. (2005) Improvement of duty-cycle heating compensation in NMR spin relaxation experiments, *J Magn Reson*.
24. Yip, G. N., and Zuiderweg, E. R. (2004) A phase cycle scheme that significantly suppresses offset-dependent artifacts in the R2-CPMG 15N relaxation experiment, *J Magn Reson 171*, 25-36.
25. Hansen, A. L., and Al-Hashimi, H.M. (2007) Dynamics of Large Elongated RNA by NMR Carbon Relaxation, *Journal of the American Chemical Society 129*, 16072-16082.
26. Loria, J. P., Rance, M., and Palmer, A. G. (1999) A TROSY CPMG sequence for characterizing chemical exchange in large proteins, *Journal of Biomolecular Nmr 15*, 151-155.
27. Zhu, G., Xia, Y. L., Nicholson, L. K., and Sze, K. H. (2000) Protein dynamics measurements by TROSY-based NMR experiments, *Journal of Magnetic Resonance 143*, 423-426.
28. Igumenova, T. I., Palmer, A. G. III. (2006) Off-resonance TROSY-selected R 1rho experiment with improved sensitivity for medium- and high-molecular-weight proteins., *Journal of the American Chemical Society 128*, 8110-8111.
29. Yamazaki, T., Muhandiram, R., and Kay, L. E. (1994) Nmr Experiments for the Measurement of Carbon Relaxation Properties in Highly Enriched, Uniformly C-13,N-15-Labeled Proteins - Application to C-13(Alpha) Carbons, *116*, 8266-8278.
30. Palmer III, A. G., Kreoenke, C. D., and Loria, P. J. (2001) Nuclear Magnetic Resonance Methods for Quantifying Microsecond-to-Millisecond Motions in Biological Macromolecules *Methods in Enzymology 339*, 204-238.
31. Mulder, F. A. A., de Graaf, R.A., Kaptein, R., and Boelens, R. (1998) An Off-resonance Rotating Frame Relaxation Experiment for the Investigation of Macromolecular Dynamics Using Adiabatic Rotations, *Journal of Magnetic resonance 131*, 351-357.
32. Jiang, F., Kumar, R. A., Jones, R. A., and Patel, D. J. (1996) Structural basis of RNA folding and recognition in an AMP-RNA aptamer complex [see comments], *Nature 382*, 183-186.
33. Hansen, A. L., Nikolova, E.N., Casiano-Negroni, A. and Al-Hashimi, H. M. (2009) Extending the range of microsecond-to-millisecond chemical exchange detected in labeled and unlabeled nucleic acids by selective carbon R(1rho) NMR spectroscopy., *Journal of the American Chemical Society 131*, 3818-3819.
34. Dethoff, E. A., Hansen, A. L., Musselman, C., Watt, E. D., Andricioaei, and Al-Hashimi, H. M. (2008) Characterizing complex dynamics in the transactivation response element apical loop and motional correlations with the bulge by NMR, molecular dynamics, and mutagenesis, *Biophysics Journal 95*, 3906-3915.
35. Fushman, D., Tjandra, N., and Cowburn, D. (1999) An Approach to direct determination of protein dynamics from N-15 NMR relaxation at multiple fields, independent of variable N-15 chemcial shift anisotropy and chemcial exchange controbutions., *Journal of the American Chemical Society 121*, 8577-8582.

36. Bax, A., and Davis, D. G. (1985) Practical Aspects Of Two-Dimensional Transverse Noe Spectroscopy, *Journal of Magnetic Resonance 63*, 207-213.
37. Wijmenga, S. S., and van Buuren, B. N. M. (1998) The use of NMR methods for conformational studies of nucleic acids, *Progress in Nuclear Magnetic Resonance Spectroscopy 32*, 287-387.
38. Fiala, R., Munzarova, M.L., and Sklenar, V. (2004) Experiments for correlating quaternary carbons in RNA bases., *Journal of Biomolecular NMR 29*, 477-490.
39. Palmer III, A. G., and Massi, F. (2006) Characterization of the Dynamics of Biomacromolecules Using Rotating-Frame Spin Relaxation NMR Spectroscopy, *Chemical Reviews 106*, 1700-1719.
40. Miloushev, V. Z., and Palmer III, A. G. (2005) R1ρ relaxation for two-site chemical exchange: General approximations and some exact solutions, *Journal of Magnetic resonance 177*, 221-227.
41. Rinnenthal, J., Klinkert, B., Narberhaus, F., and Schwalbe, H. (2010) Direct observation of the temperature-induced melting process of the Salmonella fourU RNA thermometer at base-pair resolution, *Nucleic Acids Research 38*, 3834-3847.
42. Getz, M. M., Andrews, A. J., Fierke, C. A., and Al-Hashimi, H. M. (2007) Structural plasticity and Mg2+ binding properties of RNase P P4 from combined analysis of NMR residual dipolar couplings and motionally decoupled spin relaxation, *RNA 13*, 251-266.
43. Wimberly, B. T., Brodersen, D. E., Clemons, W. M., Morgan-Warren, R. J., Carter, A. P., Vonrhein, C., Hartsch, T., and Ramakrishnan, V. (2000) Structure of the 30S ribosomal subunit, *Nature 407*, 327-339.
44. Schuwirth, B. S., Borovinskaya, M. A., Hau, C. W., Zhang, W., Vila-Sanjurjo, A., Holton, J. M., and Cate, J. H. D. (2005) Structures of the bacterial ribosome at 3.5 A resolution *Science 310*, 827-834.
45. Dibrov, S. M., Parsons, J., and Hermann, T. (2010) A model for the study of ligand binding to the ribosomal RNA helix h44, *Nucleic Acids Research 38*, 4458-4465.
46. Kaul, M., Barbieri, C. M., and Pilch, D. S. (2004) Fluorescence-based approach for detecting and characterizing antibiotic-induced conformational changes in ribosomal RNA: comparing aminoglycoside binding to prokaryotic and eukaryotic ribosomal RNA sequences, *Journal of the American Chemical Society 126*, 3447-3453.
47. Fares, C., Amata, I., and Carlomagno, T. (2007) 13C-detection in RNA bases: revealing structure-chemical shift relationships, *Journal of the American Chemical Society 129*, 15814-15823.

Chapter 4

Dynamics of a drug-resistant mutant A-site ribosomal RNA in the presence and absence of paromomycin

4.1 Introduction

Prokaryotic ribosomes carrying this A1408G mutation do not show change in ribosome function but do show significant resistance for 2-deoxystreptamine aminoglycosides (*1*)(*2*)(*3*)(*4*). Clinical studies have shown that patients infected with *Mycobacterium abscessus* carrying this mutation (A1408G) do not respond positively when treated with the aminoglycoside amikacin (*5*). The clinical isolates of this bacterium was also shown to be highly resistant to all the 2-deoxystreptamine aminoglycosides including neomycin, tobramycin, and paromomycin among others (*5*). Further, *in vitro* studies employing isolated A-site constructs revealed that the single A1408G mutation (mA-site rRNA) resulted in >100-fold reduction in the aminoglycoside binding affinity (*4*)(*3*)(*6*). The NMR solution structure of an oligonucleotide model of prokaryotic A-site rRNA carrying the A1408G mutation in the absence of aminoglycosides revealed differences relative to wild-type A-site specifically at the

internal loop; G08 is rotated towards the major groove (aminoglycoside binding pocket) and residues A92 and A93 are significantly more disordered (*7*). Yet the NMR structure of mA-site rRNA complexed with the aminoglycoside paromomycin (*6*) along with 2-aminopurine fluorescence studies (*8*) showed that aminoglycoside binding does not lead to the flipping out of A1492 and A1493 as observed in wild-type A-site rRNA. The >100-fold reduction in binding affinity was therefore attributed to disruption of the binding pocket for ring I of paromomycin most likely resulting from the change in geometry of G1408 – A1493 base pair and the conformation of G1408 where its carbonyl group is projected towards the major grove of the RNA (*6*)(*3*). In addition, MD simulations of the mutant A-site complexed to paromomycin show that the flipping in and out events of A92/A93 were less frequent than in the wild-type A-site RNA (*9*). These observations suggest that conformational change in the internal loop of A-site rRNA upon drug binding might be a key factor in the specificity and mechanism of action.

In this study, we characterize the dynamics of mutant A-site rRNA in the presence and absence of the aminoglycoside paromomycin using the same NMR scheme used to characterize the dynamics of wild-type A-site in Chapter 3. We are specifically interested in gaining insight into how the dynamic behavior of the internal loop adenines A92 and A93 is affected by the A08G mutation and how this in turn affects recognition of aminoglycosides. Comparison of these results with those obtained for the wild type A-site rRNA in Chapter 3 should provide a comprehensive and fundamental view of this critical conformational switch.

4.2 Material and Methods

4.2.1 NMR sample preparation

The mA-site rRNA samples used in the NMR studies were prepared by *in vitro* transcription using synthetic double stranded DNA templates that contained the T7 promoter and sequence of interest (Integrated DNA Technologies, Inc.), T7 RNA polymerase (Takara Mirus Bio, Inc.), and $^{13}C/^{15}N$ labeled NTPs (Silantes, Inc. and ISOTEC, Inc.). The RNA was purified by 20% (w/v) denaturing polyacrylamide gel electrophoresis containing 8M Urea and 1x TBE followed by electroelution in 20 mM Tris pH 8 buffer and ethanol precipitation. The RNA pellet was dissolved and exchanged into NMR buffer (15 mM sodium phosphate, 0.1 mM EDTA, and 25 mM NaCl at pH ~6.4) using 0.2 μM filter (Millipore Corp.). The final RNA concentrations were between 0.2 to 0.6 mM. Samples volumes of 250 to 300 μL were used for all the experiments.

The mA-site rRNA construct used in this study was derived from the *E.coli* ribosomal RNA sequence (*10*). This sequence consists of the minimal aminoglycoside-binding region that includes the conserved U-U base pair, internal loop adenines A92/A93 and the A08 to G substitution (Figure 4.1A, left). The second helix of this RNA was closed with a UUCG tetraloop (*10*). A GC base pair was added to helix II of this construct to add more measurements here as compared to helix I. In addition, helix I was extended by two GC base pairs to optimize the RNA synthesis by *in vitro* transcription.

The elongated mA-site rRNA samples were uniformly $^{13}C/^{15}N$ AU (EGC-A-site rRNA) or GC (EAU-A-site rRNA) labeled respectively to avoid spectral overcrowding due to the elongation residues. The elongation was achieved by extending the size of helix I by 22 NMR invisible Watson-Crick base pairs (Figure 4.2A).

4.2.2 NMR Spectroscopy Measurements

All NMR experiments were carried out on an Avance Bruker 600 MHz NMR spectrometer equipped with a triple-resonance 5-mm cryogenic probe at 298K. NMR spectra were processed using NMRPipe/NMRDraw (*11*), analyzed using NMRDraw or NMRView (*12*) and overlaid using Sparky 3 (*13*).

Paromomycin chemical shift titrations were performed on mA-site rRNA by recording 2D ^{13}C-^{1}H TROSY-HSQC spectra upon incremental additions of the drug. Spectra of mA-site rRNA (0.4 mM) were recorded with increments of 0.00, 0.10, 0.20, 0.30, 0.40, 0.80, 1.60, 4.00 and 10.00 mM paromomycin solution.

^{15}N spin relaxation was measured for guanine and uridine residues in both the non-elongated and elongated samples of mA-site. ^{15}N longitudinal (R_1) and transverse ($R_{2,CPMG}$) relaxation rates were measured using a combination of 2D (mA-site, EAU-mA-site) and 1D (EGC-mA-site) as described in section 3.2.2. The delays used are summarized on Tables 4.1.

Longitudinal (R_1) and rotating-frame ($R_{1\rho}$) relaxation rates were measured for mA-site rRNA (in the presence and absence of paromomycin), EAU-mA-site and EGC-mA-site rRNA samples as described in section 3.2.2. All the delays used in the R_1 and $R_{1\rho}$ experiments are summarized in Table 4.2. A 1D ^{13}C-Selective $R_{1\rho}$ experiment was used to collect $R_{1\rho}$ data for EGC-mA-site rRNA. This experiment was described in section 3.2.2. Four point relaxation profiles (including duplicates for error estimation) were collected for A92 (C2, C8), A93 (C2, C8), and A10 (C2). A spinlock power of 3.0 kHz and offset of 3.7 kHz were used for all the experiments. The delays used in the 1D ^{13}C Selective off-resonance $R_{1\rho}$ experiment are summarized in Table 4.3.

Table 4.1: Relaxation delays used in the carbon R_1 and $R_{2,CPMG}$ experiments for mA-site rRNA. Duplicate and quadruplicate measurements used to estimate error are indicated using "(x2)" and "(x4)" respectively.

Delays (ms) for G experiments		
	R_1	$R_{2,CPMG}$
mA-site rRNA	(x2)	(x2)
EAU-mA-site rRNA	(x4)	(x4)
Delays (ms) for U experiments		
	R_1	$R_{2,CPMG}$
mA-site rRNA	(x2)	(x2)
EGC-mA-site rRNA	(x2)	(x2)

Table 4.2: Relaxation delays used in the ^{13}C R_1 and $R_{1\rho}$ experiments for mA-siterRNA. Duplicate, triplicate or quadruplicate measurements used to estimate error are indicated by using "(x2)", "(x3)" and "(x4)" respectively.

Delays (ms) for R_1 experiment			
	C2, C6, and C8	C5	C1'
mA-site rRNA	20, 500 (x2)	20, 660 (x3)	20, 600 (x4)
EAU-mAsite rRNA	20, 600 (x4)	20, 600 (x4)	20, 1000 (x4)
EGC-mAiste rRNA	20, 500 (x2)		
Delays (ms) for $R_{1\rho}$ experiment			
	C2, C6, and C8	C5	C1'
mA-site rRNA	2, 25, 55 (x2)	4, 44 (x4)	4, 46 (x3)
EAU-mAsite rRNA	2, 15, 30 (x2)	2, 12, 22 (x2)	4, 24 (x2), 32 (x2)

Table 4.3: Relaxation delays used in the carbon $R_{1\rho}$ experiments for EGC-mA-site rRNA. Duplicate measurements used to estimate error are indicated using "(x2)".

Delays (ms) for $R_{1\rho}$ experiment		
	C2	C8
A92	0, 6, 14 (x2), 20	0, 4 (x2), 6, 10
A93	0, 4 (x2), 2, 6	0, 6, 14 (x2), 20
A10	0, 6, 14 (x2), 20	

A 1D ^{13}C-selective $R_{1\rho}$ relaxation experiment was used to measure slow motions (μs-ms) in mA-site rRNA in the absence and presence of paromomycin. This experiment was described in section 3.2.2. Four or seven point relaxation profiles (including duplicates for error estimation) were recorded per spinlock power. The spinlock powers used were 100, 200, 300, 400, 600, 800, 900, 1000, 1500, 2000, 2500, 3000, and 3500

Hz. The spinlock powers and offsets used for the off-resonance experiments were the same as the ones described before (section 3.2.2). The same delays were used for the on- and off-resonance experiments, respectively (tables 4.4 – 4.5).

Table 4.4: Relaxation delays used in the carbon $R_{1\rho}$ dispersion experiments for unbound mA-site rRNA. Duplicate measurements used to estimate error are indicated using "(x2)".

	Delays (ms) for $R_{1\rho}$ experiment		
	C2	C8	C1'
G08		0, 4, 8, 12 (x2), 16 (x2)	
A10	0, 2, 4, 12, 24, 36 (x2)		
A92	0, 4, 8, 12 (x2), 16 (x2)	0, 2, 4, 8, 16, 24, 30 (x2)	0, 6, 12, 24, 32, 40 (x2)
A93	0, 4, 6 (x2), 10, 16	0, 6, 12, 24, 32, 40 (x2)	0, 6, 12, 24, 32, 40 (x2)
G94		0, 2, 4, 12, 24, 36 (x2)	0, 2, 4, 8, 12, 24 (x2)

Table 4.5: Relaxation delays used in the carbon $R_{1\rho}$ dispersion experiments for mA-site rRNA 95% bound to paromomycin. Duplicate measurements used to estimate error are indicated using "(x2)".

	Delays (ms)	
	C2	C8
G08		
A92	0, 9 (x2), 18	
A93	0, 8 (x2), 16	0, 3, 6, 18 (x2)
A10	0, 10 (x2), 20	

4.2.3 Data Analysis

Apparent dissociation constants (K_d) for mA-site bound to paromomycin were obtained by fitting the observed chemical shift changes to the equation (*14*):

$$\delta_{obs} = \delta_{Free} + \frac{(\Delta\delta_T)\{([M]_T + [RNA]_T + K_d) - \sqrt{([M]_T + [RNA]_T + K_d)^2 + (4[M]_T[RNA]_T)}\}}{2[RNA]_T} \quad (4.1)$$

where $[M]_T$ is the total concentration of paromomycin, $[RNA]_T$ is the mA-site rRNA concentration based on UV absorbance at 260 nm, $\Delta\delta_T$ is the difference in chemical shifts between the "unbound" and "drug-bound" states (in ppm), δ_{obs} is the observed chemical shift (in ppm), and δ_{Free} is the chemical shift in the free state (in ppm). The data was fitted using the Origin software (OriginLab Corporation) in which $\Delta\delta_T$ and K_d were allowed to vary during the fit. The calculated apparent K_d was in good agreement with previously reported K_d for mA-site rRNA bound to paromomycin (*6*).

Changes in chemical shift were calculated using the equation $\Delta\delta = \sqrt{(\Delta\delta_H)^2 + (\alpha\Delta\delta_X)^2}$, where $\Delta\delta_H$ and $\Delta\delta_X$ are the changes in for hydrogen and carbon chemical shift, α is the ratio of ^1H and ^{13}C gyromagnetic ratio (*15*). All resonance intensities were measured using 2D TROSY-HSQC spectra as described in section 3.2.3. The normalization was carried out independently for mA-site (unbound and bound to paromomycin respectively), EAU-mA-site and EGC-mA-site rRNA samples.

All the ^{13}C and ^{15}N R_1 and R_2 values were obtained by non-linear least squares fitting the peak intensities to the mono-exponential function $I_{(t)} = I_{(0)}e^{(-R\times t)}$, based on the Levenberg-Marquardt (LM) algorithm. The data was fitted using the Origin software (OriginLab Corporation). The 2D ^{13}C R_1 and $R_{1\rho}$ data was fitted using in-house software (*16*). The final ^{13}C and ^{15}N R_2 values were corrected to account for the off-resonance effects according to the $R_{1\rho} = R_1 \cos^2\theta + R_2 \sin^2\theta$ equation, in which $\theta = \arctan(\omega_{SL}/\Omega)$ is the effective tilt angle of the spinlock field, ω_{SL} is the spinlock field power in Hz and Ω is the resonance offset from the spinlock carrier frequency in Hz. (*17*). Uncertainties were also obtained using duplicate, triplicate and quadruplicate relaxation measurements.

The relative order parameter (S^2_{rel}) values were estimated from the ratio of $2R_2$-R_1 measured for each residue to that of the largest value in the well-structured RNA helix (*18*). The $2R_2$-R_1 values are, to a good approximation, proportional to $S^2 \times J(0)$, where J(0) is the spectral density function at zero field and S^2 is an order parameter used to describe motions occurring at time scales faster than the overall tumbling. In addition, $2R_2$-R_1 values are independent of the time scale of the internal motions and the number of contributing relaxation mechanisms under the assumption that all the relaxation mechanisms experience similar amplitude of isotropic motions (*19*)(*18*)(*16*). The ^{13}C and ^{15}N R_1, R_2 and S^2_{rel} measurements for mA-site rRNA (in the absence and presence of paromomycin) and E-Asite rRNA are summarized in Appendix 2 (Tables A2.1 – A2.3).

The maximum efficiency of Hartman-Hahn transfers between spins was computed as described in section 3.2.3. Data with A_{HAHA} of >1% for the C2-C4 or C2-C6 couplings (J_{CC} = -1 Hz), C8-C5 couplings (J_{CC} = 1 Hz) and >0.1% for C8-C4 or C8-C6 couplings (J_{CC} = 10 Hz), C2-C5 couplings (J_{CC} = 11 Hz), C1'-C2' couplings (J_{CC} = 40 Hz) were excluded from the analysis (Tables A2.4 to A2.6) (*20*)(*21*).

The ^{13}C-selective relaxation data for mA-site rRNA (absence and presence of paromomycin) was analyzed as described in section 3.2.3. Only on-resonance $R_{1\rho}$ dispersion measurements were collected for mA-site rRNA in the presence of the drug. Off-resonance data was collected for G08 (C8), A10 (C2), A92 (C2, C8, C1'), G94 (C1') and A93 (C2, C8, C1'). Mono-exponential decays were observed for all the measured offset/power combinations. The on- and off-resonance data was fitted using a two-site chemical exchange expression derived using the Laguerre's method for polynomial root finding (Equation 1.3, described in section 3.2.3).

$$R_{1\rho} = R_{1\rho,\infty} + \frac{\sin^2\theta p_A p_B \Delta\omega^2 k_{ex}}{\frac{\omega_A^2\omega_B^2}{\omega_{eff}^2} + k_{ex} - \sin^2\theta p_A p_B \Delta\omega^2 k_{ex}\left(1 + \frac{2k_{ex}(p_A\omega_A^2 + p_B\omega_B^2)}{\omega_A^2\omega_B^2 + \omega_{eff}^2 k_{ex}^2}\right)} \quad (4.3)$$

All the analysis was performed using the Origin program (OriginLab Corporation) as described in section 3.2.3. The best-fit parameters were determined after an F-test statistics with a 99% confidence level (Table 4.5). The activation energies barriers and flipping out free Gibbs energy ($\Delta G_{flipping\ out}$) for unbound mA-site rRNA were calculated using the results from the chemical exchange experiments as described in section 3.2.3.

Table 4.6: Key statistics from chemical exchange for mA-site rRNA

Base	R_2	R_1	k_{ex} (s^{-1})	p_b	$\Delta\omega/2\pi$ (Hz)
G08C8	41 ± 1	2.1 ± 0.1			522 ± 13
A93C2	80 ± 2	1.6 ± 0.2			-944 ± 21
A92C2	68 ± 2	1.7 ± 0.2	13494 ± 355	(5.0 ± 0.2) x10^{-2}	-654 ± 18
A92C8	33 ± 1	2.4 ± 0.1			-299 ± 12
G94C1'	25 ± 2	2.0 ± 0.1			-503 ± 10
A93C1'	28 ± 0.4	2.0 ± 0.1	5636 ± 607	(1.1 ± 0.3) x10^{-2}	287 ± 51
A93C8	24 ± 0.1	2.0 ± 0.03	967 ± 318	(1.1 ± 0.2) x10^{-3}	-327 ± 57
A10C2	35 ± 0.1	2.0 ± 0.03			

4.3 Results

4.3.1 NMR resonance assignments of mA-site rRNA

The resonances of mA-site rRNA were assigned by comparing its spectra with those of wild-type A-site rRNA followed by conventional experiments to complete and conform assignments (Figure 4.1A). Our assignments were found to be in good agreement with previously reported assignments (*7*). The two constructs are identical except for substitution of internal loop A08 with G08. As expected, the spectra of mA-site rRNA overlaid very well with those of wild-type A-site rRNA with differences

primarily localized in and around the mutation site (Figure 4.1B-C). Interestingly, the mutation resulted in significant perturbations in the chemical shifts of residues A92 and A93. These perturbations are distinct from those observed with wild-type A-site upon binding to paromomycin for the C2/C8 base of A93/A92 and C1' sugar of A92. Small chemical shift perturbations are also observed for base pairs surrounding the internal loop and universally conserved UU base pair. These results suggest that A1408G mutation affects the structure-dynamic behavior of A92 and A93.

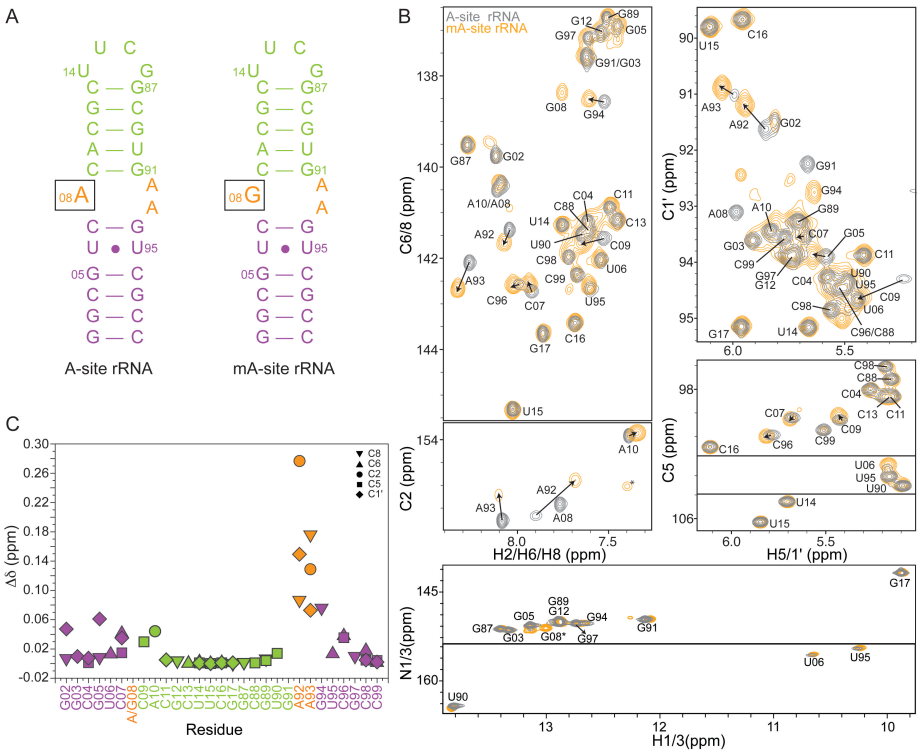

Figure 4.1: Comparison between mA-site and A-site rRNA resonance assignments. A) Secondary structure of A-site and mA-site rRNA. B) Overlay of 2D ^{13}C-^{1}H HSQC spectra of mA-site (orange) and A-site (black) rRNA. C) Change in chemical shift (Δδ) in ppm for mA-site and A-site rRNA. Shown are values for the C2 (circles), C5 (squares), C1' (diamonds), (C6 (triangle) and C8 (upside down triangle) resonances.

The resonances of the elongated constructs (EGC-mA-site rRNA and EAU-mA-site) (Figure 4.2A) could readily be assigned by overlaying their spectra with those of non-elongated mA-site rRNA (Figure 4.2B). As expected, minor differences in chemical shifts were observed for residues close to the elongation site (Figure 4.2B). Thus, elongation does not affect the structural or dynamic integrity of the mA-site rRNA. The effective preparation of these elongated samples establishes the general applicability of this strategy to study ps – ns motions.

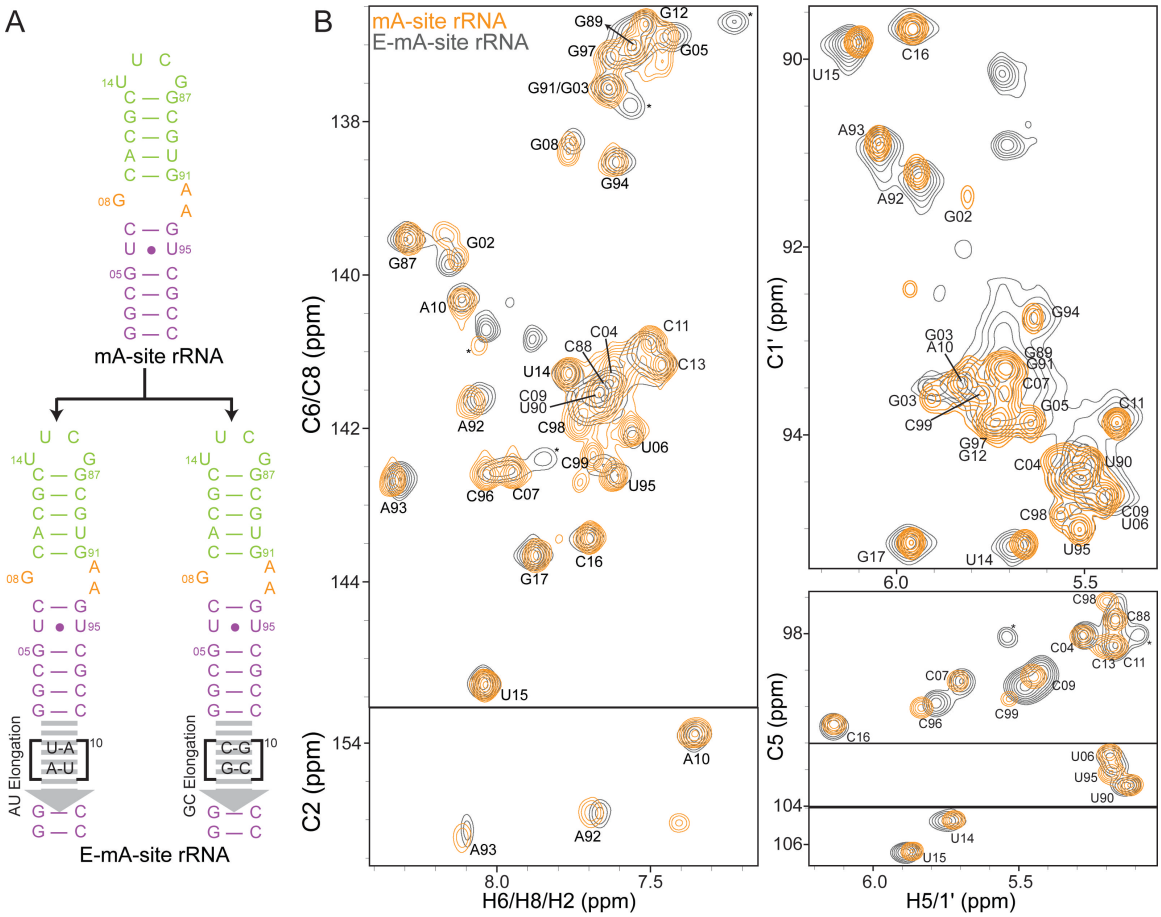

Figure 4.2: Resonance assignments of E-mA-site rRNA. A) Secondary structure of non-elongated (top) and elongated (bottom) mA-site rRNA. The purple (helix I), orange (internal loop), green (helix II), and gray (NMR invisible elongation site) represent different parts of the RNA. B) Overlay of 2D ^{13}C-^{1}H HSQC of E-mAsite rRNA (gray) and non-elongated mA-site rRNA (orange). The asterisks denote the resonances that correspond to the two GC base pairs added at the end of the elongation site.

4.3.2 Dynamics of unbound mutant A-site rRNA at the ps-ns time scale by spin relaxation

We used spin relaxation measurements to characterize the dynamic behavior of mA-site rRNA at fast ps – ns timescales. A simple way to directly compare the dynamic behavior of mA-site with that of wild-type A-site was to compare the normalized resonance intensities (*22*) measured in the elongated constructs; here, anomalously low intensities indicate presence of slow μs-ms motions whereas high intensities presence of fast ps – ns motions. This "dynamic fingerprinting" allowed us to establish the existence of differences in dynamics behavior before embarking on costly NMR experiments to completely characterize the dynamics of mA-site rRNA. This analysis revealed greater fast ps – ns motions in the sugars of A92 and A93 as well as in the base of A93 compared to A-site (Figure 4.3A). It is important to note that the sugar motions are not observed in short constructs likely because they occur at timescales comparable to overall tumbling. This together with the downfield chemical shift of A93C8 and A93C2 suggest that A93 adopts a partially looped out conformation as also observed in wild-type A-site RNA.

Next, we measured ^{15}N S^2_{rel} values for E-mA-site and compared them with those measured in E-A-site rRNA. Uniformly smaller ^{15}N S^2_{rel} values were measured for helix II as compared to the elongated helix I indicating the existence of inter-helical motions around the flexible internal loop as also observed in E-A-site RNA (Figure 4.3B). The magnitude of this attenuation is similar to that observed in wild-type E-A-site, indicating that both RNAs share similar inter-helical motional amplitudes. The anomalously high S^2_{rel} values measured for G08 and G91 can be attributed to presence of exchange

broadening and possibly to the unique of orientation of the ^{15}N – ^{1}H bond vector relative to the elongated axis (*16*)(*22*).

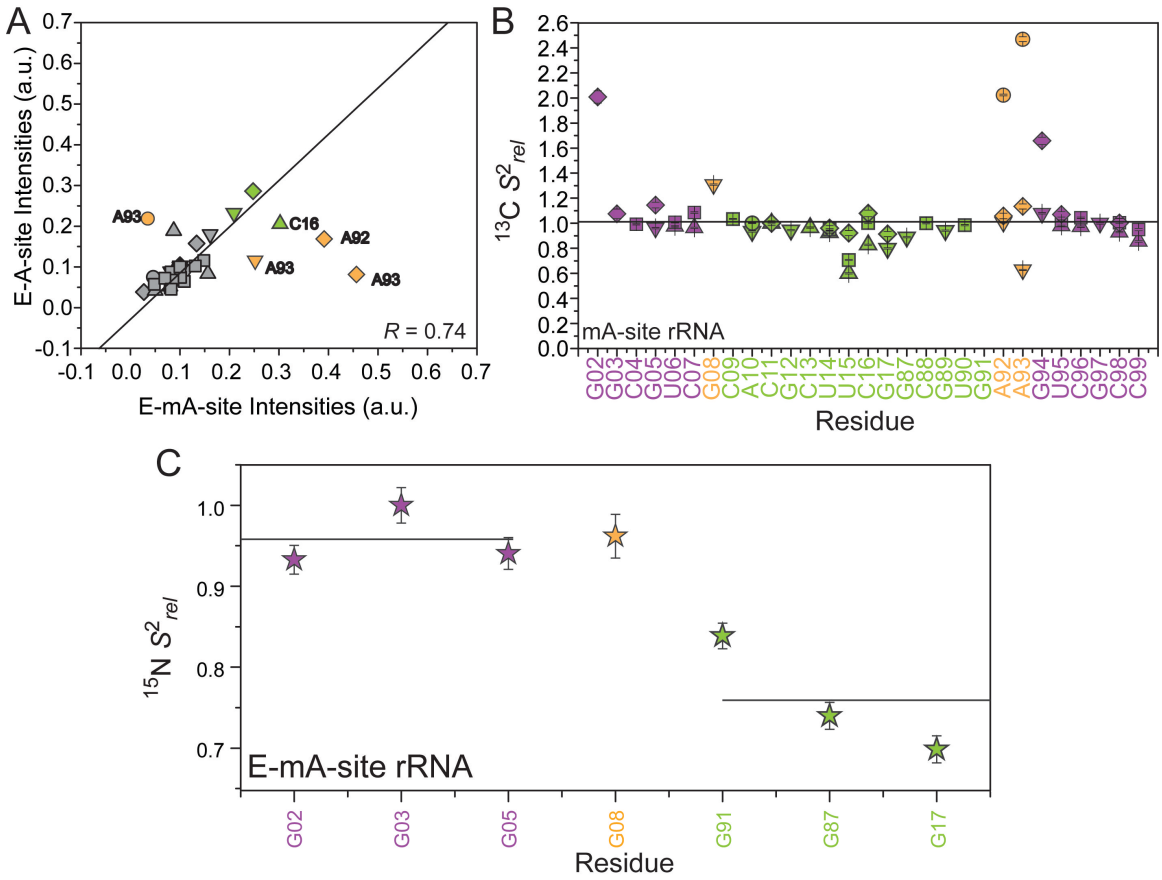

Figure 4.3:**Picosecond-nanosecond dynamics in unbound mA-site rRNA**. **(**A) Correlation plot of normalized intensities for elongated E-mA-site rRNA and E-A-site rRNA. Here, orange color values correspond to the internal loop. Qualitative order parameters (S^2_{rel}) are shown for non-elongate (B) and elongated (C) mA-site rRNAs. Shown are values for C1' (diamonds), C2 (circles), C5 (squares), C6 (triangles), C8 (upside down triangles), and N1 (stars).

Next, we measured longitudinal (R_1) and transverse (R_2) relaxation rates for the C2, C8, C5 nucleobases and C1' sugar in non-elongated mA-site rRNA and computed order parameters S^2_{rel} describing the amplitude of internal motions for each site (see section 4.2.3) (*18*)(*16*)(*19*). Comparison of the S^2_{rel} values revealed large differences specifically for the base moieties of A92 and A93, which could be attributed to

unsuppressed exchange broadening at these sites in mutant but not wild-type A-site. In addition, a greater degree of fast motions is observed for A93C8 in m-A-site compared to A-site. It is interesting that the base of A93 in m-A-site contains two sites (C2 and C8) that report on dynamics occurring at very different timescales (ps-ns versus μs-ms).

4.3.3 Microsecond-to-millisecond motions in mA-site rRNA by ^{13}C relaxation dispersion

We used $R_{1\rho}$ carbon dispersion relaxation experiments to characterize the dynamic behavior of mA-site at slow μs-ms timescales following the same procedure used to characterize the dynamic behavior of A-site in Chapter 3. These experiments revealed significant chemical exchange for G08C8, A92C2, A92C8, A93C2, G94C1', A93C8 and A93C1' (Figure 4.4). This can be compared to A-site in which significant exchange is observed for A08C2, A92C1' and A93C1'. Key statistics for this analysis are summarized in table 4.5. Thus, many more sites experience exchange broadening in m-A-site compared to A-site.

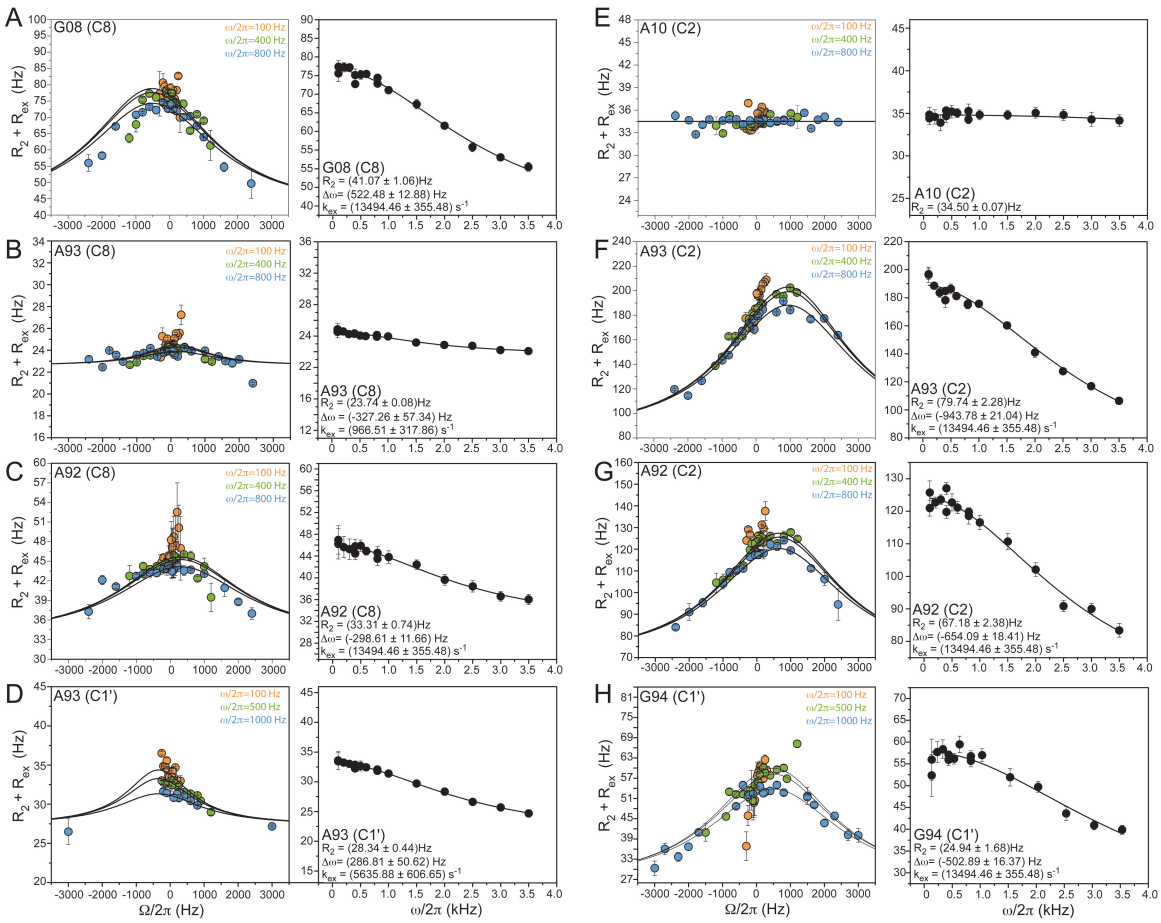

Figure 4.4: Chemical Exchange profiles for mA-site rRNA. Relaxation dispersion profiles are shown for: G08-C8 (A), A93-C8 (B), A92-C8 (C), A93-C1' (D), A10-C2 (E), A93-C2 (F), A92-C2 (G) and G94-C1' (H). The left panels show the offset (Ω/2π) and power (ω/2π) dependence of R_2 at spinlock powers of 100 (orange), 400 or 500 (green), 800 or 1000 (blue) Hz. The right panels show the on-resonance dependence of R_2

In both constructs, exchange is observed in the base of the 08 residues (G/A) and only in mA-site we observed significant exchange at G94C1'. Unlike A-site, the exchange observed in mA-site is not consistent with a single dynamic transition. Rather, the exchange rates measured for G08C8, A92C2, A92C8, A93C2, and G94C1' were significantly faster (65 – 100 μs) than those measured for either A93C8 (177 μs) and A93C1' (1 ms). This suggests three processes two of which are sensed by the base and sugar of A93. The G08C8, A92C2, A92C8, A93C2, G94C1' data could be fitted

simultaneously to a single process as determined from F-statistics with 99% confidence level yielding an exchange rate (k_{ex}) of 13494.46 ± 358.71 s^{-1} and a low populated "invisible state" of 4.95 ± 0.23%. However, the A93C8 and A93C1' exhibited different exchange rates that could not be fitted simultaneously. The k_{ex} for A93C8 is 5635.88 ± 606.65 s^{-1} and A93C1' is 966.57 ± 317.86 s^{-1}. Taken together, these data suggest that the dynamic μs – ms behavior of the A-site and mA-site rRNA are very different.

4.3.4 Conformational dynamics of mutant A-site bound to the aminoglycoside paromomycin

Previous studies have shown that binding of paromomycin does not significantly affect the conformation of G08, A92 and A93 (*8*)(*23*)(*6*). If the conformation of the internal loop hardly changes we would expect that motions experienced by unbound mA-site rRNA are scarcely affected upon drug binding. Here, we used NMR relaxation experiments to characterize the motions of mA-site rRNA bound to paromomycin.

Shown in Figure 4.4A is the 2D HSQC spectra of mA-site rRNA in the presence of paromomycin. Compared to A-site, the perturbations are much smaller though they are also localized in and around the internal loop, consistent with previous NMR studies (*7*). The chemical shift titration data was fitted to a two-state model yielding an apparent K_d ~0.76 ± 0.02 mM consistent with previously reported values (*7*). Based on this K_d, 95% of the RNA is bound to paromomycin. Furthermore, in stark contrast to A-site, addition of paromomycin had little to no effect on the internal loop resonance intensities, indicating that it does not affect motions at this site (Figure 4.5E).

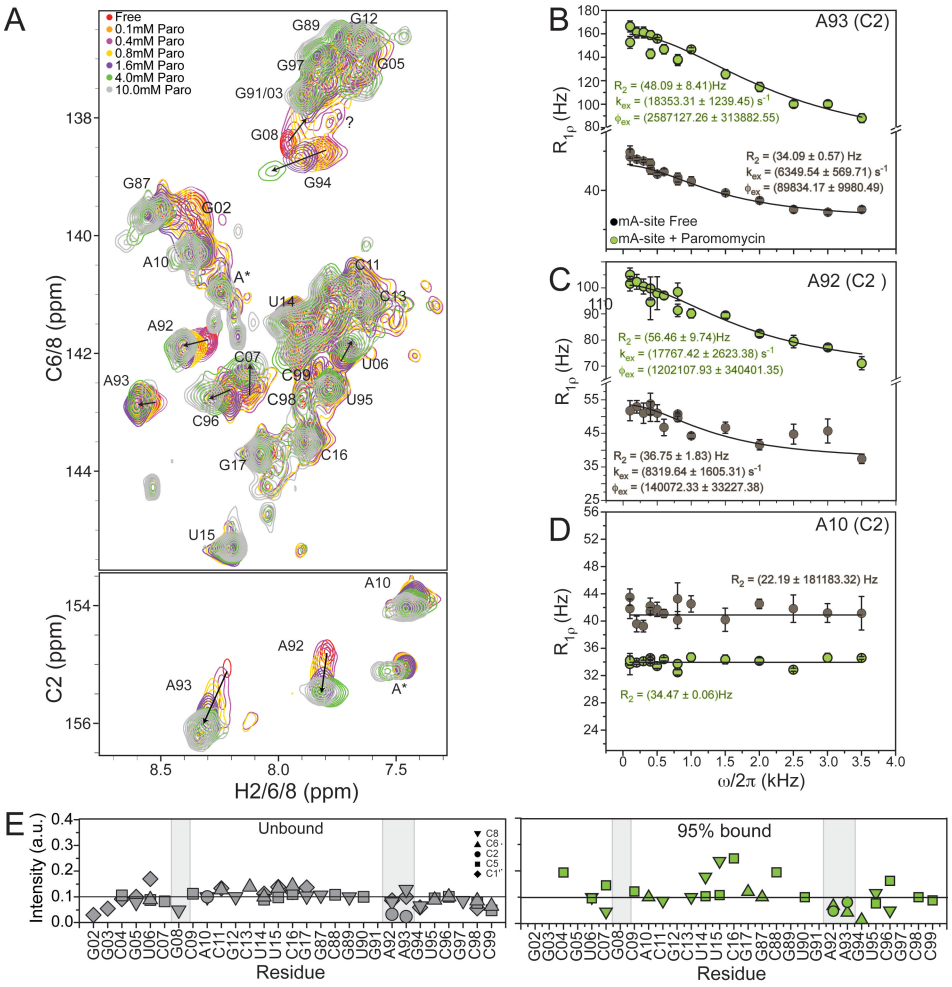

Figure 4.5: Dynamics of mA-site rRNA in the presence of paromomycin. A) 2D HSQC spectra of A-site rRNA in the presence of paromomycin. On-resonance dependence on $R_{1\rho}$ for: A93C2 (B), A92C2 (C) and A10C2 (D). E) Normalized resonance intensities for unbound and 95% bound mA-site rRNA. Shown are values for C1' (diamonds), C2 (circles), C5 (squares), C6 (triangles) and C8 (upside down triangles). D) Relaxation dispersion profiles for C2 in A10, A92 and A9

We performed carbon relaxation dispersion experiments for A10C2, A92C2, and A93C2 of mA-site rRNA under conditions where it is estimated to be 95% bound to paromomycin (Figure 4.5B-D). While the exchange was attenuated for A92C2 and A93C2 upon addition of paromomycin, significant exchange was observed in the 95% bound state. In addition, fitting the on-resonance carbon relaxation dispersion data to the fast exchange equation (see section 3.2.3 Equation 3.2) yielded an intrinsic R_2 value of

34.09 ± 0.57 Hz for A93C2 and 36.75 ± 1.83 Hz for A92C2. The lower intrinsic R_2 for A93C2 is indicative of this site being more flexible than A92C2 in the bound state as was the case in the wild-type A-site – paromomycin complex. These data shows that binding of paromomycin does not dramatically affect the motions of the internal loop (G08, A92 and A93). The complex is more dynamic in nature, which is consistent with MD simulations, that show flipping events for A92 and A93 in the presence of paromomycin (*9*).

4.3.5 Proposed model for the excited "invisible" state of mA-site rRNA

Our data clearly show that a single base substitution cause the dynamic behavior of mA-site to differ significantly from that of A-site over a range of timescales spanning picoseconds to milliseconds. How do the internal motions differ at the atomic level and what forces drive these differences? What is the excited "invisible" state sampled by m-A-site and how does it compare with the looped out state proposed for A-site?

We first note similarities between A-site and mA-site. In both cases, A93 is more flexible than A92 at ps-ns timescales, with the data generally being consistent with A93 adopting a partially looped out conformation and A92 adopting a more stacked looped in conformation. In general, we observe more extensive fast and slow motions in m-A-site, indicating that its internal loop structure is more disordered than A-site, consistent with previous NMR studies (*7*). The slower μs-ms motions also appear to be more highly complex for m-A-site rRNA. First, we observe exchange broadening for a larger number of sites, that include to residues outside the internal loop such as G94 C1'. Second, while a single concerted process can account for all the exchange observed in A-site, consistent

with a single concerted process, a total of three distinct processes with independent exchange rates are needed to account for the data measured in mA-site. In particular, we observe a concerted process for G08C8, A92C2, A92C8, A93C2, and G94C1' and two separate slower processes involving the base and sugar for A93. Thus, A93 alone reports on three distinct slow μs-ms processes while also undergoing fast motions in both it sugar and base moieties.

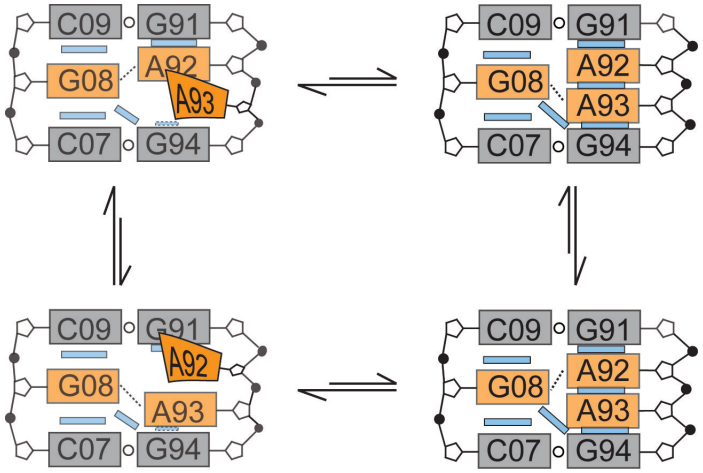

Figure 4.6: Proposed model for mA-site rRNA

The existence of three distinct processes and up to four distinct states clearly calls into question the validity of the exchange parameters obtained from our two-state analysis of the dispersion data. Unfortunately, fitting of the data to higher order models to accommodate four states is not presently feasible using state-of-the-art methods. In addition, the ability to fit a given site with a two-state process does not imply that the site does not sense other processes; rather, a good fit can be obtained when a given process dominates for example, because it leads to the largest chemical shift perturbations. Thus, we also cannot delineate all the residues that might be part of a given process. Notwithstanding the above limitations, the excited state chemical shifts of base carbons

C2 and C8 in A92 and A93 are upfield shifted relative to the ground state and is consistent with added stacking interactions. This suggests that in contrast to A-site, in which the excited state features looped out similar to the drug bound state, the excited state in m-A-site features greater stacking interactions.

While the above makes it difficult to propose specific structures for the excited states, it is useful to innumerate some possibilities. Our data suggests that the ground state features internal loop conformations in which A93 is flexible and partially looped out while A92 is more ordered and looped in. While previous NMR structures show that A93 base pairs with G08, our data suggests that the dominant base-pair alignment is most likely to involve A92. This is also consistent with fluorescence data that shows A92 to be stacked for unbound mA-site rRNA (*8*). Indeed, MD simulations show that either of A92 or A93 can base pair with G08 (*9*). Thus, other states likely include ones such as those observed in the NMR structure, in which A93 is base-paired with G08, and A92 is partially flipped out. Here the greater hydrogen bonding stability conferred by the G-A base pair compared to A-A base pairs serves to help equalize relative stabilities of these alternatives structures. Each of these two states can also potentially feature presences or absence of stacking interactions between A92 and A93 giving rise to a total of four states. We believe that the conformation in which both A92 and A93 are looped out is less likely considering the stability of the G-A base pair and the fact that such a state has not been observed for the mutant even when bound to drugs.

4.4 Conclusion

Our data shows that the single A08G substitution in the internal loop of A-site rRNA has a dramatic effect on the structural and motional features of the internal loop at timescales ranging from ps to ms. In A-site, the bases are floppy at ps-ns timescales, with A93 adopting a partially looped out conformation and A92 preferentially stacking on G91 owing to more favorable 5'-3' GA versus AG stacking (*24*). A single process towards an excited state is observed with many lines of evidence suggesting the excited state features looped out conformations for A92/A93 as observed in the drug bound state. The picture is far more complex in m-Asite rRNA. Again, we observe fast ps-ns mobility in A92 and A93 with A93 adopting a partially looped out conformation and A92 a partially looped in conformation. However, this mobility is greater in m-Asite compared to A-site. In addition, we observe exchange corresponding to up to three distinct processes and spanning a much larger of sites in the internal loop. This heterogeneity suggests that involvement of many states that likely feature distinct G08-A92/A93 hydrogen bonding interactions and/or A92/A93 stacking.

We attribute this greater heterogeneity observed in m-A-site to the greater stability conferred by the G-A base pair in comparison to the corresponding A-A base-pair in A-site. This serves to equalize the stability of having either A92 or A93 in a looped in state and base pairing with G08. This is supported by MD simulations in which both types of hydrogen bond alignments are observed (*9*). Furthermore, it is very likely that looping out both As is more energetically costly in mutant versus wild-type A-site because it requires the disruption of the G-A hydrogen bond alignment. The greater cost associated with disrupting the G-A base-pair may be one of the reasons why the A-site

does not adopt the conformation in which both As are looped out and this in turn may also contribute to lower binding affinities to the distinct structure.

Binding of paromomycin does not seem to affect the motions of mA-site rRNA. The fact that the intensities hardly changed, suggests that the internal loops dynamic behavior was not alter considerably. This is consistent with previous NMR studies and 2-aminopurine fluorescence data showed no significant changes on the RDC measurements of A92/A93 and not difference on the stacking propertied of A92 upon paromomycin binding (*8*)(*23*). The slow motions were attenuated but at 95% bound were still present in the internal loop. Binding of paromomycin does not lock the adenines in an extra-helical conformation consistent with the NMR structure of the mA-site – paromomycin complex (*6*). Hence, in the presence of the drug, the internal loop is still able to flip in/out (Figure 4.6B).

The idea was conceived by Casiano-Negroni, A and Al-Hashimi, H. M. The undergraduate student Gulati, N. synthesized the RNA. Casiano-Negroni, A. collected and analyzed the NMR data.

4.4 References

1. Recht, M. I., and Puglisi, J. D. (2001) Aminoglycoside resistance with homogeneous and heterogeneous populations of antibiotic-resistant ribosomes, *Antimicrobial Agents and Chemotherapy 45*, 2414-2419.
2. Hobbie, S. N., Pfister, P., Bruel, C., Sander, P., Francois, B., Westhof, E., and Bottger, E. C. (2006) Binding of neomycin-class aminoglycoside antibiotics to mutant ribosomes with alterations in the A site of 16S rRNA, *Antimicrobial agents and chemotherapy 50*, 1489-1496.
3. Recht, M. I., Douthwaite, S., Dahlquist, K. D., and Puglisi, J. D. (1999) Effect of Mutations in the A Site of 16 S rRNA on Aminoglycoside Antibiotic-Ribosome Interaction, *Journal of Molecular Biology 286*, 33-43.
4. Recht, M. I., Douthwaite, S., and Puglisi, J. D. (1999) Basis for prokaryotic specificity of action of aminoglycoside antibiotics, *The Embo Journal 18*, 3133-3138.

5. Prammananan, T., Sander, P., Brown, B. A., Frischkorn, K., Onyi, G.O., Zhang, Y., Bottger, E. C., Wallace, R. J. (1998) A single 16S ribosomal RNA substitution is responsible for resistance to amikacin and other 2-deoxystreptamine aminoglycosides in Mycobacterium abscessus and Mycobacterium chelonae, *The Journal of Infectious Diseases 177*, 1573-1581.
6. Lynch, S. R., and Puglisi, J. D. (2001) Structural origins of aminoglycoside specificity for prokaryotic ribosomes, *Journal of Molecular Biology 306*, 1037-1058.
7. Lynch, S. R., and Puglisi, J. D. (2001) Structure of a eukaryotic decoding region A-site RNA, *Journal of Molecular Biology 306*, 1023-1035.
8. Kaul, M., Barbieri, C. M., and Pilch, D. S. (2004) Fluorescence-based approach for detecting and characterizing antibiotic-induced conformational changes in ribosomal RNA: comparing aminoglycoside binding to prokaryotic and eukaryotic ribosomal RNA sequences, *Journal of the American Chemical Society 126*, 3447-3453.
9. Romanowska, J., Setny, P., and Trylska, J. (2008) Molecular dynamics study of the ribosomal A-site, *Journal of Physical Chemistry B 112*, 15227-15243.
10. Hermann, T. (2006) A-site model RNAs, *Biochimie 88*, 1021-1026.
11. Delaglio, F., Grzesiek, S., Vuister, G. W., Zhu, G., Pfeifer, J., and Bax, A. (1995) Nmrpipe - a Multidimensional Spectral Processing System Based On Unix Pipes, *Journal of Biomolecular Nmr 6*, 277-293.
12. Johnson, B. A., and Blevins, R. A. (1994) Nmr View - A Computer-Program For The Visualization And Analysis Of Nmr Data, *Journal Of Biomolecular Nmr 4*, 603-614.
13. Goddard, T. D. K., D.G. (2004) SPARKY 3, in *University of California, San Francisco*.
14. Gonzales, R. L., Jr.,, and Tinoco, I., Jr. (1999) Solution strucutre and thermodynamics of a divalent metal ion binding site in an RNA pseudoknot, *Journal of Molecular Biology 289*, 1267-1282.
15. Getz, M. M., Andrews, A. J., Fierke, C. A., and Al-Hashimi, H. M. (2007) Structural plasticity and Mg2+ binding properties of RNase P P4 from combined analysis of NMR residual dipolar couplings and motionally decoupled spin relaxation, *RNA 13*, 251-266.
16. Hansen, A. L., and Al-Hashimi, H.M. (2007) Dynamics of Large Elongated RNA by NMR Carbon Relaxation, *Journal of the American Chemical Society 129*, 16072-16082.
17. Yip, G. N., and Zuiderweg, E. R. (2004) A phase cycle scheme that significantly suppresses offset-dependent artifacts in the R2-CPMG 15N relaxation experiment, *J Magn Reson 171*, 25-36.
18. Dethoff, E. A., Hansen, A. L., Musselman, C., Watt, E. D., Andricioaei, and Al-Hashimi, H. M. (2008) Characterizing complex dynamics in the transactivation response element apical loop and motional correlations with the bulge by NMR, molecular dynamics, and mutagenesis, *Biophysics Journal 95*, 3906-3915.
19. Fushman, D., Tjandra, N., and Cowburn, D. (1999) An Approach to direct determination of protein dynamics from N-15 NMR relaxation at multiple fields,

independent of variable N-15 chemcial shift anisotropy and chemcial exchange controbutions., *Journal of the American Chemical Society 121*, 8577-8582.
20. Wijmenga, S. S., and van Buuren, B. N. M. (1998) The use of NMR methods for conformational studies of nucleic acids, *Progress in Nuclear Magnetic Resonance Spectroscopy 32*, 287-387.
21. Fiala, R., Munzarova, M.L., and Sklenar, V. (2004) Experiments for correlating quaternary carbons in RNA bases., *Journal of Biomolecular NMR 29*, 477-490.
22. Zhang, Q., Sun, X., Watt, E. D., and Al-Hashimi, H. M. (2006) Resolving the motional modes that code for RNA adaptation, *Science 311*, 653-656.
23. Lynch, S. R., and Puglisi, J. D. (2000) Application of residual dipolar coupling measurements to identify conformational changes in RNA induced by antibiotics, *J . Am. Chem. Soc 122*, 7853-7854.
24. Turner, D. H., and Sugimoto, N. (1988) RNA structure prediction, *Annu Rev Biophys Biophys Chem 17*, 167-192.

Chapter 5

Conclusion and future directions

5.1 Conclusion

In this thesis we characterized the structural and dynamical properties of two major RNA drug targets using different NMR experiments spanning the entire range of picosecond to millisecond timescales. We characterized global dynamics of HIV-1 TAR RNA occurring at the sub-millisecond timescales by RDC measurements (*1-3*). In addition, we used spin relaxation (*4*) and relaxation dispersion (*5, 6*) experiments to examine the local motions of A-site rRNA ranging from ps - ms timescales.

The global dynamics of HIV-1 TAR RNA and the impact of electrostatic interactions were studied using a combination of RDCs, chemical shift mapping upon metal (Na^+ and Mg^{2+}) binding and electrostatic calculations. The RDC measurements allowed the characterization of the global conformational dynamics of TAR in the

presence of Mg^{2+} and different concentrations of Na^{+}. Chemical shift mapping upon addition of metal ions provided information of the binding modes of these two metals. Our results showed a continuous reduction of inter-helical angle (from 46° to 22°), twist angle (from 66° to -18°) and RNA flexibility (measured by an increase in the internal generalized degree of order from 0.56 to 0.74) with increasing concentrations of Na^{+}. These results were in agreement with those observed for TAR in the presence of Mg^{2+} despite the difference binding modes of these two metal ions. These results suggested that Na^{+} and Mg^{2+} induces a similar structural and dynamical transition of TAR from a electrostatic relaxed bent and flexible state to a globally rigid coaxial state which has a stronger negative charge density and association with counterions. In addition, we found that the TAR inter-helical orientations that are stabilized by small molecules fall along the metal-induced conformational pathway.

The local dynamics of A-site rRNA and the impact of mutations in ligand binding were studied through a combination of spin relaxation, relaxation dispersion experiments and chemical shift mapping. Specifically, we were interested on understanding the motional modes governing the internal loop of A-site rRNA. Our results showed that a single mutation A08G has a dramatic effect on the motional modes of A-site rRNA and binding to paromomycin. In A-site rRNA we found that the internal loop bases A92/A93 undergo fast motions at ps – ns time scales. In addition, our data suggests that the internal loop of A-site is constantly exchanging between a ground state, where A92 is loop in and A93 is partially out the helix; and an "invisible" state where both adenines are partially loop out. The addition of the paromomycin then locks the adenines conformation outside the helix. However, the picture is more complicated for a version of A-site carrying the

A08G mutation. In this case, we observed fast motions in A92/A93 as well as exchange motions corresponding to three distinct processes. Binding of paromomycin to the mA-site rRNA do not seem to affect the motions present in the unbound form.

5.2 Future directions

An important next step will be to integrate our NMR data with computational MD simulations. Only then will it be possible to obtain a comprehensive atomic and energetic view of RNA dynamics and role of electrostatic and other interactions. A major weakness of our study is that RNA elements have to be taken outside their global context to carry out the NMR experiments. The design of experiments, such as foot printing, to probe the dynamics in more native contexts and link data to those observed by NMR is an important future goal. Finally, our results reveal that even on binding small molecules, RNA structure remains highly flexible. An important future goal will be to characterize this bound flexibility and its potential relationship to activity and drug design.

5.3 References

1. Kay, L. E. (2008) Using relaxation dispersion NMR spectroscopy to determine structures of excited, invisible protein states, *Journal of Biomolecular NMR 41*, 113-120.
2. Al-Hashimi, H. M., and Patel, D. J. (2002) Residual dipolar couplings: Synergy between NMR and structural genomics, *Journal of Biomolecular Nmr 22*, 1-8.
3. Getz, M. M., Andrews, A. J., Fierke, C. A., and Al-Hashimi, H. M. (2007) Structural plasticity and Mg2+ binding properties of RNase P P4 from combined analysis of NMR residual dipolar couplings and motionally decoupled spin relaxation, *RNA 13*, 251-266.
4. Palmer, A. G., 3rd. (2004) NMR characterization of the dynamics of biomacromolecules, *Chemical Reviews 104*, 3623-3640.

5. Vallurupalli, P., Hansen, D. F., and Kay, L. E. (2008) Structures of invisible, excited protein states by relaxation dispersion NMR spectroscopy *Proceedings National Academy of Science USA 105*, 11766-11771.
6. Hansen, A. L., Nikolova, E.N., Casiano-Negroni, A. and Al-Hashimi, H. M. (2009) Extending the range of microsecond-to-millisecond chemical exchange detected in labeled and unlabeled nucleic acids by selective carbon R(1rho) NMR spectroscopy., *Journal of the American Chemical Society 131*, 3818-3819.

Appendix 1

Summary of ^{13}C and ^{15}N relaxation measurements for A-site rRNA

1.1 Tables of ^{13}C relaxation measurements for A-site rRNA free and 95% bound to paromomycin. In addition, the data for the elongated A-site rRNA samples (EAU-A-site and EGC-A-site rRNA) is tabulated here.

Table A1.1: ^{13}C relaxation measurements (R_1, R_2 and S^2_{rel}) calculated for A-site rRNA.

Residue	Carbon Spin	R_1 (Hz)	R_2 (Hz)	S^2_{rel}
G02	C8	1.85 ± 0.03	36.15 ± 0.32	0.960 ± 0.06
	C1'	1.55 ± 0.10	36.63 ± 2.16	1.06 ± 0.016
G03	C1'	1.55 ± 0.07	27.47 ± 1.24	1.06 ± 0.025
C04	C5	2.16 ± 0.02	30.60± 0.05	0.989 ± 0.001
G05	C8	1.86 ± 0.02	37.11 ± 0.30	0.985 ± 0.006
U06	C6	2.28 ± 0.03	47.20 ± 0.34	1.00 ± 0.006
	C1'	1.46 ± 0.03	25.70 ± 0.61	0.994 ± 0.015
C07	C5	2.18 ± 0.05	30.70 ± 0.07	0.992 ± 0.002
	C6	2.25 ± 0.03	48.61 ± 0.37	1.032 ± 0.006
	C1'	1.50 ± 0.03	27.46 ± 0.70	1.06 ± 0.016
A08	C2	1.91 ± 0.02	34.43 ± 0.10	0.977 ± 0.005
	C1'	1.41 ± 0.03	30.23 ± 0.71	1.18 ± 0.015
C09	C5	2.13 ± 0.03	31.74 ± 0.06	1.03 ± 0.001
	C6	2.25 ± 0.03	48.59 ± 0.36	1.03 ± 0.006
	C1'	1.79 ± 0.26	34.09 ± 4.89	1.32 ± 0.074
A10	C2	1.82 ± 0.01	35.57 ± 0.12	1.00 ± 0.005
C11	C6	2.26 ± 0.02	47.11 ± 0.34	1.00 ± 0.006
	C1'	1.51 ± 0.02	25.88 ± 0.48	1.00 ± 0.013
G12	C8	1.87 ± 0.01	35.90 ± 0.28	0.952 ± 0.006
C13	C6	2.31 ± 0.02	47.77 ± 0.35	1.14 ± 0.006
U14	C5	2.19 ± 0.02	29.38 ± 0.12	0.947 ± 0.002
	C6	2.25 ± 0.01	45.90 ± 0.32	0.973 ± 0.006
	C1'	1.46 ± 0.02	23.55 ± 0.47	0.908 ± 0.014
U15	C5	1.84 ± 0.01	22.16 ± 0.09	0.711 ± 0.002
	C6	1.91 ± 0.02	29.28 ± 0.18	0.616 ± 0.006
	C1'	1.61 ± 0.02	21.15 ± 0.43	0.810 ± 0.014

C16	C5	1.99 ± 0.02	31.01 ± 0.06	1.00 ± 0.001
	C6	2.21 ± 0.02	40.60 ± 0.27	0.859 ± 0.006
	C1'	1.42 ± 0.03	26.45 ± 0.71	1.02 ± 0.017
G17	C8	1.73 ± 0.01	30.51 ± 0.19	0.807 ± 0.005
	C1'	1.57 ± 0.02	21.05 ± 0.39	0.807 ± 0.014
G87	C8	1.84 ± 0.01	35.07 ± 0.25	0.93 ± 0.01
C88	C5	2.23 ± 0.02	30.97 ± 0.05	1.00 ± 0.001
G89	C8	1.85 ± 0.01	36.01 ± 0.28	0.960 ± 0.005
U90	C5	2.14 ± 0.02	30.49 ± 0.10	0.985 ± 0.002
G91	C1'	1.47 ± 0.03	26.38 ± 0.63	1.02 ± 0.016
A92	C2	2.06 ± 0.03	35.42 ± 0.22	0.992 ± 0.006
	C8	1.96 ± 0.01	31.63 ± 0.21	0.835 ± 0.005
	C1'	1.73 ± 0.04	25.83 ± 0.72	0.994 ± 0.017
A93	C2	2.10 ± 0.01	25.30 ± 0.06	0.700 ± 0.005
	C8	2.05 ± 0.01	26.10 ± 0.17	0.683 ± 0.005
	C1'	1.80 ± 0.11	25.19 ± 2.19	0.967 ± 0.046
G94	C8	1.78 ± 0.02	40.05 ± 0.31	1.067 ± 0.006
U95	C5	2.12 ± 0.02	30.88 ± 0.10	0.998 ± 0.002
C96	C5	2.14 ± 0.05	31.69 ± 0.08	1.03 ± 0.001
	C6	2.19 ± 0.06	48.88 ± 0.47	1.039 ± 0.007
G97	C8	1.80 ± 0.01	37.61 ± 0.29	1.00 ± 0.006
C98	C5	2.15 ± 0.03	31.11 ± 0.05	1.01 ± 0.001
	C6	2.27 ± 0.03	47.20 ± 0.37	1.00 ± 0.006
	C1'	1.54 ± 0.07	20.76 ± 1.02	0.796 ± 0.027
C99	C5	2.27 ± 0.05	27.90 ± 0.09	0.896 ± 0.002
	C6	2.30 ± 0.06	45.15 ± 0.44	0.960 ± 0.007

Table A1.2: ^{13}C relaxation measurements (R_1, R_2 and S^2_{rel}) calculated for A-site rRNA 95% bound to paromomycin.

Residue	Carbon Spin	R_1 (Hz)	R_2 (Hz)	S^2_{rel}
C04	C5	2.38 ± 0.01	27.47 ± 0.20	0.881 ± 0.011
U06	C5	2.25 ± 0.04	27.63 ± 0.54	1.00 ± 0.015
	C6	2.21 ± 0.06	48.62 ± 0.79	0.999 ± 0.046
C07	C5	2.33 ± 0.05	29.87 ± 0.67	0.962 ± 0.016
	C6	2.21 ± 0.05	48.77 ± 0.65	1.00 ± 0.042
	C1'	1.19 ± 0.04	32.01 ± 2.76	1.00 ± 0.062
A08	C8	1.77 ± 0.04	40.30 ± 0.56	1.00 ± 0.030
	C1'	1.12 ± 0.06	38.33 ± 4.58	1.20 ± 0.075
C09	C5	2.57 ± 0.04	30.58 ± 0.59	0.981 ± 0.014
	C6	2.27 ± 0.05	46.64 ± 0.63	0.931 ± 0.042
	C1'	1.11 ± 0.05	38.58 ± 3.46	1.21 ± 0.063
A10	C2	1.75 ± 0.02	35.84 ± 0.24	1.00 ± 0.016
	C8	1.69 ± 0.03	38.10 ± 0.39	1.00 ± 0.025
C11	C1'	1.28 ± 0.03	28.65 ± 1.91	0.892 ± 0.056
C13	C6	2.19 ± 0.02	45.72 ± 0.37	0.947 ± 0.034
U14	C5	2.28 ± 0.01	25.93 ± 0.21	0.935 ± 0.011
	C6	2.19 ± 0.02	44.35 ± 0.33	0.919 ± 0.034
	C1'	1.25 ± 0.02	26.88 ± 0.98	0.836 ± 0.048
U15	C5	1.95 ± 0.01	19.24 ± 0.13	0.689 ± 0.011
	C6	1.80 ± 0.01	29.18 ± 0.19	0.736 ± 0.032
	C1'	1.38 ± 0.01	25.92 ± 0.76	0.803 ± 0.046
C16	C5	2.15 ± 0.02	27.24 ± 0.25	0.877 ± 0.011
	C6	2.11 ± 0.02	39.89 ± 0.29	0.858 ± 0.033
	C1'	1.24 ± 0.02	30.48 ± 1.11	0.951 ± 0.048
G17	C8	1.68 ± 0.01	30.25 ± 0.20	0.796 ± 0.021
	C1'	1.36 ± 0.01	25.00 ± 0.82	0.774 ± 0.047

G87	C8	1.75 ± 0.01	34.09 ± 0.25	0.864 ± 0.022
C88	C5	2.36 ± 0.01	25.99 ± 0.19	0.831 ± 0.011
U90	C5	2.39 ± 0.04	27.49 ± 0.63	0.992 ± 0.016
G91	C8	1.68 ± 0.03	39.25 ± 0.47	1.03 ± 0.027
A92	C2	1.93 ± 0.02	27.89 ± 0.14	0.707 ± 0.015
	C8	1.85 ± 0.02	28.43 ± 0.26	0.680 ± 0.024
A93	C2	1.91 ± 0.02	25.35 ± 0.12	0.648 ± 0.015
	C8	1.98 ± 0.02	25.90 ± 0.25	0.580 ± 0.026
	C1'	1.63 ± 0.04	35.34 ± 2.16	1.01 ± 0.054
U95	C5	2.32 ± 0.03	24.81 ± 0.37	0.893 ± 0.013
	C6	2.19 ± 0.05	47.14 ± 0.55	0.975 ± 0.039
C96	C5	2.31 ± 0.04	31.00 ± 0.61	1.00 ± 0.015
	C6	2.21 ± 0.05	47.85 ± 0.60	0.981 ± 0.040
C98	C5	2.32 ± 0.02	26.51 ± 0.27	0.849 ± 0.012
	C1'	1.20 ± 0.06	18.89 ± 4.04	582 ± 0.119
C99	C5	2.33 ± 0.06	24.95 ± 0.72	0.977 ± 0.018
	C6	2.26 ± 0.06	41.39 ± 0.62	0.832 ± 0.045

Table A1.3: ^{13}C relaxation measurements (R_1, R_2 and S^2_{rel}) calculated for EAU-A-site rRNA and EGC-A-site rRNA samples.

Residue	Carbon Spin	R_1 (Hz)	R_2 (Hz)	S^2_{rel}
G02	C8	1.31 ± 0.02	92.10 ± 2.18	0.794 ± 0.020
G03	C8	0.97 ± 0.02	115.61 ± 3.67	1.00 ± 0.022
C04	C5	1.95 ± 0.05	94.65 ± 1.68	0.816 ± 0.036
	C6	2.02 ± 0.03	111.49 ± 4.36	0.779 ± 0.042
G05	C8	0.98 ± 0.02	112.55 ± 3.02	0.973 ± 0.021
C07	C5	1.83 ± 0.14	112.23 ± 5.94	0.970 ± 0.044
	C6	1.58 ± 0.06	142.66 ± 10.51	1.00 ± 0.052
A08	C2	1.81 ± 0.18	186.37 ± 13.43	0.954 ± 0.059
C09	C5	1.78 ± 0.09	111.35 ± 4.19	0.962 ± 0.039
	C6	1.78 ± 0.04	153.31 ± 7.47	1.07 ± 0.044
A10	C2	1.32 ± 0.06	195.06 ± 18.01	1.00 ± 0.066
C11	C5	1.74 ± 0.09	116.03 ± 3.81	1.00 ± 0.038
	C6	1.75 ± 0.03	137.00 ± 5.14	0.960 ± 0.042
	C1'	1.43 ± 0.06	67.38 ± 3.45	0.959 ± 0.033
C13	C5	1.91 ± 0.07	102.46 ± 2.24	0.884 ± 0.036
	C6	1.96 ± 0.03	128.11 ± 4.53	0.896 ± 0.041
C16	C5	1.92 ± 0.94	97.75 ± 3.27	0.843 ± 0.038
	C6	1.95 ± 0.04	92.71 ± 3.75	0.647 ± 0.042
	C1'	1.29 ± 0.06	64.09 ± 4.41	0.912 ± 0.041
G17	C8	1.34 ± 0.01	71.12 ± 1.07	0.612 ± 0.017
	C1'	1.56 ± 0.04	55.16 ± 1.96	0.782 ± 0.028
G87	C8	1.38 ± 0.01	83.18 ± 1.54	0.717 ± 0.018
C88	C5	2.00 ± 0.054	99.76 ± 2.11	0.860 ± 0.036
G91	C8	1.25 ± 0.19	91.36 ± 2.50	0.788 ± 0.021
	C1'	1.48 ± 0.05	70.28 ± 2.89	1.00 ± 0.029
A92	C2	1.52 ± 0.18	119.04 ± 12.47	0.608 ± 0.070
	C8	1.24 ± 0.13	120.75 ± 6.46	
A93	C2	1.60 ± 0.05	100.92 ± 3.39	0.515 ± 0.049
	C8	1.55 ± 0.10	99.80 ± 4.58	
G94	C8	1.09 ± 0.02	101.22 ± 2.96	0.874 ± 0.021
C96	C5	1.85 ± 0.17	115.72 ± 7.89	1.00 ± 0.049
	C6	1.71 ± 0.01	139.71 ± 17.22	0.979 ± 0.072
C98	C5	1.74 ± 0.09	120.14 ± 3.99	1.04 ± 0.038
C99	C6	1.93 ± 0.10	145.65 ± 15.50	1.02 ± 0.065

1.2 Tables of the Hartmann Hahn efficiencies of bases A08, A92 and A93 for A-site rRNA.

Table A1.4: Hartman Hahn efficiencies calculated for the C2 spins of A08 and A10. Data points in bold were excluded from the analysis.

		A08			A10		
Offset (Hz)	Power (Hz)	A_{HAHA}-C4	A_{HAHA}-C5	A_{HAHA}-C6	A_{HAHA}-C4	A_{HAHA}-C5	A_{HAHA}-C6
0	100	0.0001	0.0001	0.0004	0.0001	0.0001	0.0001
0	200	0.0001	0.0001	0.0009	0.0002	0.0001	0.0002
0	300	0.0001	0.0001	0.0017	0.0003	0.0002	0.0003
0	400	0.0002	0.0002	0.0028	0.0004	0.0002	0.0005
0	500	0.0002	0.0002	0.0043	0.0006	0.0002	0.0008
0	600	0.0003	0.0002	0.0061	0.0008	0.0002	0.0011
0	700	0.0004	0.0002	0.0083	0.0011	0.0002	0.0014
0	800	0.0005	0.0002	0.0108	0.0014	0.0002	0.0018
0	900	0.0006	0.0002	0.0137	0.0017	0.0002	0.0023
0	1000	0.0007	0.0002	0.0168	0.0021	0.0003	0.0028
0	1500	0.0016	0.0003	0.0378	0.0046	0.0004	0.0062
0	2000	0.0029	0.0004	0.0672	0.0082	0.0005	0.0110
0	2500	0.0045	0.0006	0.1049	0.0128	0.0007	0.0171
0	3000	0.0064	0.0008	0.1510	0.0185	0.0009	0.0246
0	3500	0.0087	0.0010	0.2054	0.0252	0.0011	0.0335
300	100	0.0001	0.0004	0.0003	0.0002	0.0005	0.0029
250	100	0.0001	0.0004	0.0006	0.0002	0.0005	0.0001
200	100	0.0001	0.0004	0.1029	0.0002	0.0004	0.0000
150	100	0.0001	0.0004	0.0007	0.0002	0.0004	0.0000
100	100	0.0001	0.0003	0.0003	0.0002	0.0004	0.0000
75	100	0.0001	0.0003	0.0003	0.0002	0.0003	0.0000
50	100	0.0001	0.0002	0.0003	0.0002	0.0003	0.0001
25	100	0.0001	0.0002	0.0003	0.0001	0.0002	0.0001
-300	100	0.0000	0.0000	0.0007	0.0002	0.0000	0.0003
-250	100	0.0000	0.0000	0.0007	0.0000	0.0000	0.0003
-200	100	0.0000	0.0000	0.0007	0.0000	0.0000	0.0003
-150	100	0.0000	0.0000	0.0007	0.0000	0.0000	0.0003
-100	100	0.0000	0.0000	0.0006	0.0000	0.0000	0.0002
-75	100	0.0000	0.0000	0.0006	0.0000	0.0000	0.0002
-50	100	0.0000	0.0000	0.0006	0.0000	0.0000	0.0002
-25	100	0.0000	0.0001	0.0005	0.0001	0.0001	0.0002
1200	400	0.0001	0.0004	0.0007	0.0002	0.0005	0.0003
1000	400	0.0001	0.0004	0.0008	0.0002	0.0005	0.0003
800	400	0.0001	0.0004	0.0009	0.0003	0.0005	0.0004
600	400	0.0001	0.0004	0.0012	0.0003	0.0004	0.0006
400	400	0.0002	0.0004	0.0027	0.0003	0.0004	0.0034
200	400	0.0002	0.0003	**6.0573**	0.0003	0.0003	0.0024
150	400	0.0002	0.0003	0.0395	0.0003	0.0003	0.0013
100	400	0.0002	0.0002	0.0097	0.0003	0.0002	0.0008
50	400	0.0002	0.0002	0.0046	0.0004	0.0002	0.0006
-1200	400	0.0002	0.0000	0.0007	0.0003	0.0000	0.0003
-1000	400	0.0002	0.0000	0.0007	0.0003	0.0000	0.0003
-800	400	0.0002	0.0000	0.0007	0.0003	0.0000	0.0003
-600	400	0.0004	0.0000	0.0008	0.0005	0.0000	0.0003
-400	400	0.0091	0.0000	0.0009	0.0048	0.0000	0.0003
-200	400	0.0003	0.0001	0.0012	0.0014	0.0001	0.0004
-150	400	0.0002	0.0001	0.0014	0.0008	0.0001	0.0004
-100	400	0.0002	0.0001	0.0016	0.0006	0.0001	0.0004
-50	400	0.0002	0.0001	0.0021	0.0005	0.0001	0.0005

2400	800	0.0001	0.0005	0.0007	0.0002	0.0005	0.0003
2000	800	0.0001	0.0005	0.0008	0.0003	0.0005	0.0003
1800	800	0.0001	0.0005	0.0008	0.0003	0.0005	0.0003
1600	800	0.0002	0.0005	0.0009	0.0003	0.0005	0.0004
1000	800	0.0002	0.0004	0.0013	0.0003	0.0005	0.0006
800	800	0.0002	0.0004	0.0017	0.0003	0.0004	0.0009
600	800	0.0002	0.0004	0.0031	0.0004	0.0004	0.0020
400	800	0.0002	0.0003	0.0101	0.0005	0.0004	0.0179
200	800	0.0003	0.0003	**23.1877**	0.0007	0.0003	0.0125
250	800	0.0003	0.0003	**0.1367**	0.0006	0.0003	0.0418
100	800	0.0004	0.0002	0.0428	0.0009	0.0003	0.0036
50	800	0.0004	0.0002	0.0189	0.0011	0.0002	0.0024
-2400	800	0.0002	0.0008	0.0007	0.0003	0.0033	0.0003
-2000	800	0.0002	0.0001	0.0007	0.0003	0.0001	0.0003
-1800	800	0.0002	0.0001	0.0008	0.0003	0.0001	0.0003
-1600	800	0.0002	0.0000	0.0008	0.0003	0.0001	0.0003
-1000	800	0.0003	0.0000	0.0009	0.0005	0.0000	0.0004
-800	800	0.0006	0.0001	0.0011	0.0008	0.0001	0.0004
-600	800	0.0025	0.0001	0.0013	0.0020	0.0001	0.0004
-400	800	0.0609	0.0001	0.0018	0.0271	0.0001	0.0006
-200	800	0.0014	0.0001	0.0032	0.0073	0.0002	0.0008
-250	800	0.0021	0.0001	0.0026	0.0186	0.0001	0.0007
-100	800	0.0007	0.0002	0.0051	0.0025	0.0002	0.0011
-50	800	0.0006	0.0002	0.0071	0.0018	0.0002	0.0014

Table A1.5: Hartman Hahn efficiencies calculated for the C8 spins of A92 and G94. Data points in bold were excluded from the analysis.

		A92			G94		
Offset (Hz)	Power	A_{HAHA}-C4	A_{HAHA}-C5	A_{HAHA}-C6	A_{HAHA}-C4	A_{HAHA}-C5	A_{HAHA}-C6
0	100	0.0020	0.0000	0.0005	0.0000	0.0000	0.0002
0	200	0.0026	0.0000	0.0006	0.0003	0.0000	0.0003
0	300	0.0034	0.0000	0.0007	0.0000	0.0000	0.0003
0	400	0.0044	0.0000	0.0008	0.0021	0.0000	0.0003
0	500	0.0056	0.0000	0.0010	0.0006	0.0000	0.0003
0	600	0.0071	0.0000	0.0011	0.0031	0.0000	0.0004
0	700	0.0087	0.0000	0.0013	0.0033	0.0000	0.0004
0	800	0.0107	0.0000	0.0015	0.0020	0.0000	0.0005
0	900	0.0129	0.0000	0.0017	0.0028	0.0000	0.0005
0	1000	0.0153	0.0000	0.0019	0.0006	0.0000	0.0006
0	1500	0.0317	0.0000	0.0034	0.0025	0.0000	0.0009
0	2000	0.0550	0.0000	0.0054	0.0130	0.0000	0.0013
0	2500	0.0851	0.0000	0.0081	0.0180	0.0000	0.0019
0	3000	**0.1221**	0.0000	0.0114	0.0056	0.0001	0.0026
0	3500	**0.1659**	0.0001	0.0153	0.0088	0.0001	0.0034
300	100	0.0000	0.0000	0.0000	0.0014	0.0000	0.0000
250	100	0.0000	0.0000	0.0000	0.0031	0.0000	0.0000
200	100	0.0001	0.0000	0.0000	0.0015	0.0000	0.0000
150	100	0.0001	0.0000	0.0000	0.0032	0.0000	0.0000
100	100	0.0003	0.0000	0.0001	0.0000	0.0000	0.0000
75	100	0.0004	0.0000	0.0001	0.0004	0.0000	0.0000
50	100	0.0007	0.0000	0.0002	0.0025	0.0000	0.0001
25	100	0.0012	0.0000	0.0003	0.0018	0.0000	0.0001
-300	100	0.0057	0.0000	0.0017	0.0023	0.0000	0.0008
-250	100	0.0057	0.0000	0.0017	0.0004	0.0000	0.0008
-200	100	0.0055	0.0000	0.0016	0.0009	0.0000	0.0007
-150	100	0.0053	0.0000	0.0015	0.0002	0.0000	0.0007
-100	100	0.0048	0.0000	0.0014	0.0005	0.0000	0.0006

-75	100	0.0043	0.0000	0.0012	0.0018	0.0000	0.0005
-50	100	0.0036	0.0000	0.0010	0.0011	0.0000	0.0005
-25	100	0.0028	0.0000	0.0008	0.0007	0.0000	0.0003
1200	400	0.0038	0.0000	**0.7476**	0.0000	0.0000	0.0000
1000	400	0.0040	0.0000	0.0008	**0.5353**	0.0000	0.0000
800	400	0.0135	0.0000	0.0003	0.0001	0.0000	0.0000
600	400	0.0830	0.0000	0.0002	0.0105	0.0000	0.0000
400	400	0.0055	0.0000	0.0002	0.0074	0.0000	0.0001
200	400	0.0036	0.0000	0.0004	0.0005	0.0000	0.0001
150	400	0.0037	0.0000	0.0005	0.0005	0.0000	0.0002
100	400	0.0039	0.0000	0.0006	0.0032	0.0000	0.0002
50	400	0.0041	0.0000	0.0007	0.0000	0.0000	0.0003
-1200	400	0.0060	0.0000	0.0018	0.0000	0.0000	0.0008
-1000	400	0.0061	0.0000	0.0018	0.0023	0.0000	0.0008
-800	400	0.0061	0.0000	0.0018	0.0013	0.0000	0.0008
-600	400	0.0061	0.0000	0.0017	0.0000	0.0000	0.0008
-400	400	0.0060	0.0000	0.0016	0.0000	0.0000	0.0007
-200	400	0.0055	0.0000	0.0013	0.0010	0.0000	0.0005
-150	400	0.0053	0.0000	0.0012	0.0030	0.0000	0.0005
-100	400	0.0050	0.0000	0.0011	0.0001	0.0000	0.0004
-50	400	0.0047	0.0000	0.0010	0.0017	0.0000	0.0004
2400	800	0.0069	0.0000	0.0015	0.0006	0.0000	0.0003
2000	800	0.0074	0.0000	0.0013	0.0022	0.0000	0.0016
1800	800	0.0078	0.0000	0.0016	0.0011	0.0000	0.0504
1600	800	0.0084	0.0000	0.0027	0.0017	0.0000	0.0036
1000	800	0.0237	0.0000	0.0098	**1.7564**	0.0000	0.0003
800	800	**0.1113**	0.0000	0.0028	0.0509	0.0000	0.0002
600	800	**0.7198**	0.0000	0.0017	0.0163	0.0000	0.0002
400	800	0.0388	0.0000	0.0014	0.0041	0.0000	0.0003
200	800	0.0158	0.0000	0.0013	0.0024	0.0000	0.0004
250	800	0.0185	0.0000	0.0013	0.0010	0.0000	0.0003
100	800	0.0125	0.0000	0.0014	0.0045	0.0000	0.0004
50	800	0.0115	0.0000	0.0014	0.0049	0.0000	0.0004
-2400	800	0.0062	0.0000	0.0018	0.0000	0.0000	0.0008
-2000	800	0.0063	0.0000	0.0018	0.0001	0.0000	0.0008
-1800	800	0.0064	0.0000	0.0019	0.0024	0.0000	0.0008
-1600	800	0.0065	0.0009	0.0019	0.0025	0.0001	0.0008
-1000	800	0.0069	0.0000	0.0019	0.0008	0.0000	0.0008
-800	800	0.0072	0.0000	0.0019	0.0013	0.0000	0.0008
-600	800	0.0075	0.0000	0.0018	0.0008	0.0000	0.0007
-400	800	0.0080	0.0000	0.0017	0.0001	0.0000	0.0007
-200	800	0.0089	0.0000	0.0016	0.0000	0.0000	0.0006
-250	800	0.0086	0.0000	0.0017	0.0013	0.0000	0.0006
-100	800	0.0096	0.0000	0.0015	0.0044	0.0000	0.0005
-50	800	0.0101	0.0000	0.0015	0.0002	0.0000	0.0005

Table A1.6: Hartman Hahn efficiencies calculated for the C1' spins of A92 and A93. Data points in bold were excluded from the analysis.

Offset (Hz)	Power (Hz)	A92 A_{HAHA}-C2'	A93 A_{HAHA}-C2'
0	100	0.0100	0.0113
0	200	0.0119	0.0136
0	300	0.0142	0.0163
0	400	0.0167	0.0195
0	500	0.0196	0.0230
0	600	0.0230	0.0271
0	700	0.0267	0.0317

0	800	0.0308	0.0369
0	900	0.0355	0.0426
0	1000	0.0406	0.0490
0	1500	0.0737	**0.0906**
0	2000	**0.1205**	**0.1494**
0	2500	**0.1814**	**0.2260**
0	3000	**0.2564**	**0.3203**
0	3500	**0.3455**	**0.4322**
300	100	0.0325	0.0365
250	100	0.0320	0.0359
200	100	0.0312	0.0350
150	100	0.0295	0.0331
100	100	0.0261	0.0294
75	100	0.0233	0.0263
50	100	0.0195	0.0220
25	100	0.0148	0.0167
-300	100	0.0001	0.0001
-250	100	0.0001	0.0001
-200	100	0.0002	0.0003
-150	100	0.0004	0.0005
-100	100	0.0011	0.0013
-75	100	0.0019	0.0022
-50	100	0.0034	0.0039
-25	100	0.0061	0.0069
1500	500	0.0343	0.0385
1200	500	0.0344	0.0386
900	500	0.0342	0.0385
800	500	0.0340	0.0383
600	500	0.0332	0.0376
400	500	0.0312	0.0354
250	500	0.0281	0.0322
200	500	0.0267	0.0307
100	500	0.0234	0.0271
50	500	0.0215	0.0251
-1500	500	0.0131	0.0145
-1200	500	**0.1319**	0.0689
-900	500	0.0420	**0.1040**
-800	500	0.0206	0.0375
-600	500	0.0108	0.0155
-400	500	0.0100	0.0129
-250	500	0.0120	0.0148
-200	500	0.0131	0.0160
-100	500	0.0161	0.0191
-50	500	0.0178	0.0210
3000	1000	0.0352	0.0396
2700	1000	0.0355	0.0399
2300	1000	0.0359	0.0404
2000	1000	0.0364	0.0409
1700	1000	0.0369	0.0416
1500	1000	0.0373	0.0421
800	1000	0.0387	0.0442
600	1000	0.0390	0.0449
400	1000	0.0392	0.0456
250	1000	0.0394	0.0463
200	1000	0.0395	0.0466
100	1000	0.0399	0.0476
50	1000	0.0401	0.0482
-3000	1000	0.0387	0.0438
-2700	1000	0.0391	0.0448

-2300	1000	0.0398	0.0464
-2000	1000	0.0437	0.0505
-1700	1000	0.0628	0.0675
-1500	1000	**0.1118**	**0.1076**
-800	1000	**0.1946**	**0.3531**
-600	1000	0.0826	**0.1203**
-400	1000	0.0540	0.0714
-250	1000	0.0457	0.0578
-200	1000	0.0441	0.0551
-100	1000	0.0418	0.0514
-50	1000	0.0411	0.0500
1000	1000	0.0383	0.0436

1.3 Mono-exponential decays of the ^{13}C dispersion data for A-site rRNA.

Figure A1.1: Typical mono-exponential decays for C1' spin of A92 at different offsets and spinlock powers. Indicated in the frames are the offsets ($\Omega/2\pi$), spinlock powers ($\omega_1/2\pi$) and the maximum calculated A_{HAHA} (%).

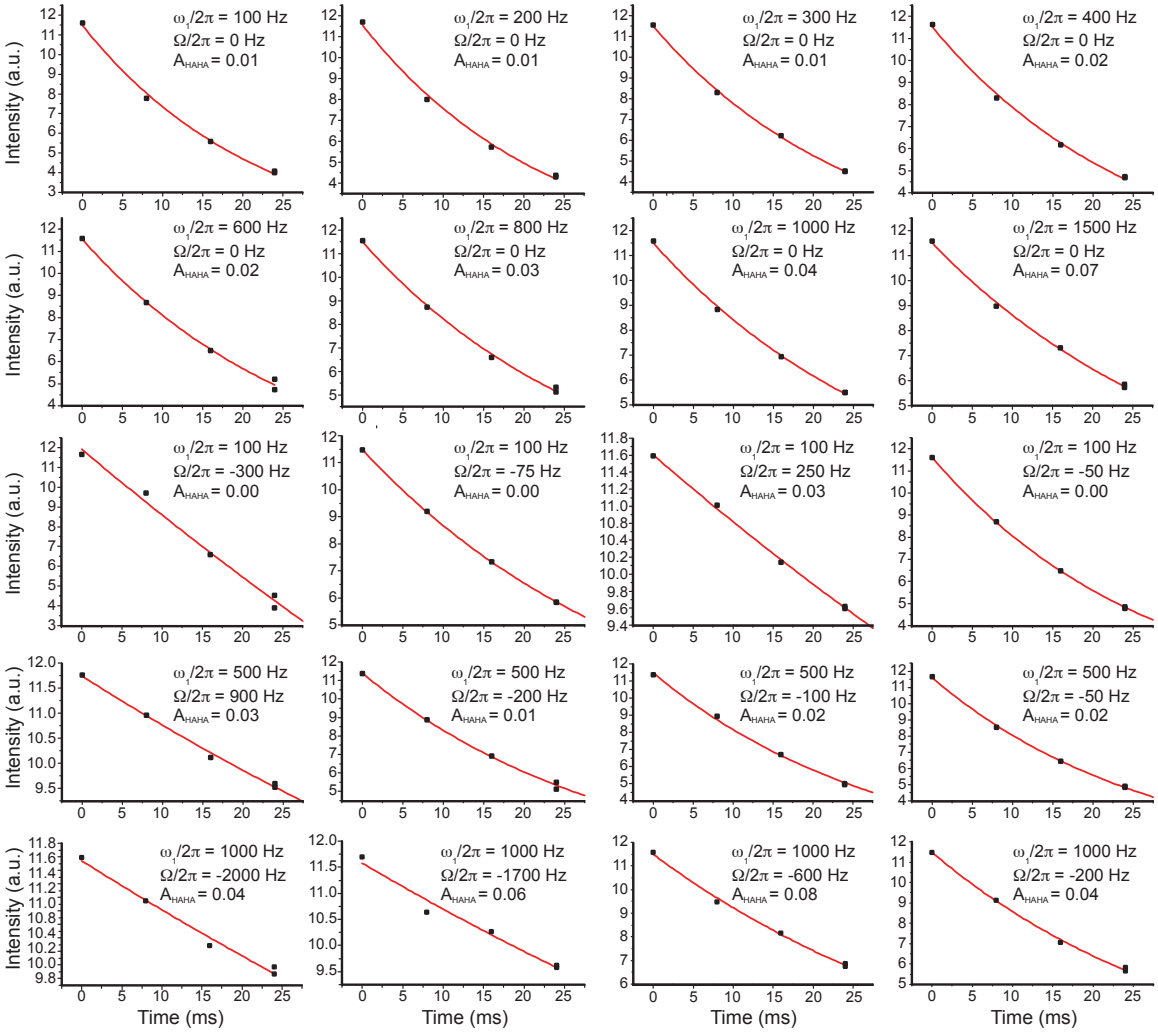

Figure A1.2: Typical mono-exponential decays for A10-C2, A93-C8 and A93-C1' of A-site rRNA-paromomycin complex at different spinlock powers ($\omega_1/2\pi$).

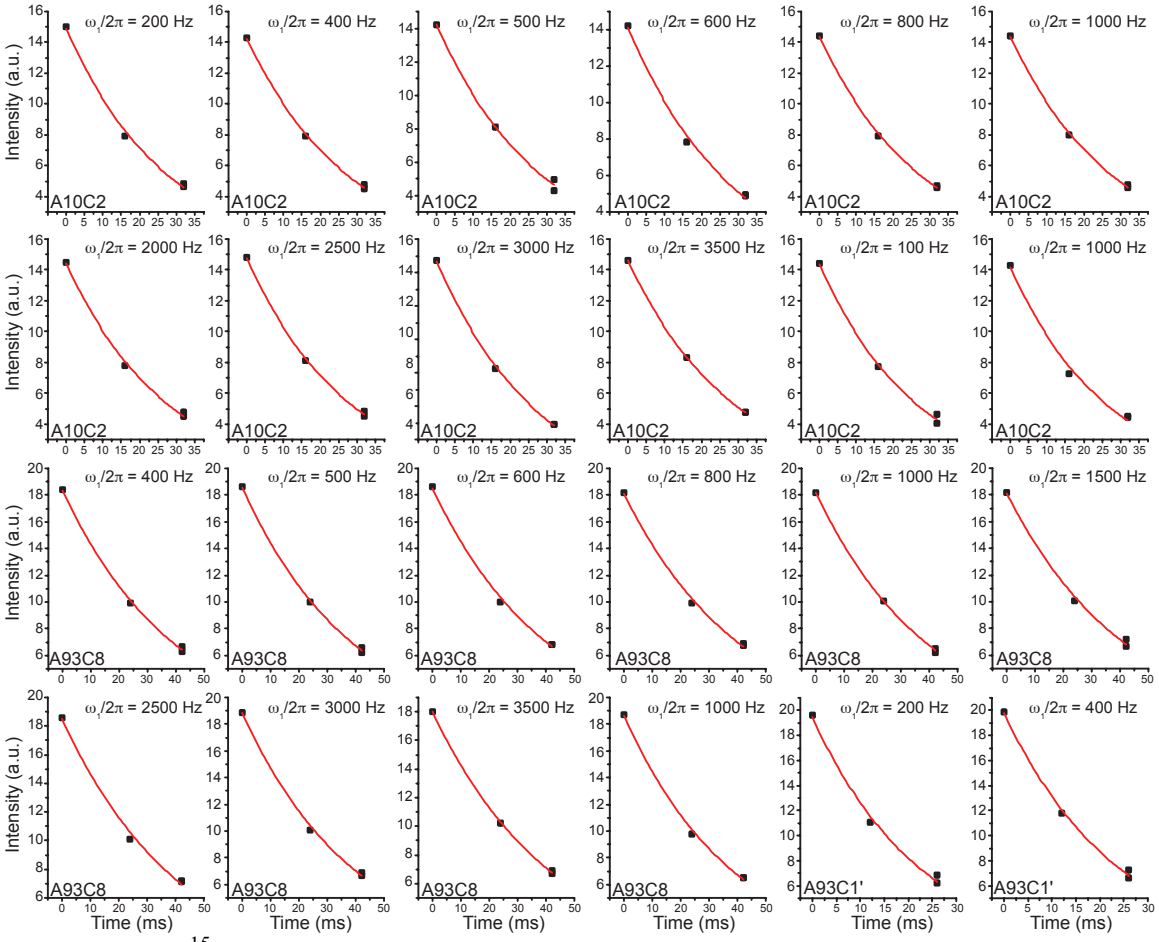

1.4 Tables of ^{15}N relaxation measurements for non-elongated and elongated A-site

Table A1.7: ^{15}N relaxation measurements calculated EAU-A-site and EGC-A-site rRNA samples.

		EAU-A-site rRNA and EGC-A-site rRNA		
Residue	Nitrogen	R_1 (Hz)	R_2 (Hz)	S^2_{rel}
G02	N1	0.875 ± 0.012	24.86 ± 0.23	0.95±0.01
G03	N1	0.845 ± 0.008	25.89 ± 0.50	0.99±0.02
G05	N1	0.915 ± 0.018	26.22 ± 0.60	1.00±0.02
G17	N1	1.118 ± 0.009	19.54 ± 0.11	0.74±0.01
G87	N1	1.023 ± 0.023	19.50 ± 0.12	0.74±0.01
U90	N3	0.795 ± 0.011	15.52 ± 1.08	
G91	N1	0.958 ± 0.014	24.49 ± 0.78	0.93±0.02

Appendix 2

Summary of ^{13}C and ^{15}N relaxation measurements for mA-site rRNA

1.1 Tables of ^{13}C relaxation measurements for mA-site rRNA free and 95% bound to paromomycin. In addition, the data for the elongated mA-site rRNA samples (EAU-mA-site and EGC-mA-site rRNA) is tabulated here.

Table A2.1: ^{13}C relaxation measurements (R_1, R_2 and S^2_{rel}) calculated for mA-site rRNA.

Residue	Carbon Spins	R_1 (Hz)	R_2 (Hz)	S^2_{rel}
G02	C8	1.71 ± 0.04	35 ± 0.32	0.90 ± 0.01
	C1'	1.49 ± 0.10	49 ± 5	2.01 ± 0.05
G03	C1'	1.43 ± 0.05	26 ± 2	1.08 ± 0.04
C04	C5	2.14 ± 0.02	31 ± 0.2	0.91 ± 0.01
G05	C8	1.72 ± 0.02	37 ± 0.3	0.96 ± 0.01
	C1'	1.29 ± 0.02	28 ± 1	1.15 ± 0.02
U06	C5	2.12 ± 0.02	31 ± 0.2	0.93 ± 0.01
	C6	2.19 ± 0.03	48 ± 0.3	0.98 ± 0.01
C07	C5	2.15 ± 0.03	33 ± 0.4	1.00 ± 0.01
	C6	2.06 ± 0.03	48 ± 0.3	0.96 ± 0.01
G08	C8	1.70 ± 0.03	51 ± 0.4	1.31 ± 0.01
C09	C5	2.12 ± 0.02	32 ± 0.2	0.95 ± 0.01
A10	C2	1.72 ± 0.02	36 ± 0.1	1.00 ± 0.002
	C8	1.69 ± 0.02	36 ± 0.3	0.93 ± 0.01
C11	C6	2.14 ± 0.03	49 ± 0.4	1.00 ± 0.01
	C1'	1.44 ± 0.01	25 ± 0.7	1.00 ± 0.02
G12	C8	1.76 ± 0.01	37 ± 0.3	0.94 ± 0.01
C13	C6	2.19 ± 0.03	48 ± 0.3	0.97 ± 0.01
U14	C5	2.20 ± 0.02	29 ± 0.2	0.88 ± 0.01
	C6	2.11 ± 0.02	46 ± 0.3	0.93 ± 0.01
	C1'	1.45 ± 0.02	24 ± 0.7	0.96 ± 0.02
U15	C5	1.84 ± 0.01	22 ± 0.2	0.65 ± 0.01
	C6	1.80 ± 0.02	30 ± 0.2	0.60 ± 0.004
	C1'	1.57 ± 0.02	23 ± 0.7	0.92 ± 0.02
C16	C5	1.99 ± 0.02	31 ± 0.2	0.92 ± 0.01
	C6	2.03 ± 0.02	41 ± 0.3	0.83 ± 0.01
	C1'	1.37 ± 0.03	26 ± 1	1.08 ± 0.03
G17	C8	1.66 ± 0.01	31 ± 0.2	0.80 ± 0.01
	C1'	1.53 ± 0.02	23 ± 0.7	0.91 ± 0.02
G87	C8	1.73 ± 0.01	35 ± 0.2	0.89 ± 0.01
C88	C5	2.20 ± 0.02	31 ± 0.2	0.92 ± 0.01
G89	C8	1.74 ± 0.01	37 ± 0.3	0.94 ± 0.01
U90	C5	2.16 ± 0.02	30 ± 0.2	0.91 ± 0.01
A92	C2	1.78 ± 0.07	72 ± 1	2.02 ± 0.01

	C8	1.76 ± 0.02	39 ± 0.3	1.01 ± 0.01
	C1'	1.68 ± 0.03	26 ± 0.9	1.06 ± 0.02
A93	C2	1.88 ± 0.14	87 ± 3	2.47 ± 0.02
	C8	1.95 ± 0.01	25 ± 0.2	0.63 ± 0.01
	C1'	1.94 ± 0.02	28 ± 0.8	1.13 ± 0.02
G94	C8	1.68 ± 0.02	42 ± 0.3	1.08 ± 0.01
	C1'	1.49 ± 0.04	40 ± 2	1.66 ± 0.03
U95	C5	2.08 ± 0.02	32 ± 0.2	0.94 ± 0.01
	C6	2.14 ± 0.03	48 ± 0.3	0.98 ± 0.01
	C1'	1.31 ± 0.02	26 ± 0.8	1.08 ± 0.02
C96	C5	2.13 ± 0.02	32 ±0.3	0.96 ± 0.01
	C6	2.11 ± 0.03	48 ± 0.4	0.97 ± 0.01
G97	C8	1.71 ± 0.01	39 ± 0.3	1.00 ± 0.01
C98	C5	2.13 ± 0.02	31 ± 0.2	0.93 ± 0.01
	C6	2.14 ± 0.03	46 ± 0.4	0.93 ± 0.01
	C1'	1.40 ± 0.04	25 ± 2	1.00 ± 0.04
C99	C5	2.16 ± 0.06	29 ± 0.5	0.88 ± 0.01
	C6	2.09 ± 0.06	42 ± 0.4	0.86 ± 0.01

Table A2.2: ^{13}C relaxation measurements (R_1, R_2 and S^2_{rel}) calculated for mA-site rRNA 95% bound to paromomycin.

Residue	Carbon Spins	R_1 (Hz)	R_2 (Hz)	S^2_{rel}
U06	C6	1.62 ± 0.11	76 ± 2	0.93 ± 0.01
A10	C2	1.26 ± 0.05	57 ± 1	1.00 ± 0.01
C11	C6	1.93 ± 0.07	81 ± 1	1.00 ± 0.01
U15	C6	1.71 ± 0.04	47 ± 0.5	0.57 ± 0.01
G17	C8	0.68 ± 0.11	15 ± 1	0.26 ± 0.04
G87	C8	1.40 ± 0.03	57 ± 1	1.00 ± 0.01
G89	C8	1.29 ± 0.04	60 ± 1	1.04 ± 0.01
A92	C2	1.49 ± 0.08	57 ± 1	0.99 ± 0.01
	C8	1.31 ± 0.06	61 ± 1	1.07 ± 0.01
A93	C2	1.47 ± 0.03	17 ± 0.2	0.29 ± 0.01

Table A2.3: ^{13}C relaxation measurements (R_1, R_2 and S^2_{rel}) calculated for EAU-mA-site rRNA and EGC-mA-site rRNA samples.

Residue	Carbon Spins	R_1 (Hz)	R_2 (Hz)	S^2_{rel}
G03	C8	0.97 ± 0.03	125 ± 2	1.00 ± 0.01
C04	C5	2.06 ± 0.03	107 ± 1	0.77 ± 0.01
G05	C8	1.01 ± 0.02	119 ± 2	0.94 ± 0.01
C07	C5	1.87 ± 0.05	122 ± 2	0.89 ± 0.01
	C6	1.63 ± 0.06	152 ± 5	1.00 ± 0.02
G08	C8	1.08 ± 0.04	114 ± 3	0.90 ± 0.01
C09	C5	1.95 ± 0.04	122 ± 2	0.88 ± 0.01
A10	C2	1.17 ± 0.04	118 ± 4	1.00 ± 0.02
C11	C5	1.91 ± 0.03	119 ± 2	0.86 ± 0.01
	C6	1.71 ± 0.04	146 ± 3	0.96 ± 0.02
	C1'	1.30 ± 0.07	69 ± 12	0.86 ± 0.15
C13	C5	1.73 ± 0.05	129 ± 2	0.93 ± 0.01
	C6	1.95 ± 0.04	125 ± 2	0.82 ± 0.02
C16	C5	1.96 ± 0.05	104 ± 2	0.75 ± 0.01
	C6	1.94 ± 0.05	106 ± 2	0.70 ± 0.02
	C1'	1.27 ± 0.10	71 ± 18	0.89 ± 0.02
G17	C8	1.34 ± 0.01	77 ± 1	0.61 ± 0.01
	C1'	1.49 ± 0.07	55 ± 8	0.68 ± 0.14

G87	C8	1.38±0.01	94.04±1.16	0.75±0.01
C88	C5	1.91±0.03	109.13±1.36	0.79±0.01
G91	C8	1.24±0.02	103.33±1.45	0.82±0.01
A92	C2	1.32±0.11	130.37±4.68	1.10±0.02
	C8	1.40±0.05	92.10±2.38	
A93	C2	1.47±0.18	99.43±8.06	0.83±0.04
	C8	1.65±0.02	64.00±1.32	
G94	C8	1.05±0.02	114.68±1.80	0.91±0.01
C96	C5	1.91±0.05	128.24±2.29	0.93±0.01
	C6	1.61±0.06	145.11±4.16	0.96±0.02
C98	C5	1.69±0.05	137.79±2.44	1.00±0.01
C99	C5	1.86±0.03	127.16±1.69	0.92±0.01
	C6	2.08±0.10	145.24±6.08	0.5±0.03

1.2 Tables of the Hartmann Hahn efficiencies of bases G08, A92, A93, A10 and G94 for mA-site rRNA.

Table A2.4: Hartman Hahn efficiencies calculated for the C2 spins of A10, A92 and A93. Data points in bold were excluded from the analysis.

		A10			A92			A93		
Offset (Hz)	Power (Hz)	A_{HAHA}-C4	A_{HAHA}-C5	A_{HAHA}-C6	A_{HAHA}-C4	A_{HAHA}-C5	A_{HAHA}-C6	A_{HAHA}-C4	A_{HAHA}-C5	A_{HAHA}-C6
0	100	0.0093	0.0002	0.0000	0.0028	0.0002	0.0001	0.0011	0.0001	0.0001
0	200	0.0321	0.0002	0.0000	0.0086	0.0002	0.0001	0.0028	0.0002	0.0001
0	300	0.0708	0.0002	0.0001	0.0184	0.0002	0.0001	0.0056	0.0002	0.0001
0	400	0.1252	0.0002	0.0001	0.0324	0.0002	0.0002	0.0097	0.0002	0.0002
0	500	0.1953	0.0002	0.0001	0.0503	0.0002	0.0002	0.0149	0.0002	0.0003
0	600	0.2809	0.0003	0.0001	0.0724	0.0002	0.0003	0.0214	0.0002	0.0004
0	700	0.3818	0.0003	0.0001	0.0984	0.0002	0.0004	0.0291	0.0002	0.0005
0	800	0.4981	0.0003	0.0002	0.1284	0.0003	0.0005	0.0379	0.0003	0.0007
0	900	0.6295	0.0003	0.0002	0.1624	0.0003	0.0006	0.0480	0.0003	0.0008
0	1000	0.7760	0.0003	0.0003	0.2004	0.0003	0.0007	0.0592	0.0003	0.0010
0	1500	**1.7292**	0.0005	0.0006	0.4498	0.0004	0.0016	0.1330	0.0004	0.0022
0	2000	**3.0334**	0.0007	0.0010	0.7968	0.0006	0.0027	0.2362	0.0006	0.0039
0	2500	**4.6601**	0.0010	0.0015	**1.2394**	0.0008	0.0043	0.3686	0.0008	0.0061
0	3000	**6.5758**	0.0013	0.0022	**1.7751**	0.0011	0.0061	0.5299	0.0011	0.0088
0	3500	**8.7427**	0.0017	0.0030	**2.4007**	0.0014	0.0084	0.7199	0.0014	0.0120
300	100	0.0047	0.0006	0.0000	0.0024	0.0005	0.0000	0.0013	0.0005	0.0000
250	100	0.0048	0.0006	0.0000	0.0024	0.0005	0.0000	0.0013	0.0005	0.0000
200	100	0.0050	0.0006	0.0000	0.0024	0.0005	0.0000	0.0013	0.0005	0.0000
150	100	0.0052	0.0005	0.0000	0.0025	0.0005	0.0000	0.0013	0.0005	0.0000
100	100	0.0056	0.0005	0.0000	0.0026	0.0004	0.0000	0.0013	0.0004	0.0000
75	100	0.0059	0.0004	0.0000	0.0026	0.0004	0.0000	0.0013	0.0004	0.0000
50	100	0.0064	0.0003	0.0000	0.0027	0.0003	0.0000	0.0012	0.0003	0.0000
25	100	0.0073	0.0003	0.0000	0.0027	0.0002	0.0000	0.0012	0.0002	0.0000
-300	100	0.0052	0.0000	0.0001	0.0026	0.0000	0.0001	0.0011	0.0000	0.0002
-250	100	0.0056	0.0000	0.0001	0.0027	0.0000	0.0001	0.0010	0.0000	0.0002
-200	100	0.0064	0.0000	0.0001	0.0030	0.0000	0.0001	0.0017	0.0000	0.0002
-150	100	0.0093	0.0000	0.0001	0.0068	0.0000	0.0001	0.0905	0.0000	0.0001
-100	100	0.0497	0.0000	0.0001	0.3340	0.0000	0.0001	0.0025	0.0000	0.0001
-75	100	**88.4102**	0.0000	0.0001	0.0126	0.0000	0.0001	0.0013	0.0000	0.0001
-50	100	0.0483	0.0001	0.0001	0.0049	0.0000	0.0001	0.0010	0.0000	0.0001

-25	100	0.0152	0.0001	0.0000	0.0033	0.0001	0.0001	0.0010	0.0001	0.0001
1200	400	0.0049	0.0006	0.0001	0.0024	0.0005	0.0002	0.0013	0.0005	0.0002
1000	400	0.0050	0.0006	0.0001	0.0025	0.0005	0.0002	0.0014	0.0005	0.0002
800	400	0.0053	0.0006	0.0001	0.0027	0.0005	0.0002	0.0014	0.0005	0.0002
600	400	0.0060	0.0006	0.0037	0.0029	0.0005	0.0004	0.0016	0.0005	0.0004
400	400	0.0075	0.0005	0.0002	0.0036	0.0005	0.0068	0.0018	0.0005	**91.7167**
200	400	0.0135	0.0004	0.0001	0.0059	0.0004	0.0003	0.0027	0.0003	0.0004
150	400	0.0180	0.0003	0.0001	0.0075	0.0003	0.0002	0.0033	0.0003	0.0003
100	400	0.0268	0.0003	0.0001	0.0103	0.0003	0.0002	0.0042	0.0003	0.0003
50	400	0.0481	0.0003	0.0001	0.0162	0.0002	0.0002	0.0059	0.0002	0.0002
-1200	400	0.0050	0.0000	0.0001	0.0025	0.0000	0.0001	0.0014	0.0000	0.0002
-1000	400	0.0052	0.0000	0.0001	0.0027	0.0000	0.0001	0.0015	0.0000	0.0002
-800	400	0.0058	0.0000	0.0001	0.0030	0.0000	0.0001	0.0017	0.0000	0.0002
-600	400	0.0070	0.0000	0.0001	0.0037	0.0000	0.0001	0.0021	0.0000	0.0002
-400	400	0.0110	0.0000	0.0001	0.0062	0.0000	0.0001	0.0039	0.0000	0.0002
-200	400	0.0484	0.0001	0.0001	0.0400	0.0001	0.0002	0.0550	0.0001	0.0002
-150	400	0.1265	0.0001	0.0001	0.1723	0.0001	0.0002	**3.7606**	0.0001	0.0002
-100	400	**1.1026**	0.0001	0.0001	**9.5574**	0.0001	0.0002	0.0930	0.0001	0.0002
-50	400	**1.0697**	0.0002	0.0001	0.1105	0.0002	0.0002	0.0211	0.0002	0.0002
2400	800	0.0049	0.0006	0.0001	0.0025	0.0006	0.0002	0.0013	0.0006	0.0002
2000	800	0.0051	0.0006	0.0001	0.0026	0.0006	0.0002	0.0014	0.0006	0.0002
1800	800	0.0052	0.0006	0.0001	0.0026	0.0006	0.0002	0.0014	0.0006	0.0002
1600	800	0.0054	0.0006	0.0001	0.0027	0.0006	0.0002	0.0015	0.0005	0.0002
1000	800	0.0069	0.0006	0.0003	0.0034	0.0005	0.0003	0.0018	0.0005	0.0004
800	800	0.0081	0.0006	0.0007	0.0040	0.0005	0.0006	0.0021	0.0005	0.0007
600	800	0.0106	0.0005	0.0291	0.0051	0.0005	0.0026	0.0026	0.0005	0.0022
400	800	0.0169	0.0005	0.0013	0.0078	0.0004	0.0456	0.0038	0.0004	**98.6087**
200	800	0.0415	0.0004	0.0003	0.0174	0.0003	0.0013	0.0076	0.0003	0.0022
250	800	0.0310	0.0004	0.0004	0.0134	0.0004	0.0020	0.0061	0.0004	0.0037
100	800	0.0958	0.0003	0.0002	0.0356	0.0003	0.0007	0.0140	0.0003	0.0010
50	800	0.1831	0.0003	0.0002	0.0604	0.0003	0.0006	0.0214	0.0003	0.0008
-2400	800	0.0049	0.0017	0.0001	0.0025	0.0098	0.0001	0.0014	0.0161	0.0002
-2000	800	0.0052	0.0008	0.0001	0.0026	0.0003	0.0001	0.0014	0.0003	0.0002
-1800	800	0.0054	0.0003	0.0001	0.0027	0.0002	0.0001	0.0015	0.0001	0.0002
-1600	800	0.0056	0.0001	0.0001	0.0029	0.0001	0.0001	0.0016	0.0001	0.0002
-1000	800	0.0077	0.0001	0.0001	0.0040	0.0001	0.0002	0.0023	0.0001	0.0002
-800	800	0.0098	0.0001	0.0001	0.0052	0.0001	0.0002	0.0030	0.0001	0.0002
-600	800	0.0146	0.0001	0.0001	0.0080	0.0001	0.0002	0.0049	0.0001	0.0002
-400	800	0.0310	0.0002	0.0001	0.0185	0.0001	0.0002	0.0127	0.0001	0.0003
-200	800	0.1842	0.0002	0.0001	0.1603	0.0002	0.0003	0.2358	0.0002	0.0004
-250	800	0.0962	0.0002	0.0001	0.0698	0.0002	0.0003	0.0675	0.0002	0.0004
-100	800	**4.3635**	0.0003	0.0002	**30.7647**	0.0002	0.0004	0.4010	0.0002	0.0005
-50	800	**4.2369**	0.0003	0.0002	0.4556	0.0002	0.0004	0.0877	0.0002	0.0006

Table A2.5: Hartman Hahn efficiencies calculated for the C8 spins of G08, A92 and A93. Data points in bold were excluded from the analysis.

		G08			A92			A93		
Offset (Hz)	Power (Hz)	A_{HAHA}-C4	A_{HAHA}-C5	A_{HAHA}-C6	A_{HAHA}-C4	A_{HAHA}-C5	A_{HAHA}-C6	A_{HAHA}-C4	A_{HAHA}-C5	A_{HAHA}-C6
0	100	0.0004	0.0000	0.0002	0.0009	0.0000	0.0003	0.0012	0.0000	0.0004
0	200	0.0005	0.0000	0.0002	0.0012	0.0000	0.0004	0.0015	0.0000	0.0004
0	300	0.0006	0.0000	0.0002	0.0015	0.0000	0.0004	0.0018	0.0000	0.0005
0	400	0.0007	0.0000	0.0002	0.0018	0.0000	0.0005	0.0022	0.0000	0.0006
0	500	0.0008	0.0000	0.0002	0.0022	0.0000	0.0006	0.0027	0.0000	0.0007
0	600	0.0009	0.0000	0.0003	0.0026	0.0000	0.0006	0.0033	0.0000	0.0008
0	700	0.0010	0.0000	0.0003	0.0031	0.0000	0.0007	0.0040	0.0000	0.0009
0	800	0.0011	0.0000	0.0003	0.0036	0.0000	0.0008	0.0048	0.0000	0.0010

0	900	0.0013	0.0000	0.0004	0.0043	0.0000	0.0009	0.0056	0.0000	0.0011
0	1000	0.0014	0.0000	0.0004	0.0050	0.0000	0.0010	0.0066	0.0000	0.0012
0	1500	0.0025	0.0000	0.0006	0.0096	0.0000	0.0017	0.0130	0.0000	0.0021
0	2000	0.0040	0.0001	0.0008	0.0161	0.0000	0.0026	0.0220	0.0000	0.0032
0	2500	0.0059	0.0001	0.0011	0.0246	0.0001	0.0038	0.0338	0.0000	0.0048
0	3000	0.0082	0.0001	0.0015	0.0351	0.0001	0.0053	0.0483	0.0001	0.0067
0	3500	0.0110	0.0002	0.0020	0.0475	0.0001	0.0070	0.0655	0.0001	0.0089
300	100	0.0000	0.0000	0.0000	0.0000	0.0000	0.0000	0.0000	0.0000	0.0000
250	100	0.0000	0.0000	0.0000	0.0000	0.0000	0.0000	0.0000	0.0000	0.0000
200	100	0.0000	0.0000	0.0000	0.0000	0.0000	0.0000	0.0000	0.0000	0.0000
150	100	0.0000	0.0000	0.0000	0.0000	0.0000	0.0000	0.0001	0.0000	0.0000
100	100	0.0000	0.0000	0.0000	0.0001	0.0000	0.0000	0.0001	0.0000	0.0000
75	100	0.0001	0.0000	0.0000	0.0002	0.0000	0.0001	0.0002	0.0000	0.0001
50	100	0.0001	0.0000	0.0001	0.0003	0.0000	0.0001	0.0004	0.0000	0.0001
25	100	0.0003	0.0000	0.0001	0.0006	0.0000	0.0002	0.0007	0.0000	0.0002
-300	100	0.0014	0.0000	0.0006	0.0030	0.0000	0.0011	0.0036	0.0000	0.0013
-250	100	0.0014	0.0000	0.0006	0.0030	0.0000	0.0011	0.0035	0.0000	0.0013
-200	100	0.0014	0.0000	0.0006	0.0029	0.0000	0.0011	0.0034	0.0000	0.0012
-150	100	0.0013	0.0000	0.0005	0.0028	0.0000	0.0010	0.0033	0.0000	0.0012
-100	100	0.0011	0.0000	0.0005	0.0025	0.0000	0.0009	0.0029	0.0000	0.0010
-75	100	0.0010	0.0000	0.0004	0.0022	0.0000	0.0008	0.0026	0.0000	0.0009
-50	100	0.0008	0.0000	0.0003	0.0019	0.0000	0.0007	0.0022	0.0000	0.0008
-25	100	0.0006	0.0000	0.0003	0.0014	0.0000	0.0005	0.0017	0.0000	0.0006
1200	400	0.0021	0.0000	0.0000	0.0013	0.0000	0.0002	0.0014	0.0000	0.0006
1000	400	0.0003	0.0000	0.0000	0.0081	0.0000	0.0001	0.0042	0.0000	0.0002
800	400	0.0001	0.0000	0.0000	0.0090	0.0000	0.0001	**0.1418**	0.0000	0.0001
600	400	0.0001	0.0000	0.0000	0.0013	0.0000	0.0001	0.0026	0.0000	0.0001
400	400	0.0002	0.0000	0.0000	0.0008	0.0000	0.0001	0.0013	0.0000	0.0001
200	400	0.0003	0.0000	0.0001	0.0011	0.0000	0.0002	0.0014	0.0000	0.0003
150	400	0.0004	0.0000	0.0001	0.0012	0.0000	0.0003	0.0016	0.0000	0.0003
100	400	0.0005	0.0000	0.0001	0.0014	0.0000	0.0003	0.0018	0.0000	0.0004
50	400	0.0006	0.0000	0.0002	0.0016	0.0000	0.0004	0.0020	0.0000	0.0005
-1200	400	0.0015	0.0010	0.0006	0.0032	0.0000	0.0012	0.0038	0.0000	0.0013
-1000	400	0.0015	0.0000	0.0006	0.0032	0.0000	0.0012	0.0038	0.0000	0.0013
-800	400	0.0015	0.0000	0.0006	0.0032	0.0000	0.0012	0.0038	0.0000	0.0013
-600	400	0.0014	0.0000	0.0006	0.0031	0.0000	0.0011	0.0037	0.0000	0.0013
-400	400	0.0013	0.0000	0.0005	0.0030	0.0000	0.0010	0.0036	0.0000	0.0012
-200	400	0.0011	0.0000	0.0004	0.0026	0.0000	0.0008	0.0031	0.0000	0.0010
-150	400	0.0010	0.0000	0.0004	0.0024	0.0000	0.0008	0.0030	0.0000	0.0009
-100	400	0.0009	0.0000	0.0003	0.0022	0.0000	0.0007	0.0027	0.0000	0.0008
-50	400	0.0008	0.0000	0.0003	0.0020	0.0000	0.0006	0.0025	0.0000	0.0007
2400	800	0.0010	0.0000	0.0004	0.0036	0.0000	0.0006	0.0043	0.0000	0.0008
2000	800	0.0010	0.0000	**0.0916**	0.0036	0.0000	0.0008	0.0044	0.0000	0.0009
1800	800	0.0015	0.0000	0.0011	0.0036	0.0000	0.0017	0.0046	0.0000	0.0015
1600	800	0.0033	0.0000	0.0003	0.0040	0.0000	0.0087	0.0049	0.0000	0.0044
1000	800	0.0033	0.0000	0.0001	0.0850	0.0000	0.0011	0.0403	0.0000	0.0019
800	800	0.0015	0.0000	0.0001	**0.0946**	0.0000	0.0007	**1.4265**	0.0000	0.0010
600	800	0.0010	0.0000	0.0001	0.0117	0.0000	0.0006	0.0239	0.0000	0.0008
400	800	0.0009	0.0000	0.0002	0.0055	0.0000	0.0006	0.0086	0.0000	0.0008
200	800	0.0010	0.0000	0.0002	0.0040	0.0000	0.0007	0.0056	0.0000	0.0008
250	800	0.0010	0.0000	0.0002	0.0042	0.0000	0.0006	0.0061	0.0000	0.0008
100	800	0.0011	0.0000	0.0003	0.0038	0.0000	0.0007	0.0051	0.0000	0.0009
50	800	0.0011	0.0000	0.0003	0.0037	0.0000	0.0008	0.0049	0.0000	0.0009
-2400	800	0.0015	0.0000	0.0006	0.0033	0.0000	0.0012	0.0039	0.0000	0.0014
-2000	800	0.0015	0.0000	0.0006	0.0033	0.0000	0.0012	0.0039	0.0000	0.0014
-1800	800	0.0016	0.0000	0.0006	0.0033	0.0000	0.0012	0.0039	0.0000	0.0014
-1600	800	0.0016	0.0000	0.0006	0.0034	0.0000	0.0012	0.0040	0.0000	0.0014
-1000	800	0.0016	0.0001	0.0006	0.0035	0.0000	0.0012	0.0042	0.0000	0.0014
-800	800	0.0015	0.0000	0.0006	0.0035	0.0000	0.0012	0.0042	0.0000	0.0014

-600	800	0.0015	0.0000	0.0005	0.0036	0.0000	0.0011	0.0043	0.0000	0.0013
-400	800	0.0014	0.0000	0.0005	0.0036	0.0000	0.0011	0.0044	0.0000	0.0012
-200	800	0.0013	0.0000	0.0004	0.0036	0.0000	0.0010	0.0045	0.0000	0.0011
-250	800	0.0013	0.0000	0.0004	0.0036	0.0000	0.0010	0.0045	0.0000	0.0012
-100	800	0.0012	0.0000	0.0004	0.0036	0.0000	0.0009	0.0046	0.0000	0.0010
-50	800	0.0012	0.0000	0.0003	0.0036	0.0000	0.0008	0.0047	0.0000	0.0010

Table A2.6: Hartman Hahn efficiencies calculated for the C1' spins of A92, A93 and G94. Data points in bold were excluded from the analysis.

Offset (Hz)	Power (Hz)	A92 A_{HAHA}-C2'	A93 A_{HAHA}-C2'	G94 A_{HAHA}-C2'
0	100	0.0113	0.0145	0.0087
0	200	0.0136	0.0161	0.0102
0	300	0.0163	0.0179	0.0120
0	400	0.0195	0.0198	0.0140
0	500	0.0230	0.0220	0.0163
0	600	0.0271	0.0243	0.0189
0	700	0.0317	0.0269	0.0218
0	800	0.0369	0.0297	0.0251
0	900	0.0426	0.0327	0.0286
0	1000	0.0490	0.0360	0.0326
0	1500	**0.0906**	0.0559	0.0580
0	2000	**0.1494**	0.0824	**0.0937**
0	2500	**0.2260**	**0.1158**	**0.1402**
0	3000	**0.3203**	**0.1561**	**0.1975**
0	3500	**0.4321**	**0.2034**	**0.2657**
300	100	0.0365	0.0001	0.0284
250	100	0.0359	0.0001	0.0280
200	100	0.0350	0.0002	0.0272
150	100	0.0331	0.0005	0.0257
100	100	0.0294	0.0013	0.0228
75	100	0.0263	0.0024	0.0203
50	100	0.0220	0.0045	0.0170
25	100	0.0167	0.0083	0.0129
-300	100	0.0001	**0.1008**	0.0001
-250	100	0.0001	0.0852	0.0001
-200	100	0.0003	0.0719	0.0002
-150	100	0.0005	0.0597	0.0004
-100	100	0.0013	0.0468	0.0010
-75	100	0.0022	0.0395	0.0017
-50	100	0.0039	0.0312	0.0030
-25	100	0.0069	0.0225	0.0052
1500	500	0.0385	0.0001	0.0299
1200	500	0.0386	0.0001	0.0299
900	500	0.0385	0.0003	0.0297
800	500	0.0383	0.0004	0.0295
600	500	0.0375	0.0010	0.0287
400	500	0.0354	0.0025	0.0268
250	500	0.0322	0.0056	0.0240
200	500	0.0307	0.0074	0.0227
100	500	0.0271	0.0129	0.0197
50	500	0.0251	0.0169	0.0180
-1500	500	0.0145	**0.1628**	0.0132
-1200	500	0.0689	**0.6487**	**1.2022**
-900	500	**0.1039**	**42.5640**	0.0183
-800	500	0.0375	**2.8238**	0.0112

-600	500	0.0155	**0.4031**	0.0073
-400	500	0.0129	**0.1382**	0.0075
-250	500	0.0148	0.0712	0.0095
-200	500	0.0160	0.0571	0.0105
-100	500	0.0191	0.0361	0.0131
-50	500	0.0210	0.0283	0.0147
3000	1000	0.0396	0.0001	0.0308
2700	1000	0.0399	0.0001	0.0310
2300	1000	0.0404	0.0001	0.0313
2000	1000	0.0409	0.0002	0.0316
1700	1000	0.0416	0.0004	0.0320
1500	1000	0.0421	0.0005	0.0323
800	1000	0.0442	0.0028	0.0331
600	1000	0.0449	0.0051	0.0331
400	1000	0.0456	0.0094	0.0329
250	1000	0.0463	0.0154	0.0326
200	1000	0.0466	0.0182	0.0325
100	1000	0.0476	0.0255	0.0325
50	1000	0.0482	0.0302	0.0325
-3000	1000	0.0438	0.0568	0.0331
-2700	1000	0.0448	0.0615	0.0328
-2300	1000	0.0464	0.0743	0.0327
-2000	1000	0.0505	**0.0967**	0.0371
-1700	1000	0.0675	**0.1523**	0.0601
-1500	1000	**0.1076**	**0.2472**	**0.1279**
-800	1000	**0.3530**	**3.6833**	**0.1056**
-600	1000	**0.1203**	**0.5067**	0.0546
-400	1000	0.0714	**0.1700**	0.0393
-250	1000	0.0578	**0.0902**	0.0349
-200	1000	0.0551	0.0743	0.0340
-100	1000	0.0513	0.0513	0.0330
-50	1000	0.0500	0.0429	0.0327
1000	1000	0.0436	0.0017	0.0330

1.3 Tables of ^{15}N relaxation measurements for non-elongated and elongated mA-site

Table A2.7: ^{15}N relaxation measurements calculated for EAU-mA-site and EGC-mA-site rRNA samples.

EAU-mA-site rRNA and EGC-mA-site rRNA				
Residue	Nitrogen	R_1 (Hz)	R_2 (Hz)	S^2_{rel}
G02	N1	0.742 ± 0.003	24.41 ± 0.42	0.93±0.018
G03	N1	0.73 ± 0.01	26.14 ± 0.80	1.00±0.02
G05	N1	0.82 ± 0.01	24.65 ± 0.58	0.94±0.02
G08	N1	0.92 ± 0.07	25.25 ± 1.10	0.96±0.03
G17	N1	1.03 ± 0.01	18.52 ± 0.23	0.70±0.02
G87	N1	0.90 ± 0.02	19.52 ± 0.23	0.74±0.02
U90	N3	0.84 ± 0.12	20.55 ± 0.08	
G91	N1	0.97 ± 0.01	22.10 ± 0.13	0.84±0.02